8-2020

Integrated DC-DC Charger Powertrain Converter Design for Electric Vehicles Using Wide Bandgap Semiconductors

Saeed Anwar
University of Tennessee, sanwar@vols.utk.edu

To the Graduate Council:

I am submitting herewith a dissertation written by Saeed Anwar entitled "Integrated DC-DC Charger Powertrain Converter Design for Electric Vehicles Using Wide Bandgap Semiconductors." I have examined the final electronic copy of this dissertation for form and content and recommend that it be accepted in partial fulfillment of the requirements for the degree of Doctor of Philosophy, with a major in Electrical Engineering.

Daniel Costinett, Major Professor

We have read this dissertation and recommend its acceptance:

Leon Tolbert, Fred Wang, David Irick

Accepted for the Council:

Dixie L. Thompson

Vice Provost and Dean of the Graduate School

(Original signatures are on file with official student records.)

Integrated DC-DC Charger Powertrain Converter Design for Electric Vehicles Using Wide Bandgap Semiconductors

A Dissertation Presented for the

Doctor of Philosophy

Degree

The University of Tennessee, Knoxville

Saeed Anwar

August 2020

Acknowledgment

I would like to express my sincere gratitude to my advisor Dr. Daniel Costinett for his support and guidance for my Ph.D. studies at the University of Tennessee, Knoxville (UTK). He helped me to understand the design challenges of power electronics converter. He also encouraged to explain research problems to the general audience in a very interesting way, perform collaborative teamwork, participate in leadership activities, and increase networking skills. I believe all these supports and encouragements from my advisor will have a profound influence in my future career.

I like to express my gratitude to my committee members, Dr. Leon Tolbert, Dr. Fred Wang, and Dr. David K. Irick. Dr. Tolbert helped at UTK and Oak Ridge National Lab (ORNL) to review my work and gave a lot of valuable suggestions to make the work better. Dr. Wang helped me to think and understand in border level about the significance of any research work for industry. Dr. Irick mentored me in the EcoCAR 3 competition and I learned a lot about vehicles from him.

I am grateful to work with a diverse group of friends at CURENT and UTK. I like to thank Dr. Zheyu Zhang, Dr. Weimin Zhang, and Dr. Bo Liu for mentoring me. I like to specially thank Kamal Sabi, Andrew Foote, Jared Baxter, Spencer Cochran, Dr. Jiang, Dr. Zhao, Jie Li, Ruiyang Qin, Quillen Blalock, Jingjing Sun, and Peter Pham for their feedback, reviews, and motivations.

I like to thank CURENT, ORNL, and UTK for the academic and financial support for my Ph.D. research. I am grateful to Dr. Ozpineci, Dr. Onar, Dr. Mukherjee, Dr. Chowdhury, Dr. Mohammad, Dr. Galigekere, Dr. Chinthavali, Dr. Pries, Dr. Asa, Dr. Gurpinar, Jon Wilkins, Steven Campbell, Larry Seiber, Christian L Boone, and Cliff White for the support at ORNL.

Finally, I would like to express my sincere gratitude to my wife Tasneem Farzana Khan, my parents Md. Zowadul Munir and Mahmuda Khanam, and my sister Sharmin Afrose for their support, love, and encouragement.

Abstract

Electric vehicles (EVs) adoption is growing due to environmental concerns, government subsidies, and cheaper battery packs. The main power electronics design challenges for next-generation EV power converters are power converter weight, volume, cost, and loss reduction. In conventional EVs, the traction boost and the onboard charger (OBC) have separate power modules, passives, and heat sinks. An integrated converter, combining and re-using some charging and powertrain components together, can reduce converter cost, volume, and weight. However, efficiency is often reduced to obtain the advantage of cost, volume, and weight reduction.

An integrated converter topology is proposed to combine the functionality of the traction boost converter and isolated DC-DC converter of the OBC using a hybrid transformer where the same core is used for both converters. The reconfiguration between charging and traction operation is performed by the existing Battery Management System (BMS) contactors. The proposed converter is operated in both boost and dual active bridge (DAB) mode during traction operation. The loss mechanisms of the proposed integrated converter are modeled for different operating modes for design optimization. An aggregated drive cycle is considered for optimizing the integrated converter design parameters to reduce energy loss during traction operation, weight, and cost. By operating the integrated converter in DAB mode at light-load and boost mode at high-speed heavy-load, the traction efficiency is improved. An online mode transition algorithm is also developed to ensure stable output voltage and eliminate current oscillation during the mode transition. A high-power prototype is developed to verify the integrated converter functionality, validate the loss model, and demonstrate the online transition algorithm. An automated closed-loop controller is developed to implement the transition algorithm which can automatically make the transition between modes based on embedded efficiency mapping. The closed-loop control system also

regulates the integrated converter output voltage to improve the overall traction efficiency of the integrated converter. Using the targeted design approach, the proposed integrated converter performs better in all three aspects including efficiency, weight, and cost than comparable discrete solutions for each converter.

Table of Contents

List of Tables

List of Figures

1 Introduction

Electric vehicles (EVs) adoption is increasing due to environmental awareness, government subsidies, lower battery prices, and the price volatility of the fossil fuel supply [1, 2]. In 2016, 28% of the total US emissions were generated from the transportation sectors, primarily from light-duty vehicles [3]. These emissions are causing smog and health issues in urban areas. Although EVs are also responsible for carbon emission in the process of electricity generation [4], the source of electricity is getting cleaner due to the integration of renewable energy sources into the grid.

Tax credits and incentives are offered to reduce the up-front cost of EVs to consumers [5]. Different manufacturers are offering free charging at public parking lots and office areas to support the growth of PEVs and encourage more customers to adopt EVs [6]. Another incentive for individuals to purchase EVs includes access to HOV lanes for low emission vehicles by the Department of Transportation in different states [7].

EVs have a long history of variable consumer demand along with gasoline prices, regulations, and technological development. By 1900, a third of the total vehicles on the road were electric cars in the US [8]. However, with the mass production of gasoline cars, the price of a gasoline car dropped to almost 63% cheaper than an electric car in 1912. The decrease in gasoline prices, the availability of gasoline in rural areas, and the improvement in gasoline vehicle technologies led to the complete decline of EVs by 1935 in the US [8]. EVs sales increased again beginning 1999, as shown in Figure 1.1 [9], with the commercial production of the Toyota Prius. Furthermore, the increase in gasoline prices motivated people to purchase hybrid electric vehicles (HEVs) which have less emission and higher city fuel economy. According to the prediction shown in Figure 1.2 [10], EVs will comprise 35% of all new vehicle sales by 2040. To sustain the growth of EVs, it is important to reduce the traction drive system cost and improve the efficiency [11, 12].

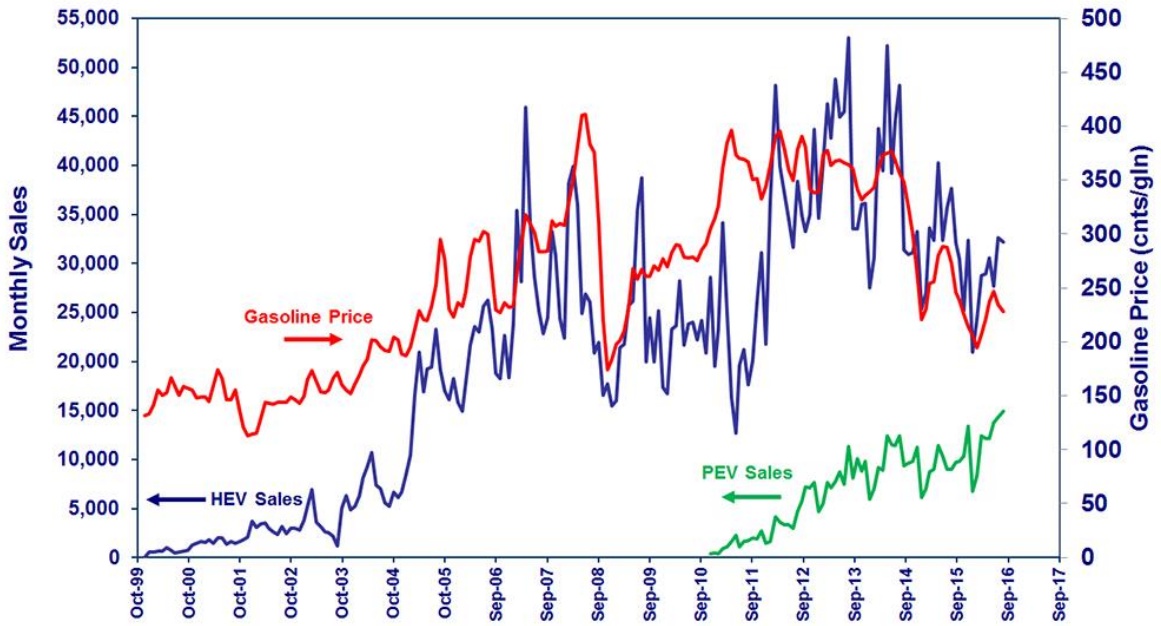

Figure 1.1. PEV and HEV sales [9].

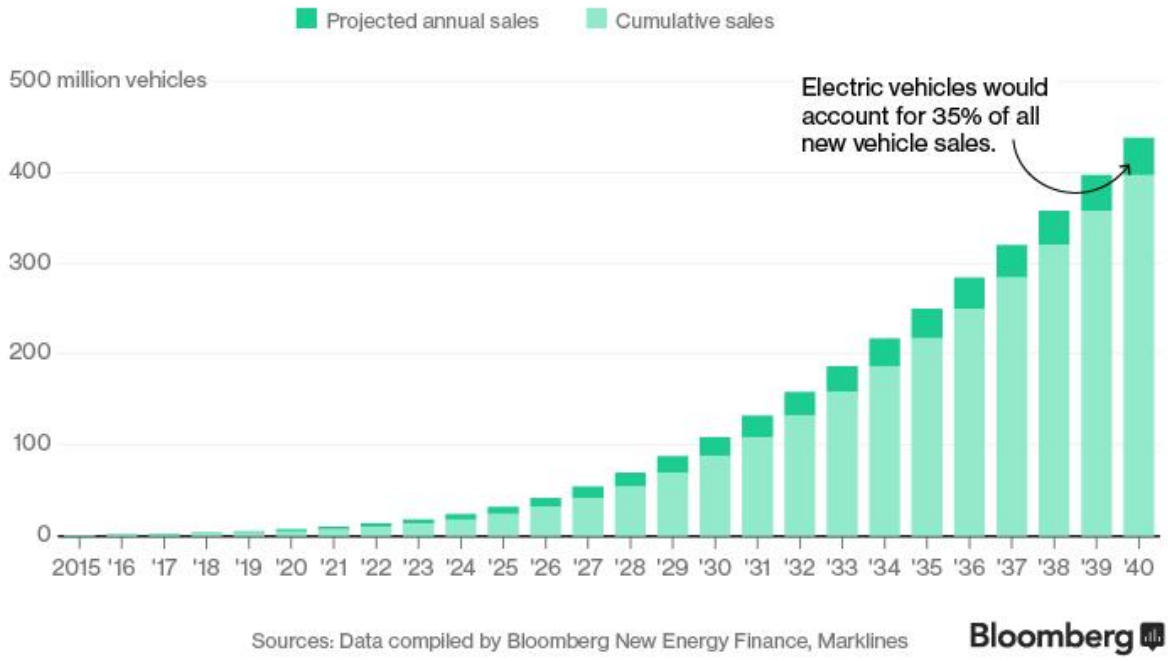

Figure 1.2. EV Sales prediction for 2040 [10].

1.1 Role of Power Electronics in EVs

Power converters are used in EVs during traction as well as vehicle charging operation. The traction converters are also known as the power control unit (PCU) [13]. Typical converters used in EVs are shown in Figure 1.3. During traction operation, the electric motor is driven through the bidirectional boost converter and inverter [14]. The bidirectional boost converter is optional in EVs. Accessory loads are powered by the high voltage EV battery using several low power step down DC-DC converters [15]. The EV battery is charged from the grid using the onboard battery charger.

1.1.1 PCU

The PCU delivers power to the traction motor from the high voltage (HV) battery. The major high-power components of PCU are – inverter, traction bidirectional DC-DC converter, and DC-DC converter for auxiliary loads [16]. The power level of the PCU ranges from 20 kW to over 250 kW depending on the type of EVs [17, 18]. The PCU of a 2010 Toyota Prius HEV is shown in Figure 1.4.

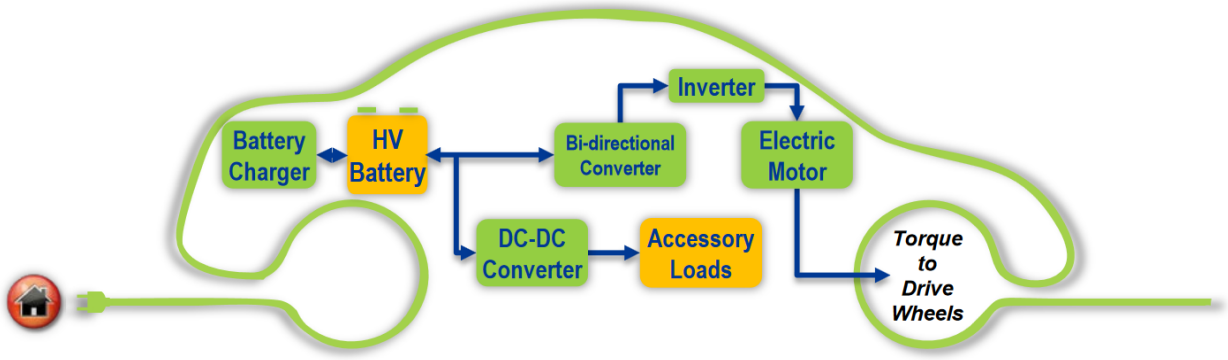

Figure 1.3. Converters used in EVs [18].

The inverter is responsible for controlling the power flow from the battery to the traction motor [19]. Based on the torque-speed requirement at the different operating conditions, the inverter power processing varies during the EV drive cycle. The inverter also captures the regenerative braking energy from the traction motor and feeds back to the battery. In the Toyota Prius hybrid system, two separate inverters are used for the motor and generator [13].

The bidirectional boost converter steps up the battery voltage to the inverter to ensure the inverter operation at optimum points based on different loads [20, 21]. The bidirectional boost converter decouples the inverter operation and regulates the voltage regardless of the varying state of the charge (SOC) of the battery. The bidirectional boost converter is implemented in Toyota Prius, Toyota Camry, BMW i3, and Honda Accord PCUs to improve the motor-inverter efficiency for the different torque-speed conditions [20]. In contrast, Nissan Leaf does not have a bidirectional boost converter [22]. As a result, the inverter used in Nissan Leaf is always operated at higher battery pack voltage sacrificing overall traction efficiency at high speed low torque condition [22]. The converter also transfers the regenerative energy to the battery. The boost inductor and bulk capacitor make up 40% of the volume of the Toyota Prius PCU [23].

The auxiliary loads are also powered by the HV battery through a DC-DC converter. These auxiliary loads include heaters, fans, lighting, power steering, infotainment systems, controllers, low power electronics system, and user on-demand low power equipment charging outlets [24].

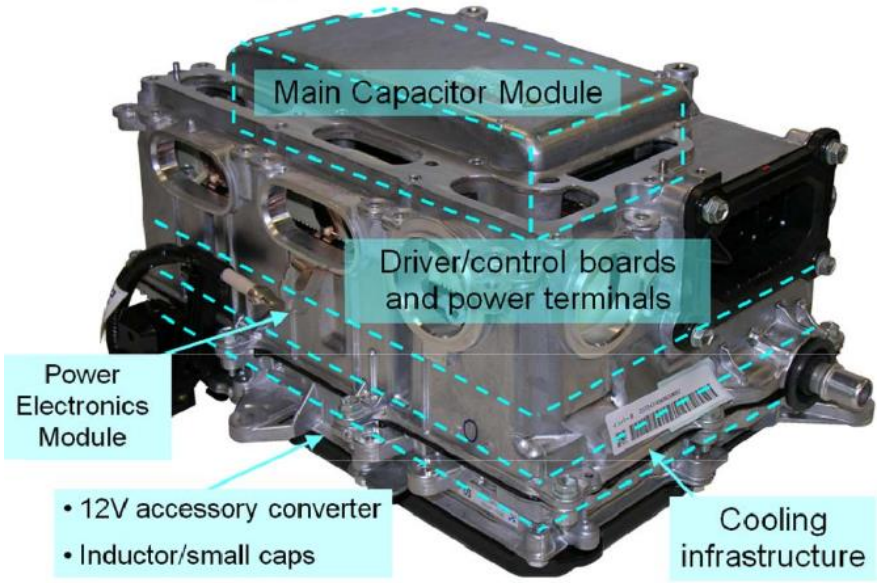

Figure 1.4. PCU of 2010 Toyota Prius [13].

1.1.2 Onboard Charger

The battery charger controls the power flow from the grid to the HV battery by monitoring the state of the charge of the battery pack. The charging time depends on the power level of the EV battery charger and the EV battery pack size. Based on the charger power level, the charger can be categorized as Level 1, Level 2, and Level 3 charger [25]. A Level 1 charger is supplied from standard wall 120 V outlet and the charging power is limited to 1.8 kW. A Level 2 charger uses a 240 V outlet and the charging power is typically 3.3 kW to 12 kW. Level 3 chargers are fast DC chargers that are available at commercial EV charging locations and the charging power is higher than 20 kW. With the consumer demand for longer driving range and shorter charging time, level 2 chargers are used in onboard chargers. The 2013 Nissan Leaf has a Level 2 onboard charger which is shown in Figure 1.5 [26].

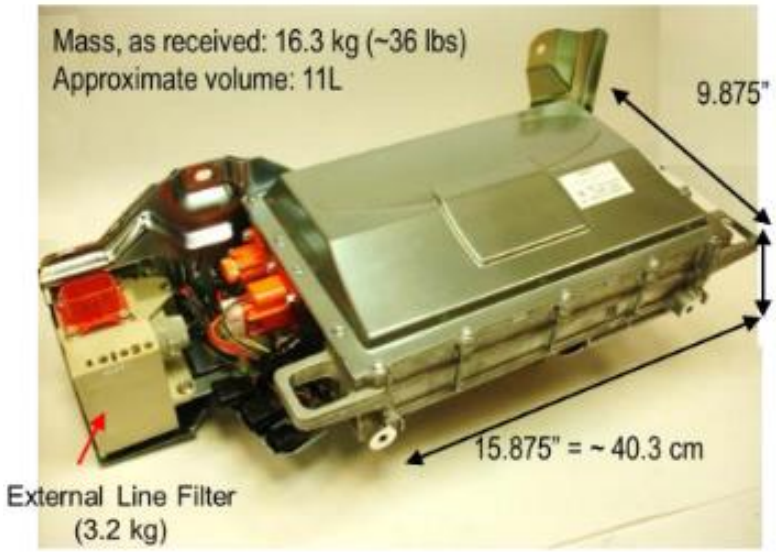

Figure 1.5. 2013 Nissan Leaf onboard charger [26].

The onboard charger has two major components – power factor correction unit (PFC) and isolated DC-DC converter [25, 27]. The PFC unit maintains unity power factor, reduces switching noise during the charging operation [28], and boosts the voltage for the isolated DC-DC converter stage. The isolated DC-DC converter provides galvanic isolation using a high-frequency isolation transformer [29].

1.2 Scopes for Improvement

The power electronics converter design challenges are power converter weight, size, loss, and price reduction [30]. An efficient power converter can maximize the driving range from the EV battery pack and requires smaller heat sink volume and weight.

1.2.1 Weight and Volume

The weight and volume of the 2010 Toyota Prius PCU are 13 kg and 16.2 L respectively [13]. The PCU is heavy and bulky due to the high-power boost inductor, bulk capacitor, and cooling systems. The boost converter in the 2010 Toyota Prius PCU contributes to about 40% of the total PCU weight and 30% of the total PCU volume [13]. The total cooling infrastructure contributes to about 34% of the total PCU volume. The main capacitor module also contributes to about 17% of the total PCU volume and 17% of the total PCU weight. The converter weight and volume increase with the power rating of the PCU [13].

The weight and volume of the 2013 Nissan Leaf PCU are 16.3 kg and 11 L, respectively, as shown in Figure 1.5. To maintain the charging standard and grid power quality requirement, the onboard charger is heavy and bulky due to the isolation transformer, filter inductors, capacitors, and heat sink [31]. The size of the isolation transformer and filter inductors can be reduced by increasing the switching frequency.

1.2.2 Efficiency

In 2012, the average silicon-based electric drive system efficiency was around 90% [30]. The peak efficiency of the 36.5 kW Lexus LS 600H traction DC-DC converter is around 97.5% for 650V step-up operation at 5 kHz switching frequency [32]. The power conversion loss generates heat in the power converter and needs to be removed by the thermal management system. High-efficiency converters allow for smaller thermal management components. As a result, the heat sink size and weight can be reduced. High efficiency also enables reduced converter size by higher switching frequency. With improved efficiency, the energy saved in the traction drive system can

be used to increase the range of the EVs. For a 120 V charging system, total efficiency is reported around 87% for 3.3kW operation and the DC-DC converter efficiency is about 94% [22].

The power loss reduction target for 2022 electric drive system is set at 40% by the U.S. Department of Energy (DOE) [30]. The peak efficiency of the traction motor occurs in the high-power region as shown in Figure 1.6 [30]. However, the power requirement for EVs varies for different driving conditions. The fraction of time spent at different torques and speeds at urban dynamometer driving schedule (UDDS) and highway driving schedule are shown in Figure 1.7. The most common operating conditions occur at much lower torque than the peak efficiency region shown in Figure 1.6. To improve efficiency, the traction efficiency map needs to be altered to shift the peak operating region to lower powers based on the drive cycle. In this way, the driving range can be extended and EVs can be operated more efficiently.

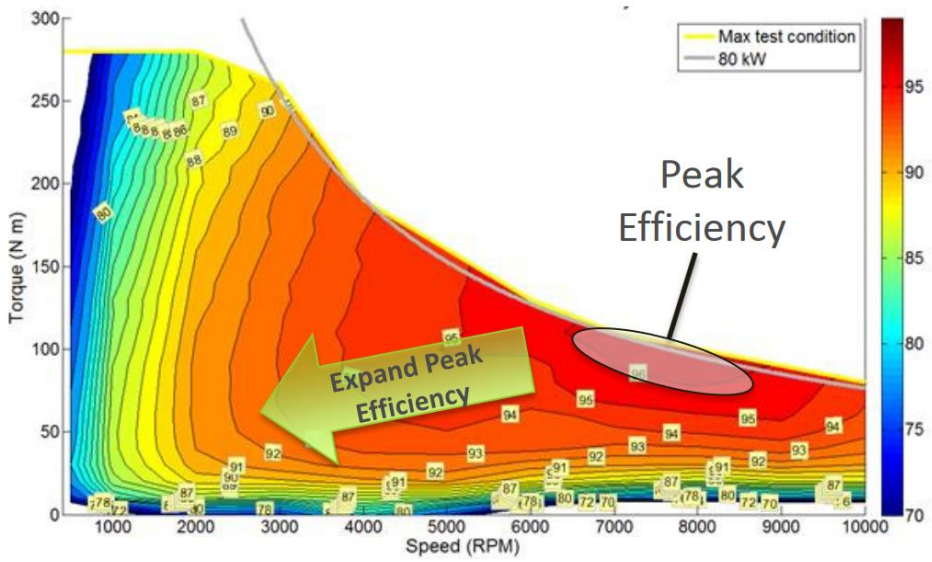

Figure 1.6. Typical traction motor efficiency map [30].

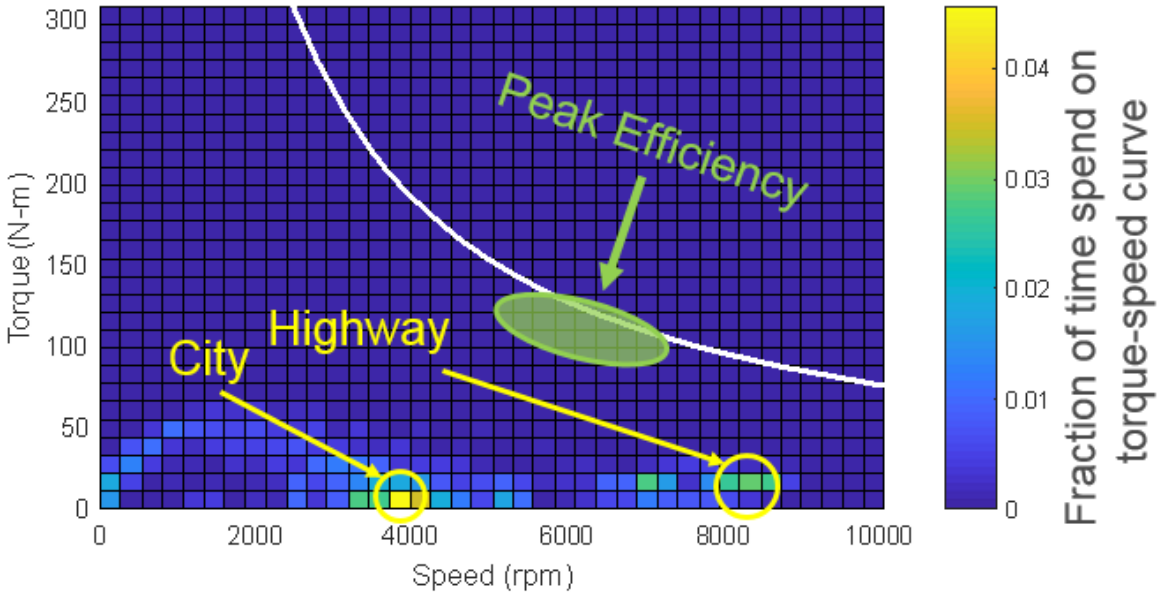

Figure 1.7. Histogram of the torque-speed characteristics for urban dynamometer driving schedule and highway driving schedule.

1.2.3 Price

According to the US DOE, the EV price is the most significant challenge to increased EV adoption by consumers [18]. The hybrid traction drive price breakdown, which includes the battery price is shown in Figure 1.8 [33]. The second-largest contributing factor to high EV price is power electronics, which is 24% of the total hybrid traction drive system cost [33]. The price of the Tesla Model S electric drive system (excluding battery price) is around $5,400 which is about 7% of the total price of the vehicle [18, 34]. The price of a Chevy Volt traction drive system (excluding battery price) is also around 7.2% of the vehicle price [18, 35]. The price of a 3.3 kW onboard charger was about $900-$1,000 in 2010 [18] which is almost 4% of the Nissan Leaf price. The price reduction is the most significant challenge for the electric drive system [30, 36].

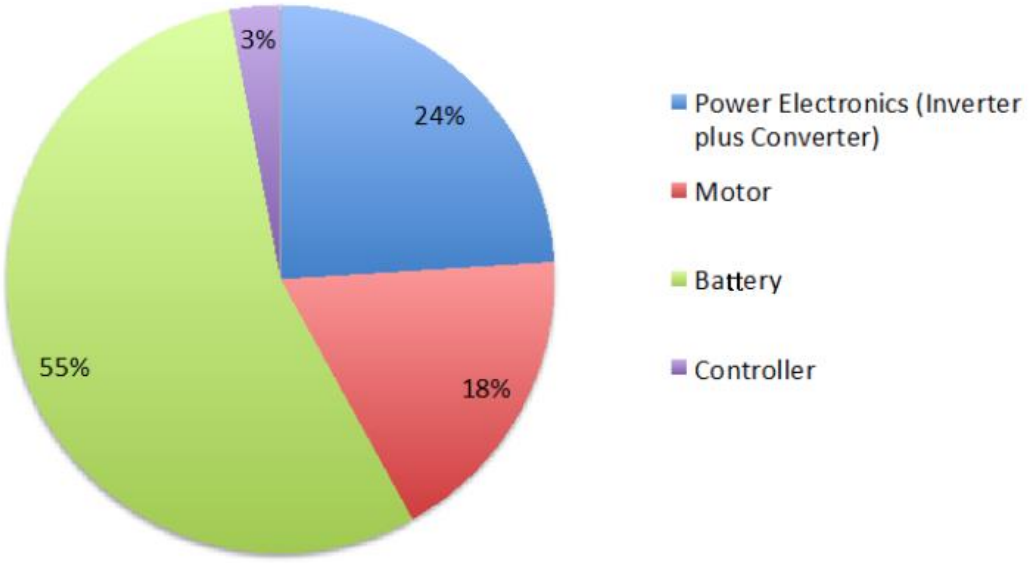

Figure 1.8. Hybrid traction drive system price breakdown [33].

Based on the high voltage power electronics price from the US DOE [11], power modules and associated gate drivers are the most expensive inverter components as shown in Figure 1.9 [11]. The thermal management system, housing, inductors, transformers, and capacitors also increase the EV price [37]. Reducing the component count can potentially reduce the price of the power converter.

1.3 Research Approaches for Achieving Targets

With the latest technological improvement, different approaches are proposed to reduce the volume, weight, conversion loss, and price of EVs [30, 38]. The approaches include the adoption of wide bandgap (WBG) devices, different control methodologies, and modulation techniques, design optimization for magnetics size reduction and application-oriented loss reduction, and different topologies to share components among the power converters.

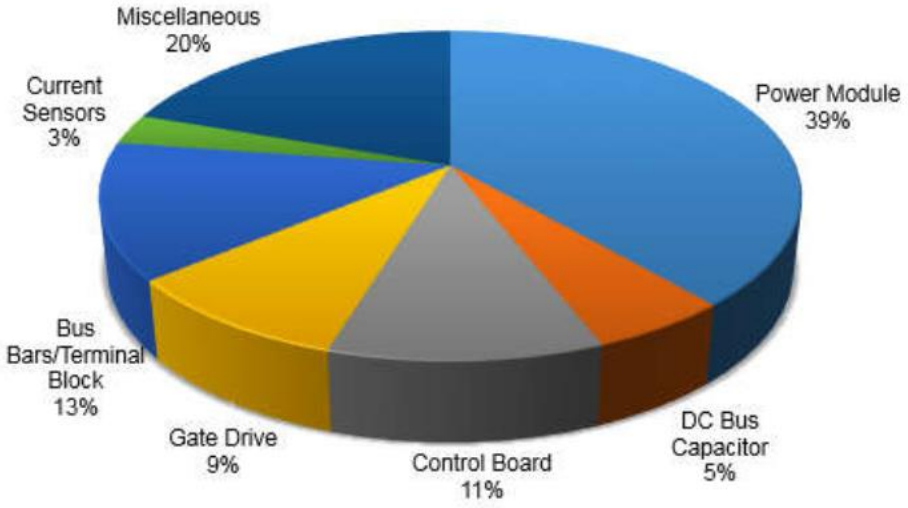

Figure 1.9. High voltage power electronics price status in 2015 [11].

1.3.1 Wide Band Gap Devices

Commercially available wide bandgap (WBG) semiconductor devices include Silicon Carbide (SiC) and Gallium Nitride (GaN) [39]. SiC devices are commercially available up to 10 kV voltage rating. For EV applications, 650 V, 900 V, and 1200 V SiC devices are good candidates. However, GaN devices are only available as a lateral device as they are fabricated by growing GaN material on Si or sapphire substrate due to the lack of high-quality defect-free GaN wafer [39]. As a result, commercially available GaN devices are currently limited to 650 V voltage rating.

Conventional EVs use Si insulated-gate bipolar transistor (IGBT) based bidirectional boost converter and inverters [20]. IGBTs are a mature technology and have field-proven reliability. Since the IGBT is a minority carrier device, it exhibits tail current during the turn-off transition due to the minority carrier recombination. The tail current limits the switching frequency of the IGBT based converters. As a result, bulky inductors and capacitors are required to filter the

switching ripple. IGBT operation is impacted by temperature variation and requires a large heat sink and thermal management [40]. On the other hand, MOSFETs can be operated at higher switching frequency as they are majority carrier devices. However, high voltage (900 V – 1200 V) Si MOSFETs are not practical to use in high-efficiency high-power operation due to large on-state resistance increase at elevated junction temperature. As a result, they are used for low voltage onboard charger applications. Inductors and capacitors make up 40% of the volume of the Toyota Prius PCU [23]. By increasing the switching frequency, the size of the inductors can be reduced.

Compared to Si devices, WBG devices have a higher breakdown field, higher thermal conductivity, and higher electron saturation velocity [41]. The switching frequency of SiC MOSFETs can be increased without sacrificing overall system efficiency since they are majority carrier devices. By increasing the converter switching frequency, the size and weight of the passive components, which include inductors and transformers, can be reduced. Since SiC devices have better thermal conductivity than Si devices, the heat sink and thermal management system requirement can be reduced. The SiC-based converter can be operated at a higher junction temperature than silicon IGBTs as well without significant performance degradation. Toyota set an 80% volume reduction goal by converting IGBT based PCU to SiC-based PCU [23]. WBG devices are expensive compared with the Si devices. However, the advantages of WBG devices can be realized at the system level reducing the overall system loss, weight, and price [42].

1.3.2 Control

Controllers, including digital signal processor (DSP) and field-programmable gate array (FPGA), are getting faster to compute more complex algorithms and store larger lookup tables. For traction operation, control algorithms can improve the traction efficiency based on the modeled database by selecting the optimum bus voltage of the traction DC-DC converter [21]. A complex

predictive algorithm is implemented in the controller to predict the inverter current requirement based on the torque command. The DC-DC stage of the traction converter is used to compensate for the inverter current by using an intelligent control algorithm. In this way, the size of the bulk capacitor can be reduced as well [21]. The controller can improve converter efficiency by changing the modulation at different power levels [43]. Based on the analytical model, the light load efficiency is improved by switching among different modulation techniques. Variable frequency can improve the converter efficiency at different power levels as well [44].

1.3.3 Design Optimization

Optimization is the process to select a design among different possible design combinations based on an objective function. Different optimization methods have been investigated for power converters to reduce the magnetics size and improve converter efficiency [45, 46]. Optimization is also used for complex magnetics design to reduce the power converter weight and loss [47]. Optimization can also improve power converter efficiency at different drive cycles [48]. Using design optimization, power converter performance can be improved by reducing the magnetics weight, heat sink weight, and power converter loss.

1.3.4 Topology

Different converter topologies are used to reduce the power converter loss, price, weight, and volume. Separate converters with different topology are paralleled to operate at different output power in [48]. Power converters with integrated magnetics are also explored to reduce the power converter weight and size in [49, 50]. Integrated converter topologies are another approach to reduce the power converter price, weight, and volume. In an integrated converter, the functionality of multiple converters is combined into a single converter [51]. The integrated converter has the

potential to reduce the total number of high-power switches and passive elements including capacitors, inductors, and transformers [52]. The main challenges of integrated converters are control complexity and the need for extra hardware for functionality reconfiguration. The extra hardware includes mechanical contactors and solid-state switches [25]. The mechanical contactors are bulky and require a longer time to complete the connect and disconnect process. On the other hand, the solid-state switches are expensive and lossy.

1.4 Dissertation Overview

An integrated DC-DC converter topology is proposed in the dissertation to improve the overall traction efficiency, and reduce the weight and cost of the traction boost converter and isolated DC-DC stage of OBC. The proposed integrated DC-DC converter is developed by integrating the magnetics of boost stage and isolated DC-DC stage of OBC, sharing the high-power switches, and utilizing the existing BMS contactors for mode reconfiguration. The loss model of the integrated converter considering the effect of magnetics integration is developed for design optimization. The integrated converter is optimized over a drive cycle to reduce the traction energy loss, weight, and loss. An automated controller is developed for the integrated converter to select the operating mode automatically based on the overall efficiency database to improve the traction efficiency. The dissertation is organized as follows:

In Chapter 2, different topologies are reviewed including separate traction converter and onboard charger. Different powertrain-charger integration approaches are also reviewed. The advantages and limitations of different topologies are explored.

In Chapter 3, the DC-DC integrated converter topology proposed for the research is presented. The advantages of the integrated converter topology are presented. Different operating modes of

the integrated converter are also described. The magnetics integration process for the integrated converter is defined as well. The capability of the integrated DC-DC converter operation in different modes is also demonstrated.

In Chapter 4, the impact of the magnetics integration in the integrated converter is modeled and analyzed for different modes of operation. The modeled current peaks are used to develop a loss model for the integrated converter for different modes of operation. The loss model is validated using a scaled-down integrated converter prototype. The advantage of different operating modes at different power level is highlighted as well to improve the traction efficiency.

In Chapter 5, an online transition algorithm is developed for traction operation to achieve the benefits of the integrated converter operating at different modes. The online transition algorithm ensures stable bus voltage for the inverter and eliminates power flow interruptions during the online transition. A modulation method is proposed to reduce the stress of the reconfiguration switch. As a result, the online transition method can be implemented for any type of reconfiguration switch available in the traction system.

In Chapter 6, an optimization method is presented to improve the integrated DC-DC converter design compared with a separate traction DC-DC converter and charger solution for a practical driving condition. An aggregated drive cycle is considered for the integrated converter optimization. The objective of the optimization is to reduce the traction power loss over the drive cycle, converter weight, and price. Different converter parameters including devices, cores, switching frequency, switching ripple, and magnetics integration approaches are considered. Using the Pareto front optimization, a design point is selected for high power integrated converter development.

In Chapter 7, a high-power prototype is developed based on the optimization method. The converter is tested for different operating modes for different output voltage and power levels. The converter loss model is validated for different power and voltage levels. A closed-loop automated controller is developed to ensure the automated transition between modes. The controller is also tested for different power level change where it automatically set the mode of operation and set the output voltage to achieve maximum traction efficiency.

In Chapter 8, the major takeaways of the integrated converter development process are presented. Possible future works are also described to improve the integrated converter design further.

2 Literature Review

Different topologies are presented in the literature for bidirectional boost converters for the powertrain, isolated DC-DC converters for the onboard charger, and for integrated converters where components are shared among powertrain and onboard charger. In this chapter, different topologies will be reviewed considering their advantage and disadvantages.

2.1 Bidirectional Boost Converter

The bidirectional boost converter is used for stepping up the battery voltage for the traction inverter based on the torque-speed requirement. Different types of bidirectional converters are studied for the EV powertrain application, which includes the single-phase, interleaved phase, and integrated magnetics-based solutions.

2.1.1 One-Phase Boost Converter

A one-phase boost converter consists of one inductor, two power semiconductor switches, and an input and output capacitor [53]. The schematic of the one-phase boost converter is shown in Figure 2.1. The main advantage of the one-phase boost converter is the operational simplicity and minimal component count. As a result, a one-phase bidirectional boost converter is used in the PCU of Toyota Prius, Honda Accord, BMW i3, and Toyota Camry [13, 20, 22]. The average power rating of the one-phase boost converter used in commercial HEVs is 30 kW [13]. However, for a higher power one-phase boost converter, the inductor gets large and inefficient since the full load current is passed through the boost inductor. A large core is required to prevent core saturation and to accommodate the thicker wire. High current rated devices are required to handle high current. Large DC bus filter capacitors are also required to filter the current ripple [54].

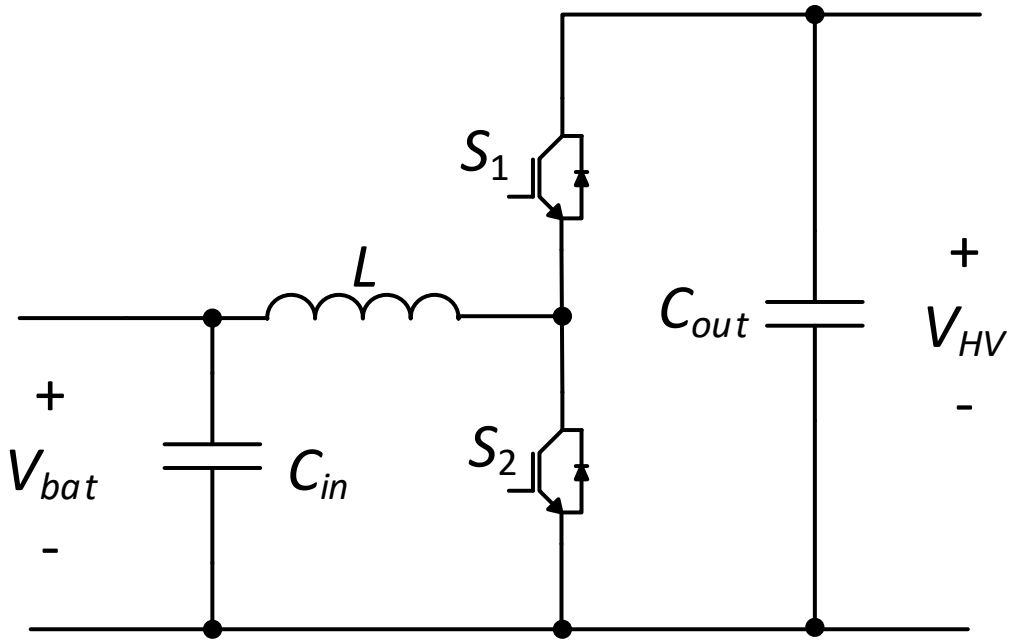

Figure 2.1. Bidirectional one-phase boost converter topology for Toyota Prius PCU [20].

2.1.2 Interleaved Boost converter

In an interleaved boost converter, several converter units operate in parallel in a phase-shifted manner [55, 56]. In this way, the total battery current can be distributed among the number of interleaved phases. The schematic of a two-phase interleaved boost converter is shown in Figure 2.2.

The advantage of the interleaved converter is that it reduces the input and output ripple current by interleaving the phase currents [57]. Since the current ripple is reduced, the required filter capacitance is reduced [21]. As the total current splits into multiple phases, the current rating of each switch is reduced. The total core size is reduced as well since the core saturation level is reduced and the total energy required to store in inductor is reduced as well. With the increased power demand of the traction drive system and the advent of high-speed controllers, interleaved

boost converters are investigated by OEMs as well to reduce the converter weight and volume [21]. However, the interleaved boost converter phase current ripple is greater than the input current ripple which results in higher AC power in the inductor loss compared to a one-phase boost converter [58].

2.1.3 Interphase Transformer (IPT) based Boost Converter

The main idea of the IPT based boost inductor is to use separate magnetics for DC and AC magnetization [59]. The schematic of the IPT interleaved boost converter is shown in Figure 2.3. The inductor is designed using a high flux core for DC magnetization. The interphase transformer is typically designed for AC magnetization using low core loss ferrite material [60, 61]. The main advantage of this topology is being able to optimize the AC and DC magnetics design separately for high efficiency and compact size [61]. The phase current ripple is either the same or smaller than the input current ripple depending on the duty cycle [58]. The input and phase current ripple frequency is twice that of the switching frequency.

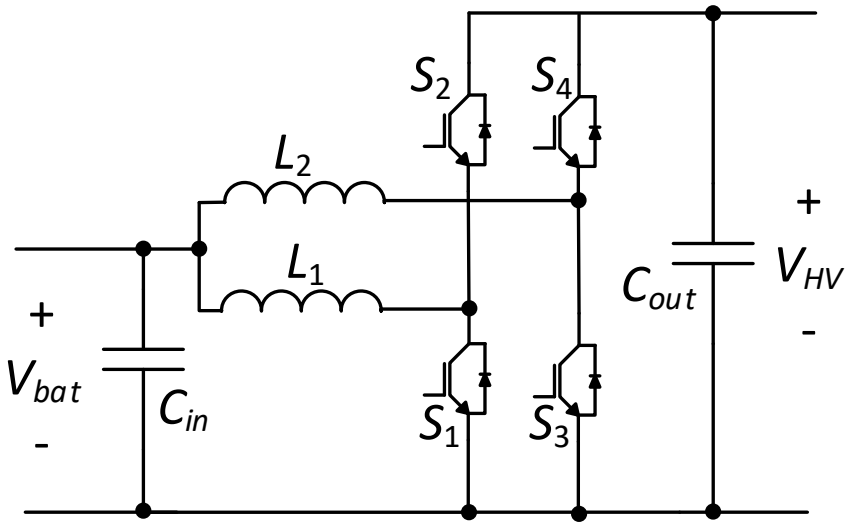

Figure 2.2. Interleaved boost converter [21].

In comparison to the same power rating and input current ripple of the interleaved boost converter, the IPT boost converter can improve efficiency and reduce weight [58]. However, to achieve the required magnetizing inductance, the converter performance is degraded due to the significant inter-winding capacitance [62]. The high DC bias input inductor also contributes to the high loss, weight, and price of the converter [58]. The inductor loss reduces the light load efficiency of the boost converter.

2.1.4 Integrated Magnetics (IM) Boost Converter

In the integrated magnetics boost converter, the inductors of the interleaved boost converter stages are integrated into a single low-loss core using a magnetic coupling technique [62]. An IM boost converter with a coupled inductor topology is shown in Figure 2.4.

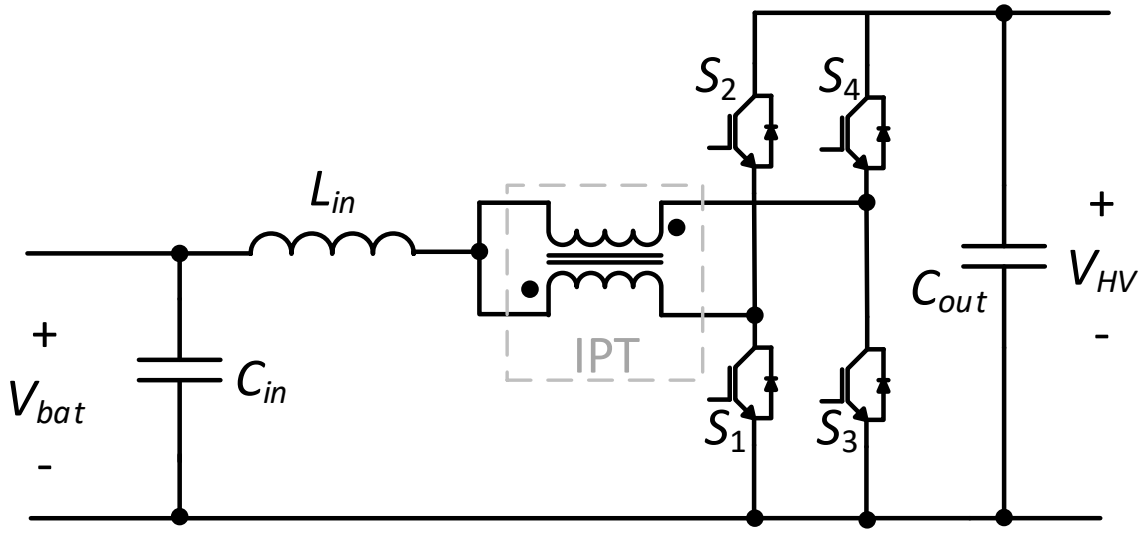

Figure 2.3. Interleaved boost converter with interphase transformer [59, 63].

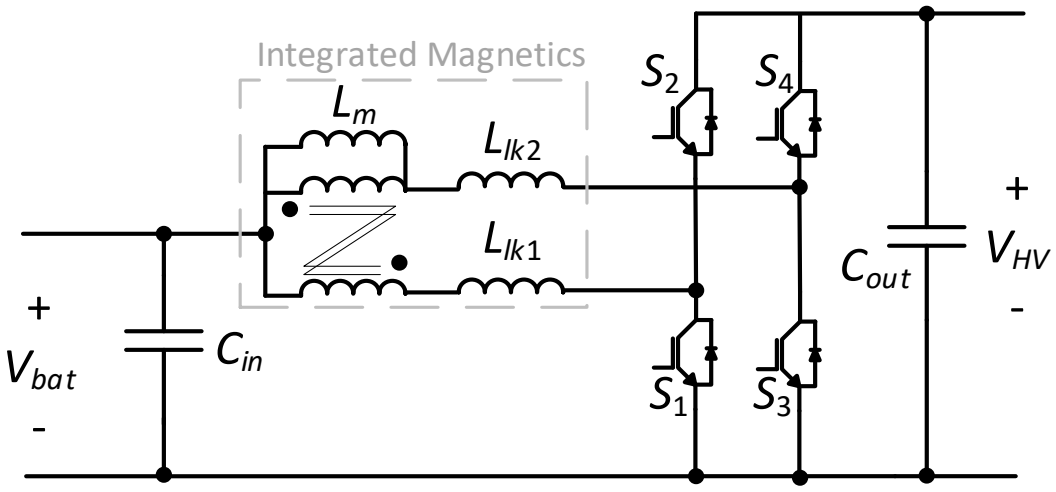

Figure 2.4. IM boost converter with coupled inductor [62, 64].

The main advantage of this topology is utilizing a single core for boost operation to reduce the price, weight, and volume of the boost converter. Since no DC inductor is used, the weight and volume can be reduced further [64]. The main challenge of the IM boost converter is the need for proper transformer winding and core geometry design to minimize the loss due to leakage [62]. The IM boost converter input current ripple is higher than the interleaved boost converter current ripple [65].

2.1.5 Composite Boost Converter

In the composite boost converter, shown in Figure 2.5, the boost converter efficiency is improved by limiting the boost converter duty cycle using parallel power converter stages [66]. The main drawback of the topology is the need for additional devices and magnetics for buck and DC transformer stages. The composite converter size is further reduced by using design optimization of the boost, buck, and DC transformer stage for standard drive cycle in [67].

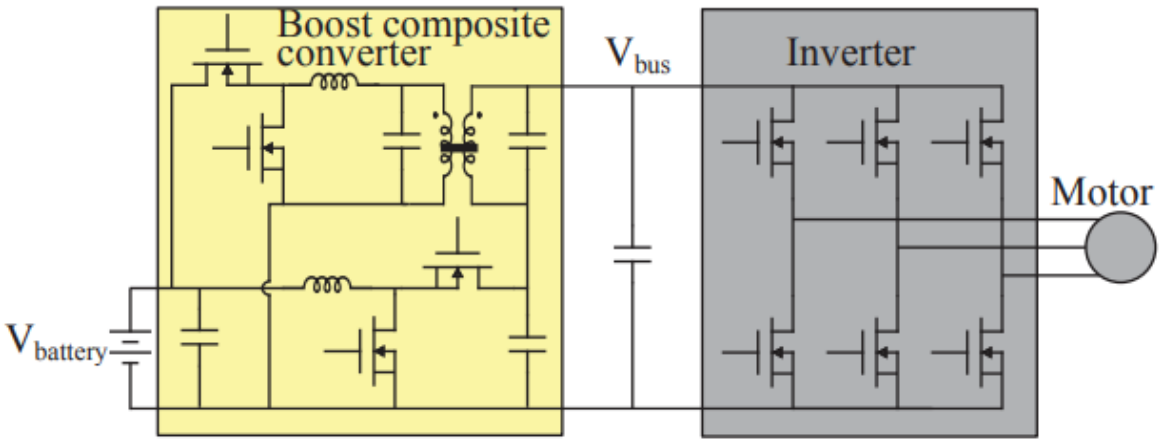

Figure 2.5. Composite boost converter topology [48].

2.2 Onboard Charger Isolated DC-DC Converter

The onboard charger has two major elements – a power factor correction unit and an isolated DC-DC converter [25]. The isolated DC-DC converter is responsible for controlling the power flow to the battery and providing galvanic isolation [29]. Traditional OBCs are unidirectional and only responsible to charge the battery from the grid [68]. However, with the increased demand for grid support during the peak hour, bidirectional converters are getting research attention [69, 70]. In this section, different topologies for isolated DC-DC converter are explored.

2.2.1 Phase Shift Full Bridge Converter

The phase shift full-bridge converter is commonly used as a unidirectional onboard charger topology [25, 26, 38]. The power flow is controlled based on the phase difference between the primary side phase legs [71]. The schematic of the converter is shown in Figure 2.10.

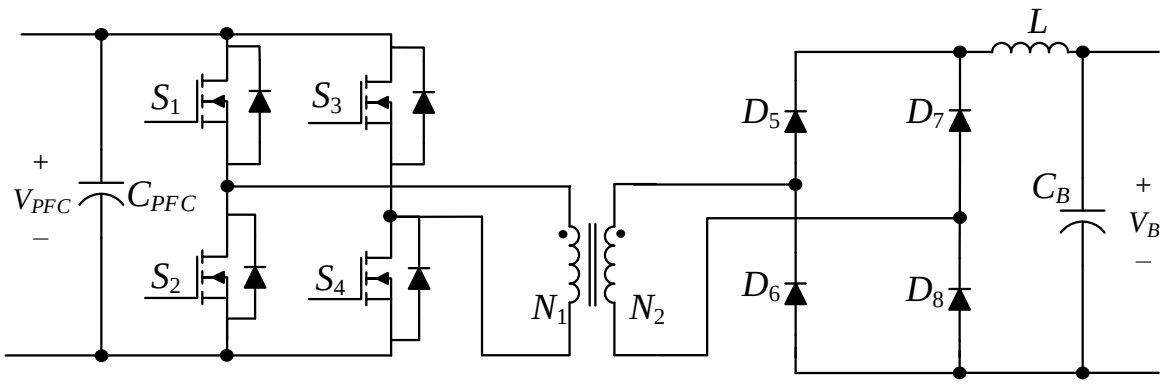

Figure 2.6. Phase shift full-bridge converter [72].

The phase shift full bridge converter has good characteristics including wide output voltage regulation and constant switching frequency PWM operation [73]. However, the circulating current that occurs during the freewheeling period is one of the drawbacks [74]. The converter can provide unidirectional power flow only. The secondary side diodes impact the efficiency of the converter. The phase shift full bridge efficiency can be improved by adopting hybrid switching techniques assisted by additional switches and passive elements [74].

2.2.2 Dual Active Bridge Converter

The dual active bridge (DAB) topology can be realized by combining two voltage fed full-bridge converters with a high-frequency isolation transformer [75]. An onboard bidirectional isolated DAB DC-DC converter is shown in Figure 2.7. Different modulation techniques are proposed for the dual active bridge converter topology including phase shift modulation, triangular modulation, trapezoidal modulation, and optimum modulation [15, 43].

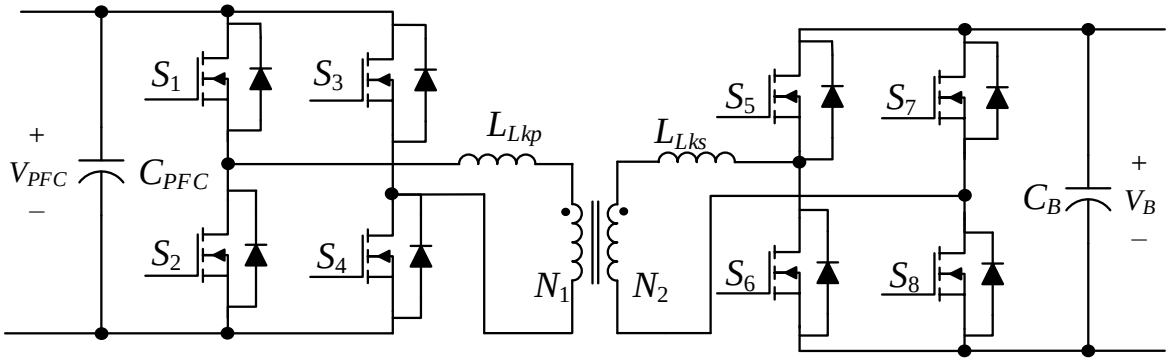

Figure 2.7. Dual active bridge charger topology for isolated DC-DC converter [76, 77].

The advantage of the DAB converter includes low device and component stress, inherent ZVS operation at the secondary side bridge, ZVS at the primary bridge at heavy load, high efficiency, bidirectional power flow capability, buck/boost capability, and good output voltage regulation [78]. However, the DAB converter is expensive since it requires eight active switches. Primary side ZVS is lost during the light load operation. Different modulation techniques and switching frequency variations are proposed for light-load efficiency improvement [43, 79].

2.2.3 CLLC and LLC Converters

The CLLC converter topology is used for bidirectional onboard chargers [80, 81] where LLC converter topology is used for the unidirectional grid to vehicle onboard charger [82]. The schematic of the CLLC converter topology is shown in Figure 2.8.

The advantage of the CLLC and LLC converters are high efficiency due to the extended soft switching operation [83, 84]. The main drawback is the output voltage regulation and switching frequency variation at different operating conditions [72]. Using an additional DC-DC converter can help the LLC converter to operate at the resonant point and regulate the battery voltage using the DC-DC converter [85].

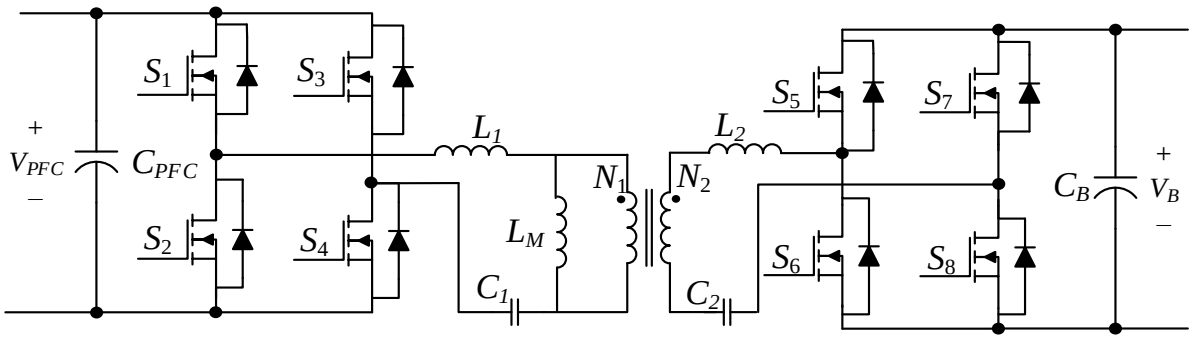

Figure 2.8. CLLC converter for EV charger [80, 81].

2.3 Integrated Converters

In an integrated EV converter, the charging system components and traction system components are shared to minimize the weight, volume, and price of some passive components of the charging system [38]. However, the drawbacks of integrated converters are the control complexity and extra mechanical contactor requirement. Different levels of integration are presented in the literature, including motor-based integration and DC-DC converter integration.

2.3.1 Motor Based Integration

The motor winding is used as an inductor in charging operation in different integrated converter topologies. The OBC weight and cost is reduced using the motor-based integration approach.

2.3.1.1 Motor Winding as Grid Filter Inductor

The motor windings can be used for the AC/DC portion of the EV charger. Both main traction motor and auxiliary motor including their associated power electronics of PEV or PHEV can be used for charging [86]. The auxiliary motor can be a three-phase generator, air compressor drive

motor or water pump motor. In Figure 2.9, motor and generator winding are used as grid filter inductors.

The price, weight, and volume are reduced as the traction semiconductor switches are used for charging and motor windings are used for filter inductor [86]. However, galvanic isolation is not provided in this topology. The motor winding also has high zero sequence resistance which can reduce the efficiency at high power. For the grid connection, the motor neutral point needs an additional mechanical disconnect [16]. The maximum power flow is also limited by the auxiliary motor power rating. Two three-phase Y-connected motors are required for the integrated charger. So, this method is not applicable for a delta connected motor. The inductance is not the same in all three branches due to the position of the rotor. The external inductors are added in series with the motor winding to get enough inductance for filter purposes as presented in [16].

The topology presented in Figure 2.9 is limited by the auxiliary motor power rating. To overcome the maximum power rating issue, an alternative implementation is shown in Figure 2.10 where only the main motor and inverter switches are used [86]. However, the main limitation of the solution is the requirement of an external diode leg.

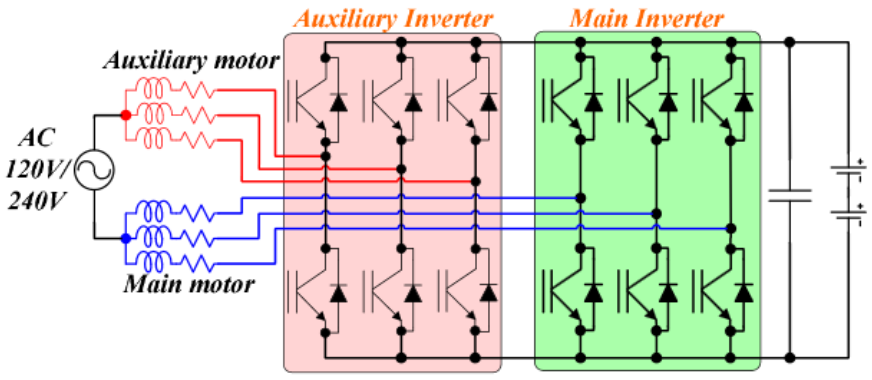

Figure 2.9. Integrated charger with two motors and two inverters [86].

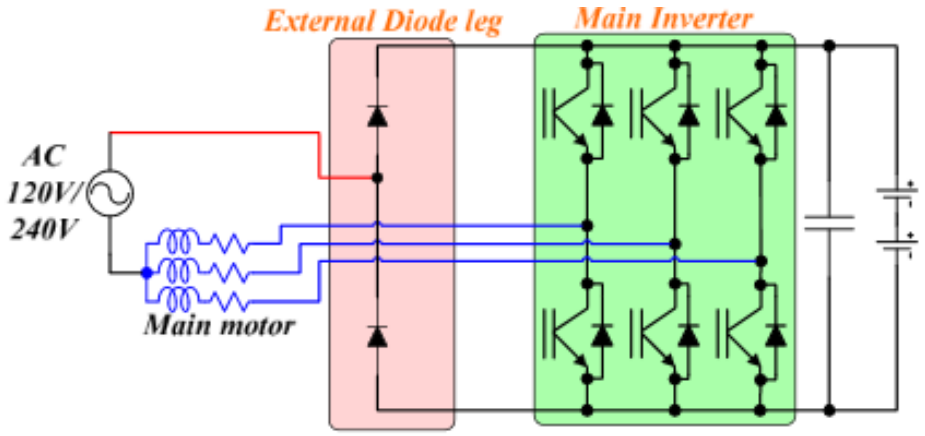

Figure 2.10. Integrated charger with one motor and one inverter [86].

2.3.1.2 Motor Winding and Powertrain Boost Converter as Grid Filter Inductor

The integrated converter proposed in [52] utilizes the main motor inductor and boost inductor for the grid filter inductance as shown in Figure 2.11. The need for the extra diode leg, shown in Figure 2.10, is avoided by the powertrain bidirectional boost converter phase leg and traction inverter. A single core is utilized for both the high-frequency isolation transformer and an auxiliary DC-DC converter for charging the low voltage battery.

Galvanic isolation is provided by the high-frequency isolation transformer. The converter price, weight, and volume are also reduced by utilizing the traction inverter and bidirectional converter. The main drawback of the circuit is the need for four mechanical contactors in the topology. The mechanical relays are bulky and expensive. The neutral point of the motor is typically grounded which needs to be reconfigured as shown in Figure 2.11.

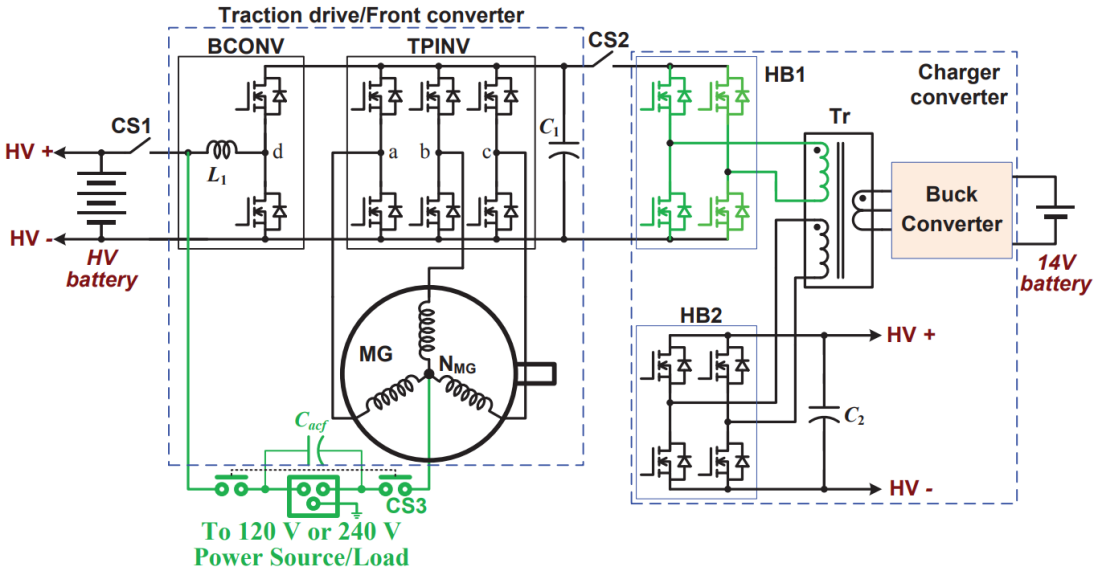

Figure 2.11. Integrated converter topology for vehicle traction and charging operation presented in [52].

2.3.1.3 Motor Winding as Grid Filter Inductor and Buck/Boost Inductor

An integrated switched reluctance motor (SRM) driver is presented in [87] where the motor winding is used for both grid filter inductor and Buck/Boost converter. The bidirectional charger topology is shown in Figure 2.12. In the charging mode, the purpose of Phase A and Phase B is to maintain the unity power factor for the grid requirement. The purpose of phase C is to regulate the battery voltage.

The advantage of this integration is that all motor windings and inverter are used for charging operation. The topology can reduce the price, weight, and volume of the converter. However, the main limitation of this topology is the need for 2 extra power switches for Phase C and the extra relay switch to disconnect the battery. Galvanic isolation during the charging operation is not available during the charging operation.

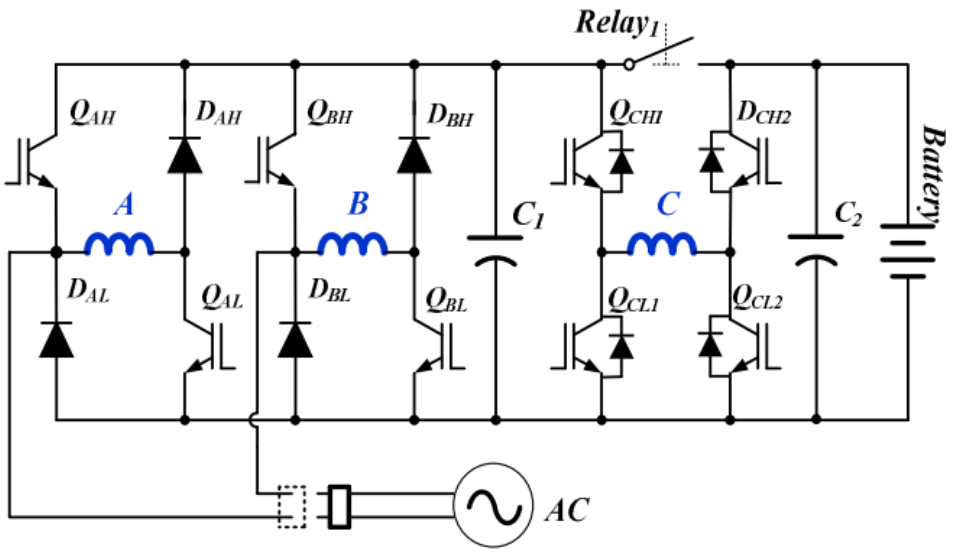

Figure 2.12. Integrated SRM drives with bi-directional converter [87].

2.3.1.4 Motor Winding as Buck/Boost Inductor

An integrated charger for the permanent magnet synchronous motor (PMSM) presented in [88] is shown in Figure 2.13. During motoring operation, only Relay 1 is connected, and the battery is directly connected to the inverter. For charging operation Relay 1 is disconnected and both Relay 2 and Relay 3 are connected to create a boost converter or interleaved buck converter depending on the grid voltage.

The advantage of this integrated functionality is to obtain the interleaved boost converter from the inverter. The limitation of the topology is the extra relays and reconnection requirement. The inductance is also not fixed and depends on the rotor position of the PMSM motor.

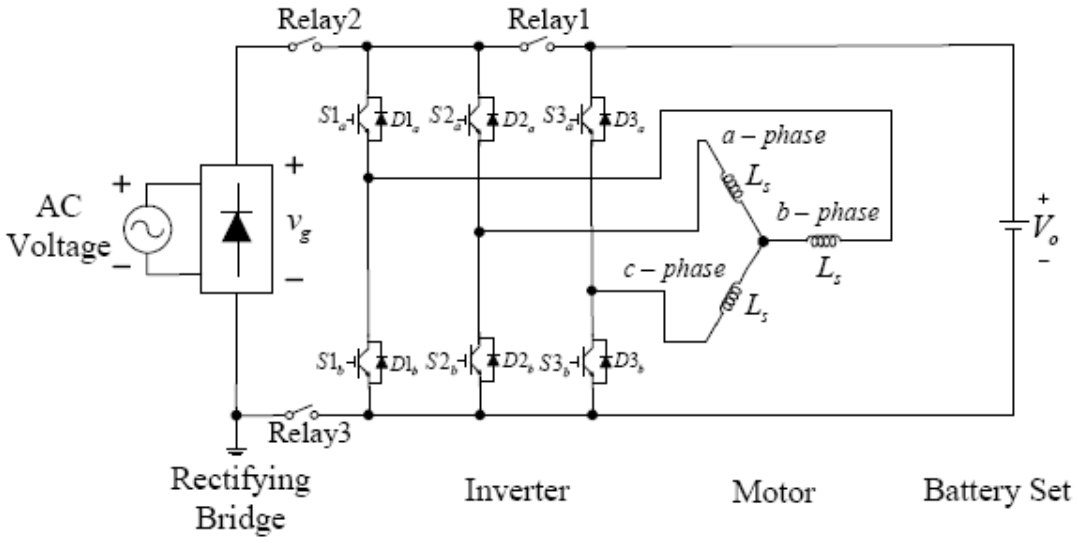

Figure 2.13. Integrated converter for PMSM [88].

2.3.2 DC-DC Converter Integration

The DC-DC stage of the traction drive system and the OBC is integrated by shared inductor, capacitor, and high-power switches. The OBC weight and cost is reduced by sharing passives and high-power switches.

2.3.2.1 Integrated Non-Isolated Powertrain Boost and PFC Boost Stage

An integrated converter utilizing the traction boost inductor and PFC boost inductor is presented in [89]. The powertrain boost inductor is designed to operate for the maximum traction inverter power requirement. As a result, the boost inductor is larger than the PFC boost converter. The converter topology is shown in Figure 2.14 where several diodes are used to control the power flow direction during the traction and charging operation.

The advantage of the topology is reduced weight and volume due to the elimination of the PFC boost inductor. However, the main drawback of the integrated converter topology is the

requirement of the extra devices. The traction power path contains two diodes and two MOSFETs which decreases the converter operating efficiency to 89% [89]. Since extra MOSFETs and diodes are used for converter reconfiguration, the required number of switches is high for this topology. As a result, the overall price is also high for this topology. The topology does not provide galvanic isolation as well.

2.3.2.2 Integrated Isolated Powertrain Boost and PFC Boost Stage

The topology proposed in [90] utilizes a low-frequency transformer for galvanic isolation as shown in Figure 2.15. The advantage of this topology is the reduction of the PFC boost inductor and elimination of diodes to direct the power flow during the powertrain and traction operating. In this topology, the powertrain boost converter is also used during the charging application. As a result, converter price, weight, and volume can be reduced. The main drawback of the integrated converter is the heavy and bulky line frequency transformer. Two MOSFETs are also used at the high-power flow path during the traction operation which will increase the converter loss and price.

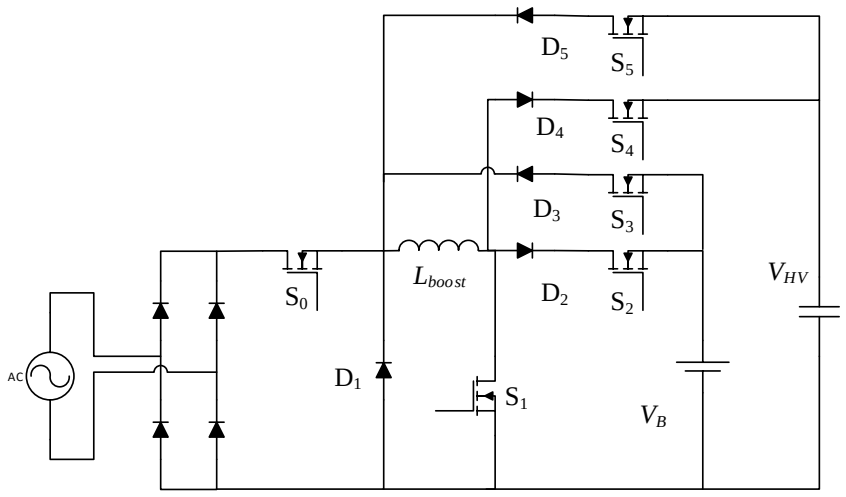

Figure 2.14. Integrated non-isolated powertrain boost and PFC boost converter [89].

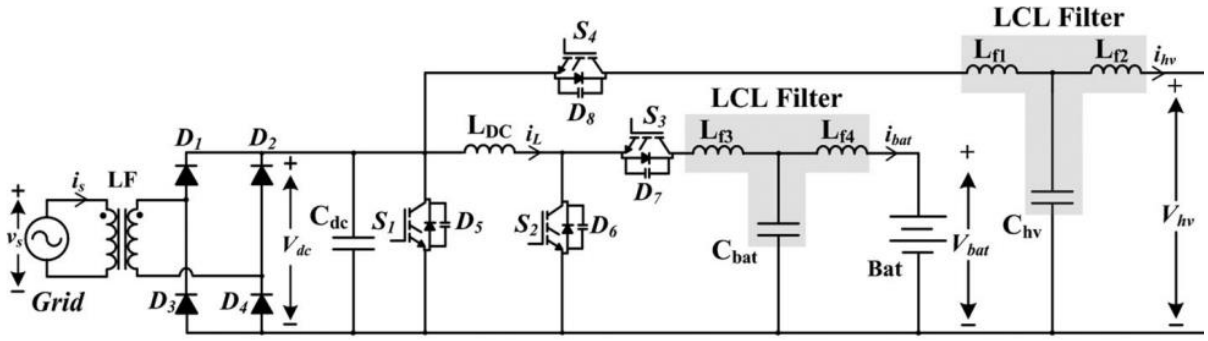

Figure 2.15. Integrated isolated powertrain boost and PFC boost converter in [90].

2.3.2.3 Integrated Powertrain Boost and Phase Shift Full Bridge Inductor

The integrated converter topology presented in [91] combines powertrain boost converter and phase shift full bridge inductor as shown in Figure 2.16. The topology can be reconfigured for the wireless power transfer (WPT) system. The diodes of the powertrain boost converter switches are also used for the secondary side of the phase shift full-bridge converter. The topology provides galvanic isolation using a high-frequency transformer. Five single-pole double-throw (SPDT) mechanical contactors are used for reconfiguration among traction, wired, and WPT modes.

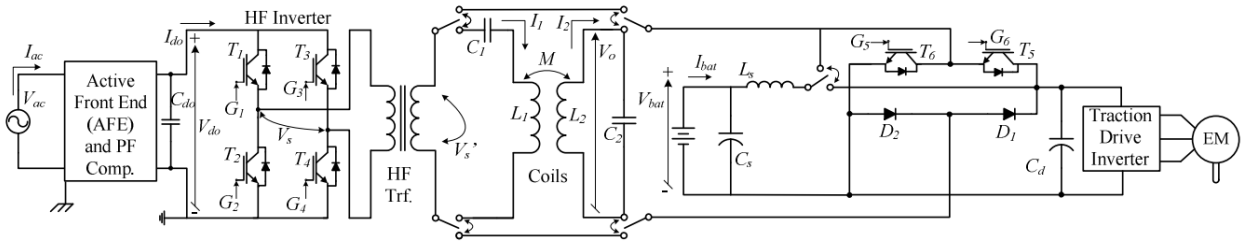

Figure 2.16. Integrated powertrain boost and phase shift full bridge inductor [91].

2.3.2.4 Integrated Magnetics for Boost and Isolated DC-DC Converter

The concept of integrated coupled magnetics can also reduce the number of semiconductor switches and magnetics requirements as proposed in [92, 93]. The integrated converter topology is shown in Figure 2.17. The strongly coupled inductor is used during boost operation while the transformer is deactivated. On the other hand, the coupled inductor exhibits very low leakage inductance during the isolated DC-DC converter operation and the transformer excitation is utilized for power flow from the rectified grid voltage towards the onboard battery.

The integrated converter can reduce the number of magnetic components and semiconductor switches by half compared to a conventional system [93]. The converter can provide galvanic isolation as well during the charging operation. The converter also has a lower number of semiconductor switches and magnetic components. The number of magnetic cores can be further reduced by incorporating the series DAB inductors into the transformer leakage inductance.

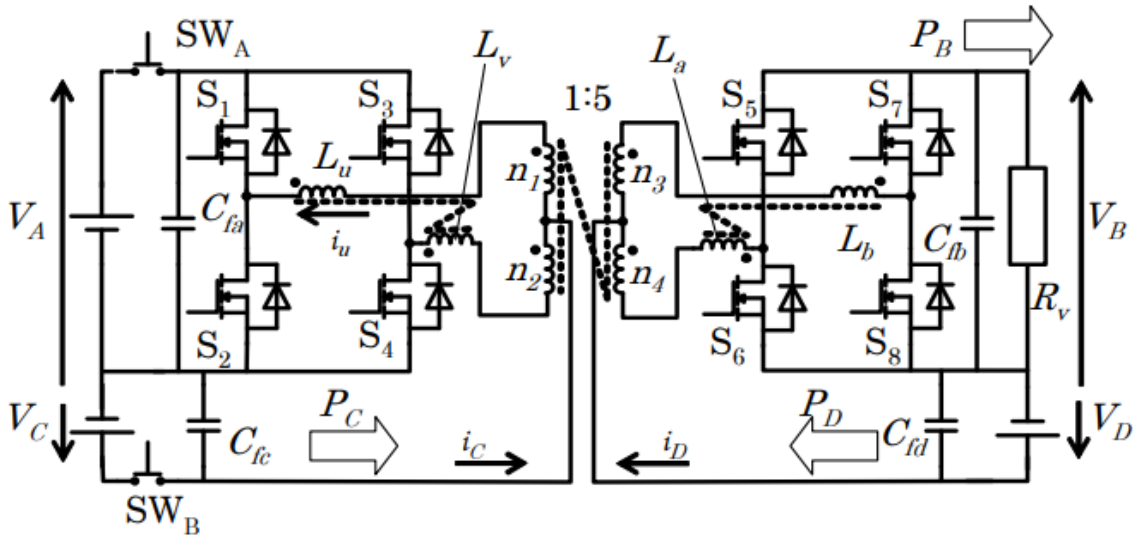

Figure 2.17. Integrated Magnetics for Powertrain Boost and Isolated DC-DC Charger [92, 93].

2.4 Research Gap

To compare the current state of the art of the integrated DC-DC converter topologies, the efficiency and the output power per core weight is plotted in Figure 2.18. The traditional integrated converter efficiency is low. The separate traction DC-DC converter topologies with various DC-DC OBC chargers are also plotted in Figure 2.18. The proposed integrated converter is designed to improve the existing integrated DC-DC converter efficiency and achieve similar efficiency compared with the separate traction DC-DC converter. By combining the power switches and magnetics, the cost and weight of the integrated DC-DC converter can be reduced as well.

Inductor and transformer are important for the integrated DC-DC converter design. The magnetics must be carefully designed and optimized by identifying different core loss mechanism.

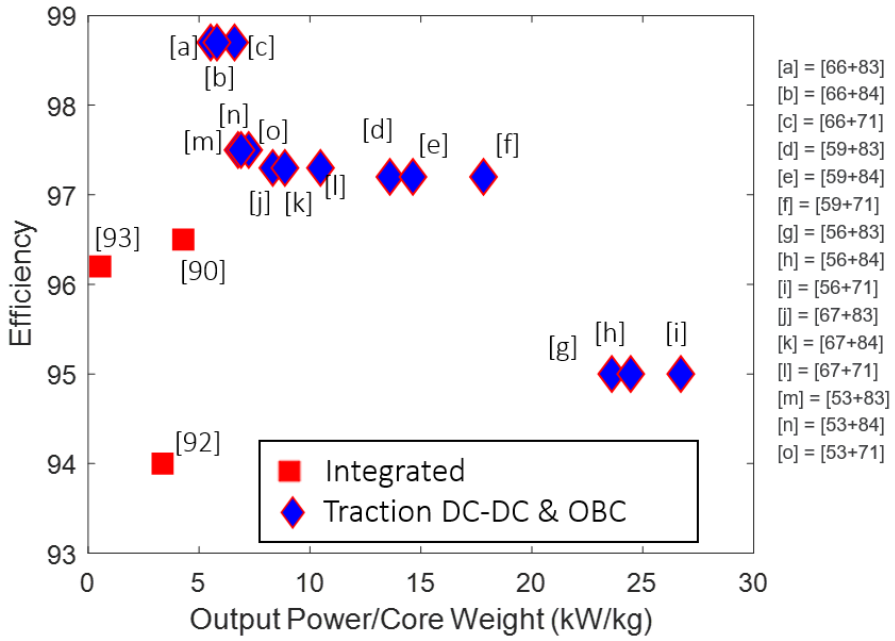

Figure 2.18. Comparison between integrated DC-DC converter, and separated traction DC-DC with the DC-DC stage of OBC.

2.5 Core Material

A low core loss material is essential to increase the power conversion efficiency of the EV powertrain. Different core materials including iron powder core, ferrite core, amorphous core, and nanocrystalline cores are reviewed for EV applications [94-97]. The core loss density at different amplitudes for 100 kHz switching frequency is reported in [96] and shown in Figure 2.19. The nanocrystalline material (Vitroperm500F) can provide lower core loss compared with iron-powder and amorphous material. The ferrite material (3C93) also exhibits low loss at lower magnetic flux density. However, the saturation flux density of ferrite material is around 0.4 T which is less than half of the nanocrystalline material flux density. As a result, nanocrystalline is getting attention for both inductor and transformer applications below 100 kHz. The gapped core has the flexibility to increase the saturation limit by increasing the air gap of the core. However, the nanocrystalline core is conductive. Conductive cores are laminated to prevent internal circulating current up to a certain frequency [98]. As a result, the flux lines near the air gap cause additional lamination loss.

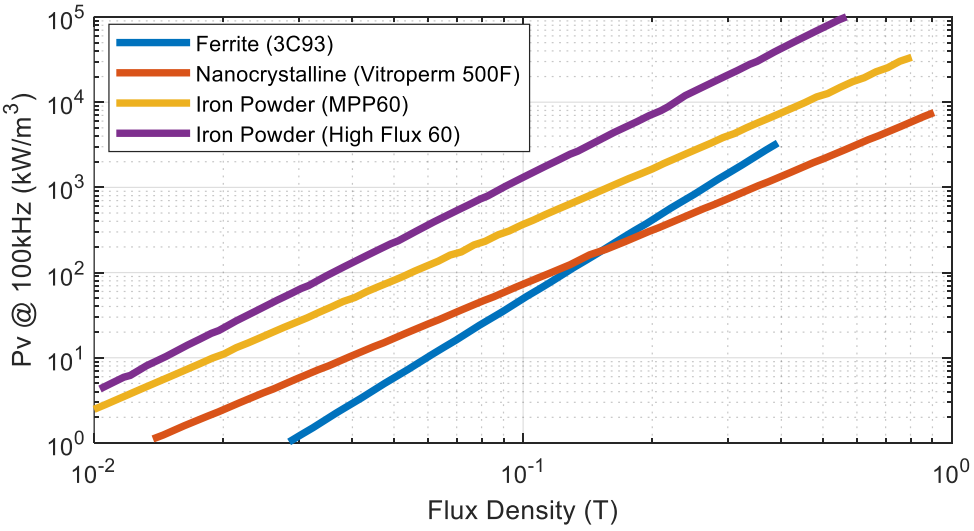

Figure 2.19. Core loss comparison among different core materials [96].

2.6 Lamination Loss in Laminated Core

The lamination is designed to prevent internal circulating current for a frequency of interest. The fringe flux in the airgap cause eddy current in the outer lamination of the laminated core as shown in Figure 2.20 [99]. Gap loss is predicted empirically for steel laminated core which overestimates the loss for the amorphous core [100]. The gap loss model is also developed using 3D finite element analysis (FEA) homogenization approximation for nanocrystalline inductors [99]. The homogenization approximation approximates the core as a bulk material with flux flow in a certain direction. The challenge is the computational complexity to simulate the losses individual laminations of a laminated core [101]. The lamination loss in Nanocrystalline transformers with a very small air gap (20 µm -160 µm) can be neglected [102]. However, the transformer winding orientation and leakage fluxes contributes to the lamination loss presented in [103] which is ignored in empirical models. The lamination loss for the transformer with the large air-gap nanocrystalline core need FEA modeling considering the winding orientation.

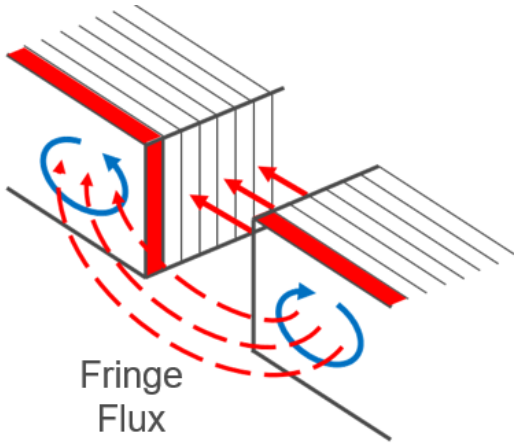

Figure 2.20. Fringe flux induced eddy current near the air gap in the laminated core.

2.7 Power Converter Optimization

Optimization for a power converter is investigated to improve the power converter design by reducing the converter size and increasing efficiency [45, 46]. The mathematical multi-objective optimization process can be gradient-based or metaheuristic based [104, 105]. The main drawbacks of the gradient-based multi-objective optimization for power converter design are the possibility of iteration becoming stuck at local minimums and difficulty to optimize for nonlinear variables [46]. The nonlinear variables are generated from power converter components including different device on-state resistance, switching loss information, and device price. As a result, the Pareto front optimization and genetic algorithm are used for power converter loss, weight, and size optimization to find a global solution [45, 46, 106]. The magnetic design including inductors and transformer is improved by the Pareto front optimization method [107-109]. Optimization methods are also proposed for traction loss reduction at different drive cycles [48, 110].

In EV integrated converter topologies, the efficiency is often sacrificed to reduce the converter weight and price [89]. The optimization of the integrated converter combining the traction and charging functionality is not widely reviewed in the literature. The components of the existing integrated converters in literature are designed for maximum load conditions. Integrated converter optimization can provide designers with the trade-off between efficiency, weight, volume, and price. Integrated converters can be optimized for the targeted drive cycle as well which can improve overall traction performance of EVs.

2.8 Research Approach

The main objective of this research work is to design an integrated DC-DC converter which can reduce the power conversion loss, weight, and price compared with separate DC-DC traction converter and charger. To achieve the objective, the design steps are as follows.

First, the interleaved boost inductor and the high-frequency isolation transformers of the DC-DC converter presented in [92, 93] are combined on the same nanocrystalline core to create a hybrid transformer. The interleaved boost stage power devices are reused for the DAB stage as well. To reconfigure the integrated converter functionality, existing BMS contactors are used. With this configuration, the integrated converter needs to be verified for both boost and DAB mode of operation. In this way, the converter cost can be reduced by sharing the expensive magnetics and power semiconductor switches. The converter weight can be reduced as well by sharing the same magnetic core and heat sink for power modules.

Second, the integrated converter primary and secondary current waveform are modeled considering the effect of the hybrid transformer. The current peaks are essential for loss modeling for the integrated converter. The hybrid transformer loss in the presence of the fringe effect needs to be considered as well. The loss model is verified using a small power prototype. The hybrid transformer for the DAB stage can be designed to provide better efficiency at light load compared to the traction boost converter. In this way, operating in DAB mode in traction operation provides potential efficiency improvement.

Third, the traction loss reduction by using both boost and DAB mode requires online transition during the traction operation. The online transition is challenging since the existing BMS contactor is planned to be used for the integrated converter. The BMS contactor takes significant time to connect and disconnect. A modulation technique is developed to ensure a seamless transition,

eliminate power flow interruption, and reduce the current and voltage oscillation during the transition. In this way, the traction power loss can be reduced during traction operation along with the potential weight and price reduction.

Forth, design optimization can further improve the integrated converter design. For a given drive cycle, different integrated converter designs are evaluated to reduce traction energy loss, weight, and price. The optimization method is developed to generate Pareto front results where the design is selected for high power prototype development.

Finally, a closed-loop automated controller is developed to operate the high-power integrated converter. The controller automatically decides to perform the automated transition for power and voltage levels. The loss model is validated for the high-power integrated converter prototype.

2.9 Summary

In this Chapter, different DC-DC converter topologies are presented for separate powertrain and onboard charger. The advantages and limitations of different topologies are also explained. Different integrated converter solutions including the motor-based integration and DC-DC converter-based integration are explored. Although the integrated converter can reduce the converter price, volume, and weight by sharing different charging and powertrain components, extra mechanical contactors or high-power semiconductor switches increase the price and volume of the converter. To design the integrated DC-DC powertrain-charger, the challenges of the existing integrated DC-DC converters are also investigated.

3 Integrated Powertrain-Charger DC-DC Converter

In conventional EV power conversion architecture with an onboard charger, the charging and powertrain circuits are separate as shown in Figure 3.1. During charging operation, the battery contactors (S_{11} – S_{12}) are connected and the EV is charged from the AC grid through the power factor correction circuit (PFC) and an isolation transformer. The isolation transformer is used to isolate the AC power ground from the EV ground. Separately, a DC-DC converter is commonly used to boost from the high voltage battery to a DC bus used as the input to the motor drive inverter. The inverter bus voltage also varies at different torque and speed demand by the traction motor to improve the traction efficiency [111-113]. This discrete implementation of each converter requires separate magnetic devices for the isolation transformer of the OBC and inductors of the boost converter. These magnetics increase weight and volume of the EV which impact the overall vehicle performance and consumes usable space. Additionally, each converter requires separate cooling systems.

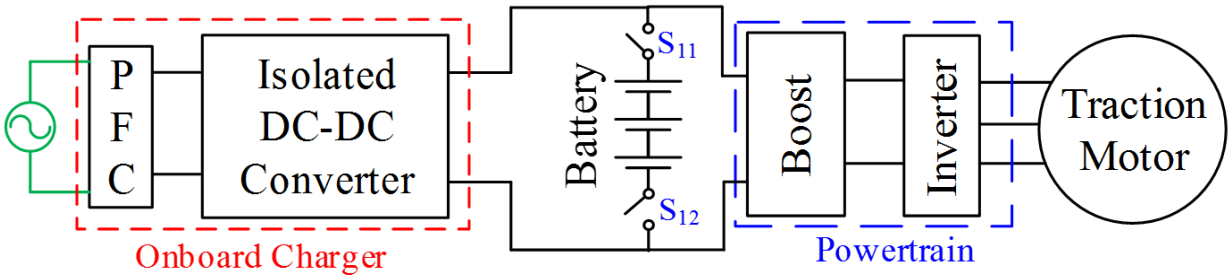

Figure 3.1. Conventional EV charger and powertrain converter architecture.

3.1 Integrated Converter Topology

The integrated converter topology proposed for investigation is shown in Figure 3.2. The DC-DC stage of the traction system and the onboard charger are integrated. The integrated converter topology incorporates both traction and charging functionality. The existing BMS contactors (S_{11} and S_{12}) are used for the functionality reconfiguration. The DC-link capacitor in the separate onboard charger and powertrain converter is bulky [114]. In this integrated converter topology, the PFC converter and inverter are connected at the same node. As a result, the same DC link capacitor can be shared.

The circuit diagram of the proposed integrated converter is shown in Figure 3.3. The boost inductors and the high-frequency isolation transformers of the DC-DC converter in [92, 93] are combined to create a hybrid transformer. The leakage inductance is used for DC-DC converter power flow where the magnetizing inductance is used as boost energy storage inductor.

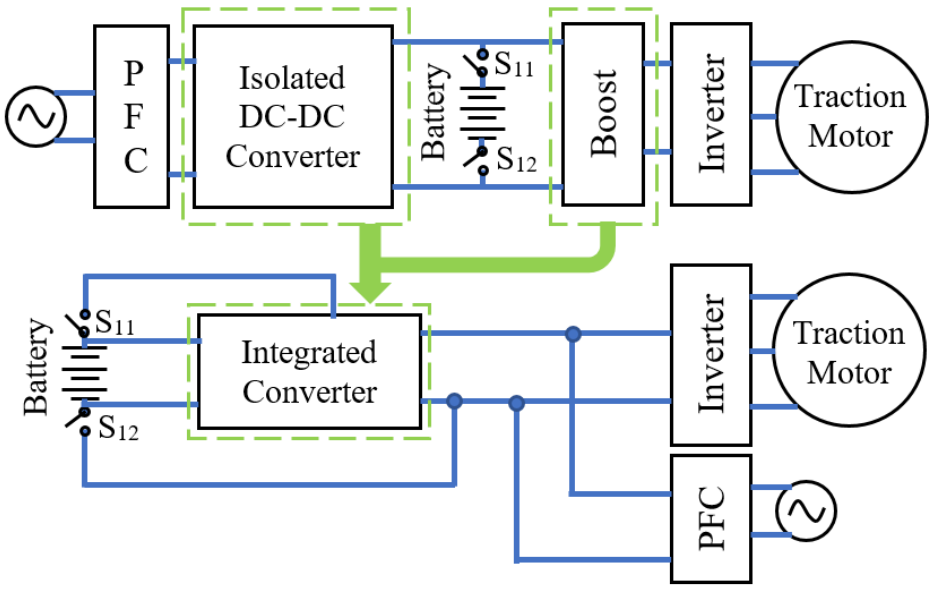

Figure 3.2. Integrated powertrain-charger DC-DC converter architecture.

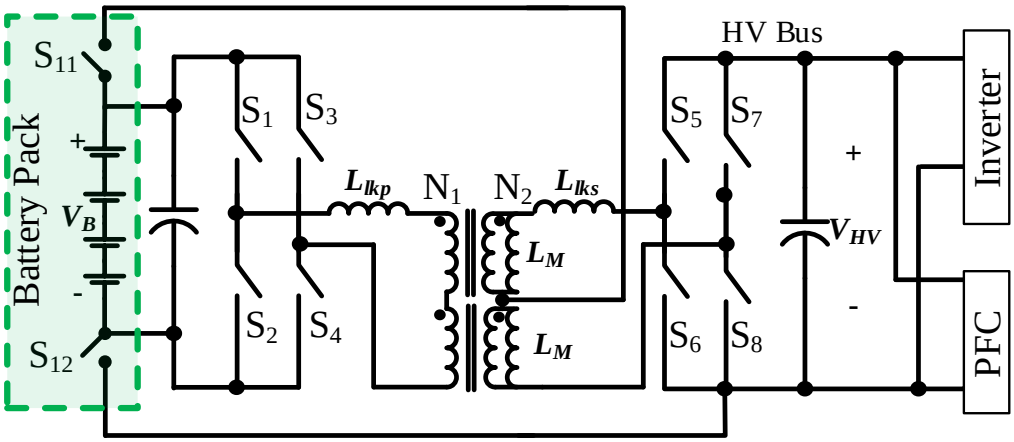

Figure 3.3. Integrated powertrain-charger DC-DC converter schematic.

The integrated converter has eight high power semiconductor switches (S_1-S_8). The four switches, S_5-S_8, are the basic powertrain boost converter switches that can handle the full inverter power. A DAB converter is used for the isolated DC-DC converter due to bidirectional power flow capability, zero voltage switching operation, and low stress on the power semiconductor switches. The DAB secondary side transistors are shared with the boost converter, reducing the total number and semiconductor area of power devices.

3.2 Charging Operation

During the battery charging operation using the proposed integrated converter, all eight switches (S_1 – S_8) are modulated, and the converter functions as a DAB. Galvanic isolation is maintained by disconnecting S_{11} and S_{12}. The charging operation is shown in Figure 3.4. The converter transfers power from the HV bus to the battery using the phase shift between the primary side and secondary side of the converter as shown in Figure 3.5. For a lossless DAB, the power flow equation is

$$P_{DAB} = \frac{nV_B V_{HV}\phi(\pi - |\phi|)}{2f_{sDAB}L_{lk}} \tag{3-1}$$

where n, V_B, V_{HV}, ϕ, f_{sDAB}, and L_{lk} are the transformer turns ratio, battery voltage, inverter bus voltage, phase shift, DAB switching frequency, and equivalent leakage inductance of DAB, respectively.

The phase shift is always limited below $\frac{\pi}{2}$ to prevent excessive circulating currents. The required phase shift is calculated from the solution of the quadratic equation of the DAB power flow

$$\phi = \frac{\pi}{2}\left(1 - \sqrt{1 - \frac{8f_s L_{lk}|P|}{nV_B V_{HV}}}\right) \tag{3-2}$$

The maximum power flow during the DAB operation at different operating conditions is

$$P_{DAB_{max}} = \frac{nV_B V_{HV}}{8f_{sDAB}L_{lk}} \tag{3-3}$$

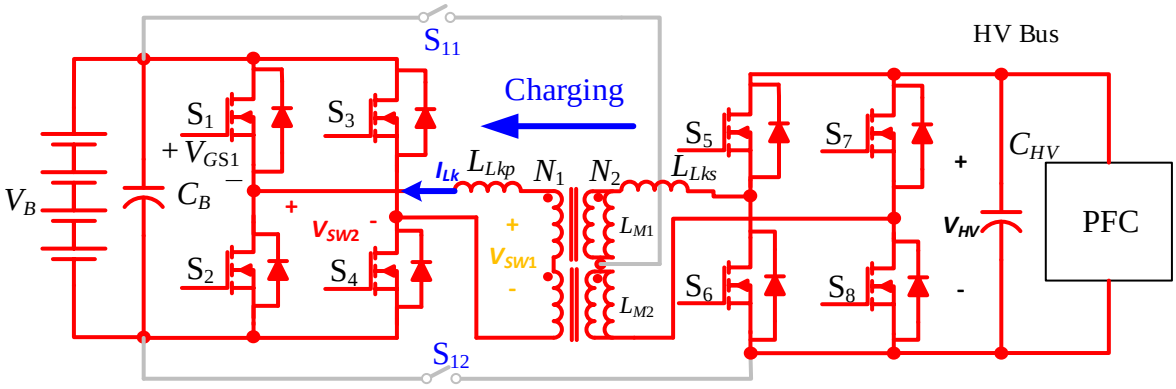

Figure 3.4. Integrated converter working as a DAB converter in charging mode.

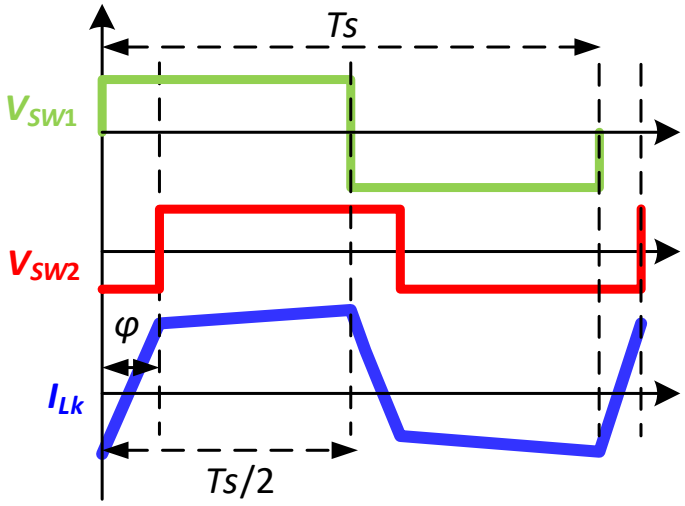

Figure 3.5. Integrated converter waveform in DAB mode.

3.3 Traction Operation

During traction operation, the integrated converter can be reconfigured as a boost or DAB converter. The boost converter is designed to support efficient high-power traction operation. The DAB converter is rated for charging power which is typically a fraction of the traction boost converter. As a result, the DAB converter can be designed specifically to improve the light load efficiency of the traction operation.

In a conventional topology with separate charging and powertrain converter, only the boost converter is available for traction operation. As a result, the traction boost converter design is largely determined by heavy load operation. The proposed integrated converter provides the opportunity to design the DAB converter for light and boost converter for heavy load.

3.3.1 Traction Boost Mode

The integrated converter can be configured as a boost converter by connecting the BMS contactors S_{11} and S_{12} as shown in Figure 3.6. In this mode, four switches ($S_5 – S_8$) are modulated and the other four switches ($S_1 – S_4$) are turned off. The battery voltage is connected at the center point of the integrated transformer by the BMS contactor. The self-inductance of the secondary winding of the transformer is used as the boost inductance.

The switching waveform and inductor current waveform during the interleaved boost converter operation are shown in Figure 3.7. The power flow of the boost converter is controlled by the traction inverter. The required secondary side self-inductance for the boost converter is

$$L_{B1,2} \geq \frac{V_{HV} - V_B}{\Delta I_M f_S V_{HV}} \tag{3-4}$$

where V_{HV}, V_B, f_S and ΔI_M are the HV bus voltage, battery voltage, switching frequency, and allowable boost current ripple, respectively.

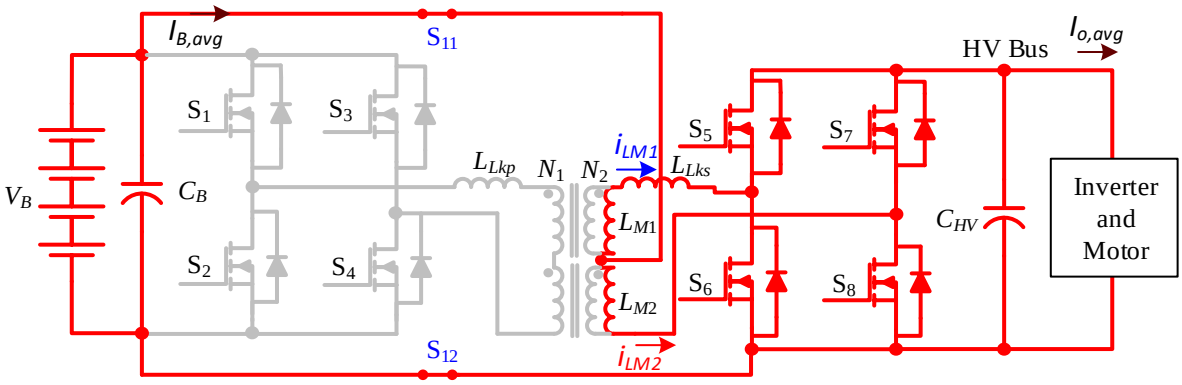

Figure 3.6. Integrated EV DC-DC converter configured as boost configuration.

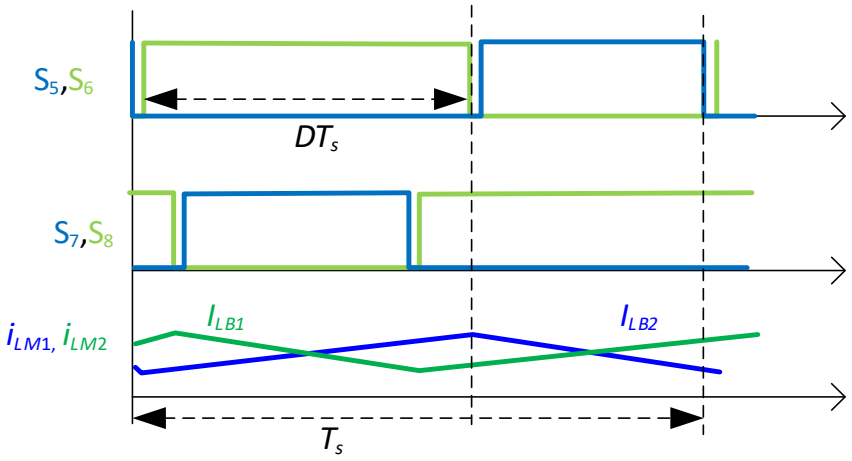

Figure 3.7. Interleaved boost converter in traction mode.

The output voltage of the boost converter is set by the duty ratio

$$V_{HV} = \frac{1}{1-D} V_B \tag{3-5}$$

where D is the converter duty ratio as illustrated in Figure 3.7.

3.3.2 Traction DAB Mode

During powertrain operation, the efficiency of the interleaved boost converter decreases at low power and high conversion ratio due to the large switching loss and high currents present in a high step-up boost. Due to the bidirectional power flow capability of the DAB converter, the DAB can be used for traction operation as well. To improve the light load efficiency further, the DAB operating mode can be used when the output power is within the achievable range of the DAB converter. The configuration in the traction mode of the DAB converter is shown in Figure 3.8. The DAB converter is operated in phase shift modulation as shown in Figure 3.8.

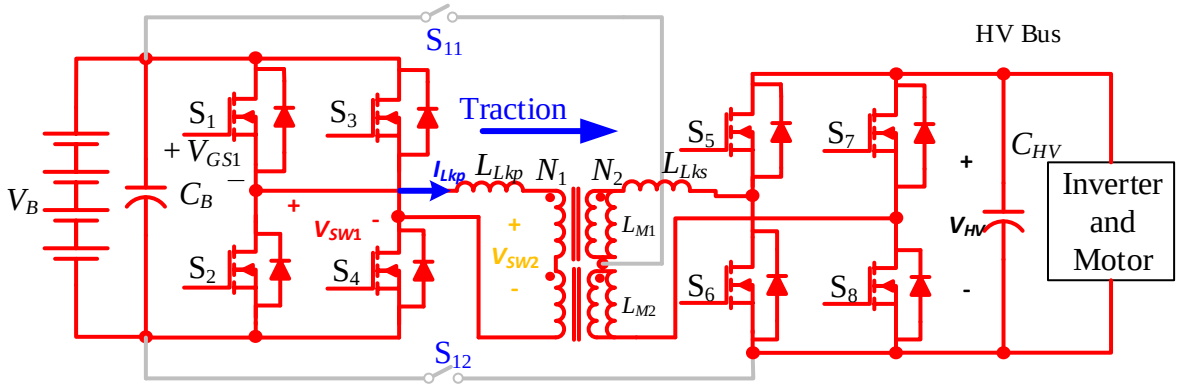

Figure 3.8. Integrated EV DC-DC converter working as a DAB converter in traction mode.

3.4 Hybrid Transformer

A hybrid transformer design is critical for the integrated converter design. The same core is used for booth boost inductor and high-frequency transformer. The boost inductor is realized by the self-inductance of the secondary side of the DAB transformer. The DAB power flow is controlled by using the leakage inductance of the integrated magnetic component.

The B-H curve of the hybrid transformer of the integrated powertrain-charger converter is shown in Figure 3.9. In the boost mode, the flux through the core is small AC ripple shifted by a DC value. The air gap is set to prevent the core saturation at the maximum peak current during the boost converter operation. During the DAB converter operation, the flux through the core is AC.

This design interdependency leads to inherent tradeoffs in performance between the two operating modes. As shown in Figure 3.10, the portion of the magnetic winding area dedicated to the boost, $K_{u\,\mathrm{boost}}$, will have a direct relationship with the boost efficiency but inverse relationship with the DAB efficiency. The fill factor for the boost windings can vary,

$$0 < K_{u\,boost} < 1 \tag{3-6}$$

Since the boost converter is designed for high power operation, a larger portion of the window area is generally dedicated to it to accommodate higher AWG wires. As such, the definition of optimum design is dependent not only on traditional tradeoffs between efficiency and power density but also on tradeoffs between performances of each operating mode. Based on the transformer primary and secondary winding configuration, the leakage inductance of the DAB transformer can be modified which also impacts the efficiency of the DAB converter operation.

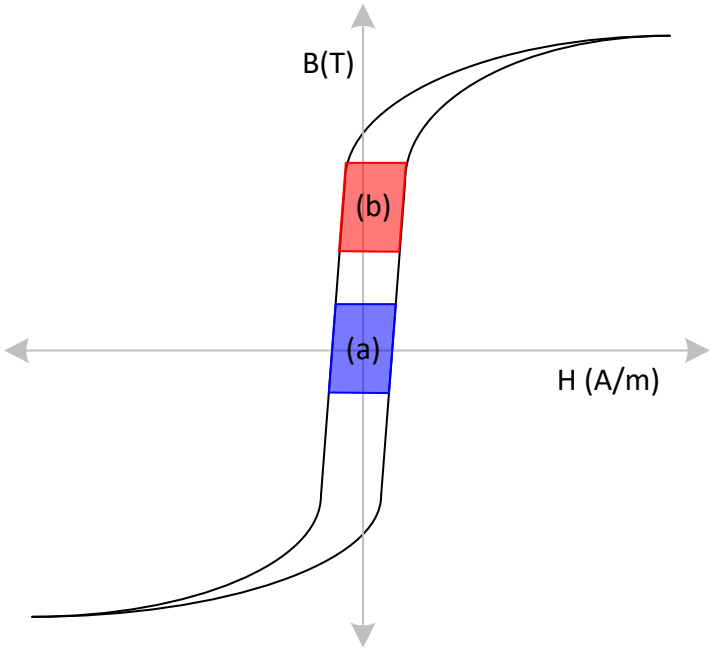

Figure 3.9. B-H curve of the magnetic core for (a) DAB transformer operation and (b) Boost converter operation.

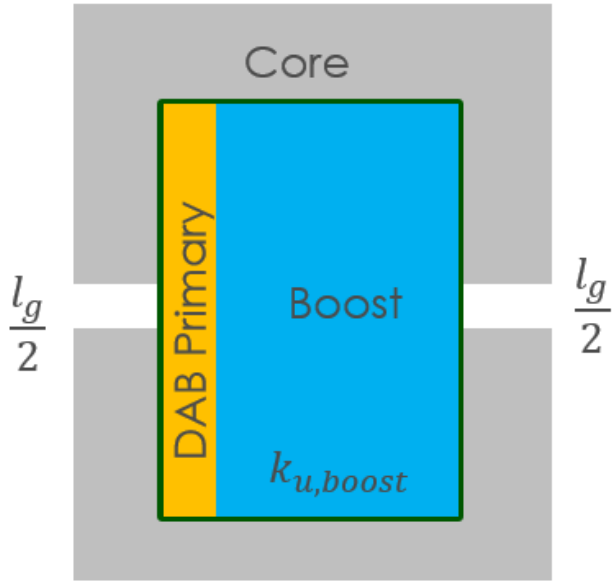

Figure 3.10. Hybrid transformer fill factor for the Boost converter and DAB primary winding.

The self-inductance of the hybrid transformer is used as the boost inductance. The self-inductance is the combination of the secondary side magnetizing inductance and leakage inductance of the integrated transformer. The boost inductance is expressed as a function of the boost converter switching frequency using fixed inductor current ripple approximation.

The maximum magnetic flux density is set for the boost converter based on the saturation flux density and B-H curve characteristics [97]. The number of turns, winding area, and required airgap to design $L_{B1,2}$ depend on the core geometry, core material, switching frequency, ripple, and winding design.

Due to the presence of the air-gap, the fringe flux changes the effective air gap length and core cross-sectional area. As a result, the fringe factor is considered while designing the inductance value. The fringe factor given in [115] is

$$F = 1 + \frac{l_g}{\sqrt{A_c}} ln\left(\frac{2C}{l_g}\right) \tag{3-7}$$

where l_g, A_c, and C are the total air gap, core cross-sectional area, and the window height of the core as shown in Figure 3.11. The boost inductance considering the fringe factor is

$$L_{boost1,2} = F\left(\frac{\mu_0 A_c N_s^2}{l_g}\right) \tag{3-8}$$

where N_s is the number of turns of the secondary winding of the integrated transformer. To prevent the core from saturation, the maximum magnetic flux density is

$$B_{max} = F\left(\frac{\mu_0 N_s I_{max}}{l_g}\right) \tag{3-9}$$

where I_{max} is the maximum boost phase current considering the ripple and DC average current.

The DAB converter is used to improve the light load high conversion ratio efficiency of the boost converter. For unity conversion DAB turns ratio, the number of primary turns is

$$N_p = N_s \frac{V_B}{V_{HV}} \tag{3-10}$$

The cross-sectional area of the DAB winding depends on the remaining portion of the area for the DAB converter. The remaining portion of the window area is

$$K_{u\,DAB} = 1 - K_{u\,boost} \tag{3-11}$$

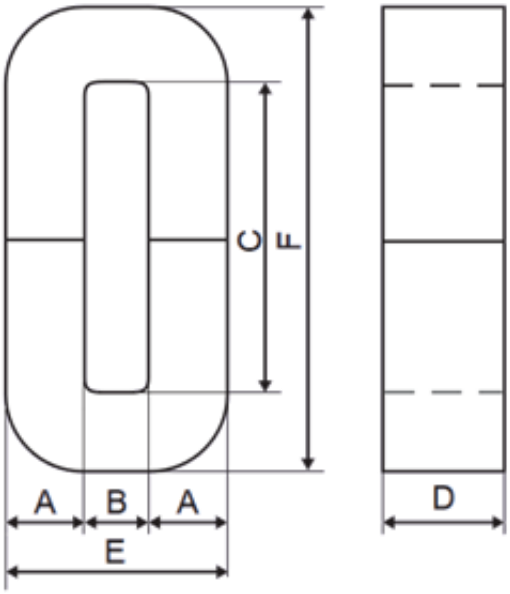

Figure 3.11. Core geometry of the Hitachi F3CC nanocrystalline core.

The DAB converter leakage inductance depends on the winding arrangement. The leakage inductance can be calculated using Finite Element Analysis (FEA). The impact of the hybrid transformer on the DAB converter performance will be analyzed details in the next chapter.

3.5 Experimental Results

To verify the integrated converter functionality experimentally, a low power prototype is developed where the parameters are given in Table 3.1. To implement the high-frequency power switches (S_1-S_8), CREE C2M0080120D SiC MOSFETs are used. For the BMS contactor, the TE EV200AAANA SPST contactor is used. The integrated transformers are constructed using Nanocrystalline C core and Litz wire. The primary design is targeted to achieve maximum leakage inductance to eliminate the need for extra inductors required for DAB power flow. The proposed control algorithm is implemented in Spartan 6 XC6SLX9 FPGA.

Table 3.1. Specification for the integrated converter prototype

Converter	Boost Converter	DAB Converter
Battery Voltage ($\boldsymbol{V_B}$) (V)	200	200
HV Bus Voltage ($\boldsymbol{V_{HV}}$) (V)	400 – 500	400 – 500
Power (W)	5000	660

The integrated converter power flow control and mode transition are performed by the FPGA by controlling the SiC switches and the BMS contactor. A 60 µF film capacitor is used for the HV bus capacitor. A DC power supply is used as the battery and an electronic load is used to emulate the traction inverter. The scaled-down integrated DC-DC converter prototype is shown in Figure 3.12. The integrated DC-DC converter is tested in interleaved boost mode for 5 kW traction operation.

The integrated converter is operated in interleaved boost mode up to 5 kW at 450 V output voltage. The gate signal, switch node voltage, and the secondary winding current waveforms for the interleaved boost mode are shown in Figure 3.13. The integrated converter is operated in DAB mode up to 600 W at 450 V output voltage. The gate signal, primary switch node voltage, the primary winding current, and the secondary winding current waveforms for the DAB mode are shown in Figure 3.14. Unlike a conventional DAB, the primary and secondary current waveshapes are different during the power transfer interval. Part of the primary current is circulating back through the magnetizing inductance.

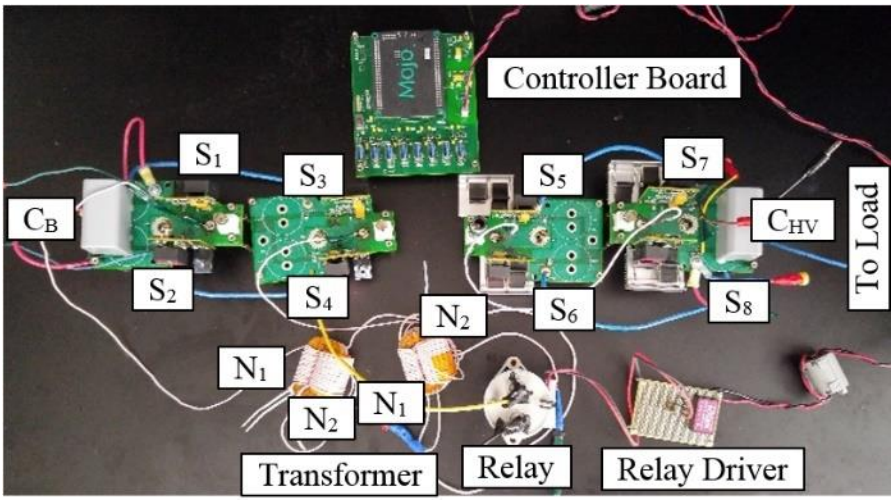

Figure 3.12. The experimental prototype for the 5 kW integrated converter.

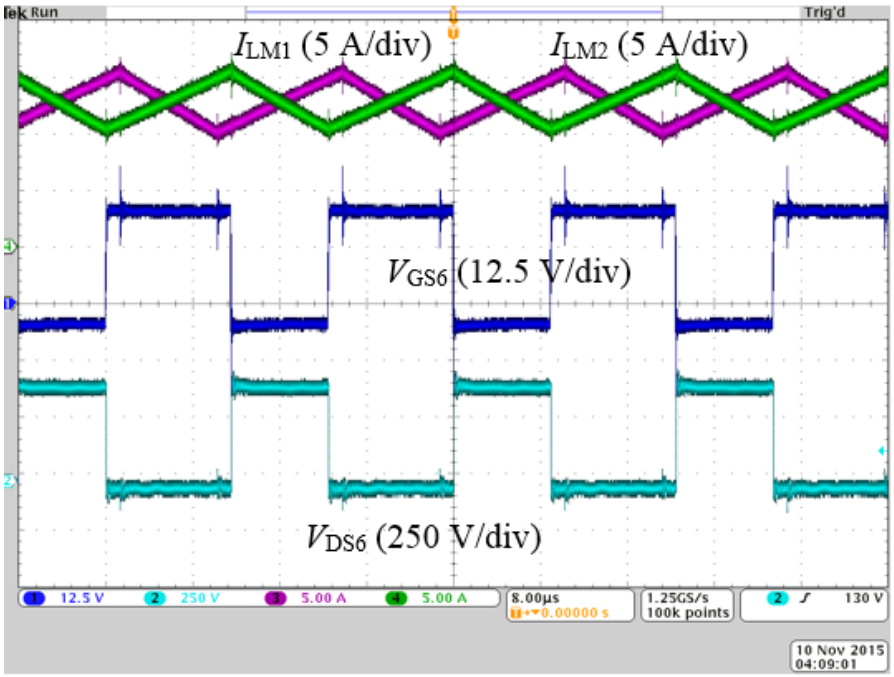

Figure 3.13. Waveforms of the integrated converter at interleaved boost mode at 5 kW.

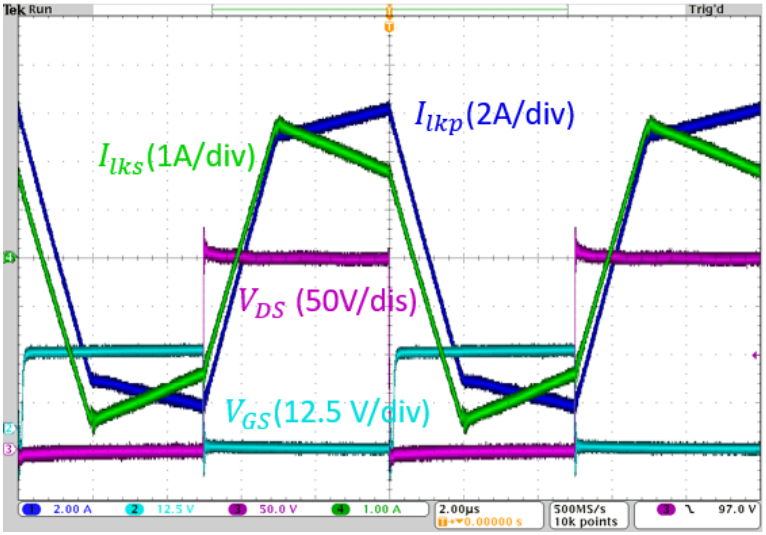

Figure 3.14. Waveforms in DAB powertrain mode at 600 W.

3.6 Summary

In the integrated converter topology, the existing BMS contactors are used for the integrated converter reconfiguration. High power boost switches are used for DAB secondary H-bridge. The same magnetic core is also used for the construction of the boost converter and the high-frequency isolation transformer. The integrated converter can utilize the same heatsink for the traction and charging stage power switches and magnetics as well. In this way, the integrated converter can perform both traction and charger operation with shared components while reducing the converter weight and price. The integrated converter operation in interleaved boost mode and DAB mode is verified in this chapter. Unlike the conventional DAB, the primary and secondary current waveform is different in the hybrid transformer during the power flow interval. In the next chapter, the integrated converter model will be updated considering the effect of magnetizing inductance.

4 Integrated Converter Modeling

The integrated converter can be reconfigured and operated in both boost mode and DAB mode. The integrated converter loss mechanisms are investigated in this chapter for different operating modes. Since the hybrid transformer is designed to handle peak boost current, the magnetizing inductance is low compared with the conventional DAB converter. A model is developed for the DAB mode primary winding current waveform considering the effect of magnetizing inductance. The main motivation for loss modeling is to improve the integrated converter design.

4.1 Boost Loss Modeling

During the traction operation, the boost converter steps up the battery voltage for efficient motor-inverter operation. The traction boost converter power rating is the same as the traction inverter power rating. The boost converter switching operation is shown in Figure 4.1.

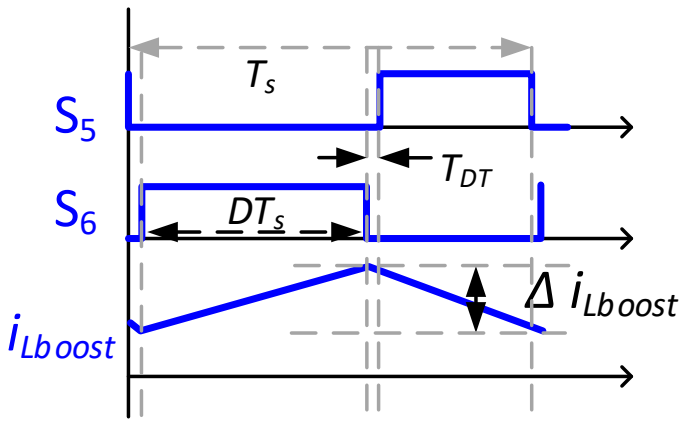

Figure 4.1. Traction boost converter waveform for different switching intervals.

The main loss mechanisms of the traction boost converter are conduction loss, switching loss, winding loss, core loss, and gap loss.

4.1.1 Conduction Loss

The conduction loss is contributed by the device on-state resistance during the device turn-on and the diode during the switching transition. The current through the main switch (S_5) is

$$I_{rms,main} = I_{L_{boost}} \sqrt{D\left(1 + \frac{1}{3}\left(\frac{\Delta I_{L_{boost}}}{I_{L_{boost}}}\right)^2\right)} \tag{4-1}$$

The current through the synchronous (S_6) switch is

$$I_{rms,sync} = I_{L_{boost}} \sqrt{(1-D)\left(1 + \frac{1}{3}\left(\frac{\Delta I_{L_{boost}}}{I_{L_{boost}}}\right)^2\right)} \tag{4-2}$$

The device on-state resistance, $R_{ds,on}$, is obtained from the manufacturer datasheet. The device conduction loss per phase is

$$P_{cond,\ sx} = R_{ds,on} I^2_{rms,main} + R_{ds,on} I^2_{rms,sync} \tag{4-3}$$

The diode conducts during the dead band interval once the equivalent device capacitance is discharged. The diode conduction loss can be reduced by optimizing the dead-band time. The diode conduction loss is

$$P_{cond,\ d} = \left(I_{LM} V_{f@I_{L_{boost}}} T_d\right) f_s \tag{4-4}$$

where, $V_{f@I_{LM}}$, T_d, and f_s represent the diode forward voltage drop at the inductor current, diode conduction interval, and boost converter switching frequency.

4.1.2 Switching Loss

During the switching transition between the primary and synchronous switches, the overlap between the device drain current and drain to source voltage results in overlap switching loss. The capacitive energy loss occurs when the energy stored in the device capacitance is dissipated in the device channel during the primary switch turn-on process. The overlap loss and capacitive loss are the major contributors to the boost converter loss mechanism. The switching loss can be reduced by adopting soft switching techniques.

To measure switching energy associated with the power switches, a double pulse test (DPT) setup is developed as shown in Figure 4.2. The schematic of the DPT platform is shown in Figure 4.3. The turn-on and turn-off switching energy are evaluated for different load current and voltage conditions. The double pulse test results for different bus voltage are shown in Figure 4.4.

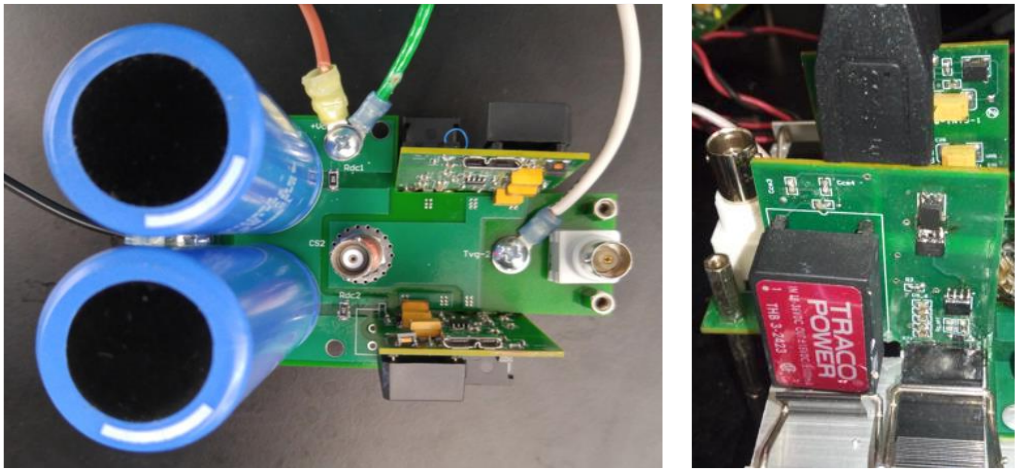

(a) (b)

Figure 4.2. Switching energy evaluation setup (a) double pulse test board and (b) gate driver board.

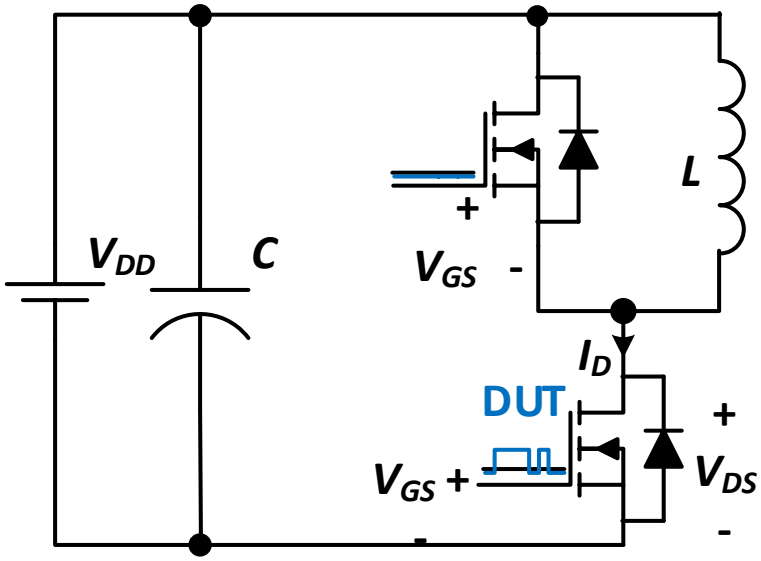

Figure 4.3. Schematic for the double pulse test for switching loss evaluation.

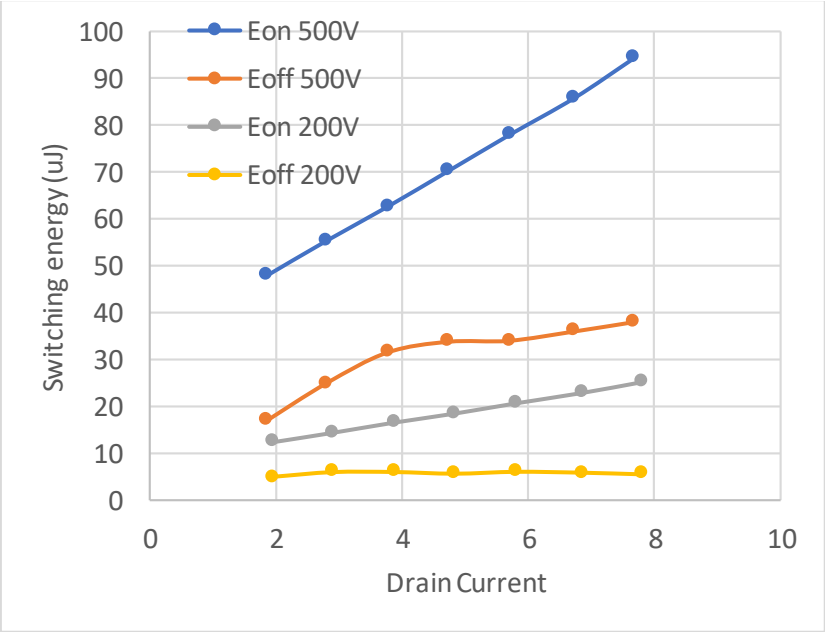

Figure 4.4. Turn-on and turn-off loss at different bus voltage.

The double pulse test results are used for the switching loss estimation. Based on the power level and the inductor current, the boost converter can operate in hard switching conditions, partial ZVS, and full ZVS condition.

When the minimum inductor current is positive, the converter operates in hard switching conditions. The main switch operates at hard switching turn-on and turn-off switching loss. The auxiliary switch always operates under soft switching conditions for positive power flow. The switching loss during the hard-switching condition is

$$P_{SW} = f_s\left(E_{on@V_{HV}@I_{Lboostmin}} + E_{off@V_{HV}@I_{Lboostmax}}\right) \tag{4-5}$$

where $E_{on@V_{HV}@I_{Lboostmin}}$ and $E_{off@V_{HV}@I_{Lboostmax}}$ represent the turn-on switching energy during the minimum inductor current and turn-off switching energy during the maximum inductor current through the main switch at the operating inverter bus voltage.

The synchronous boost converter full ZVS condition depends on minimum inductor current and minimum dead band to discharger the devices' capacitive energy completely. The switching loss during soft switching condition is

$$P_{SW} = f_s\left(E_{off@V_{HV}@I_{Lboostmax}} + E_{off@V_{HV}@|I_{Lboostmin}|}\right) \tag{4-6}$$

When the dead band and/or the peak inductor current is not enough to discharge the blocking device capacitive energy completely, partial ZVS condition is observed. In this condition, the device is turned on at a lower voltage than the inverter bus voltage and the capacitive energy is partially recovered.

4.1.3 Core Loss

The inductor ripple current causes flux ripple in the inductor with a DC offset. The inductor core loss is calculated using the improved Generalized Steinmetz Equation (iGSE) [116]. Since the boost waveforms are non-sinusoidal, the iGSE method has better accuracy than the Steinmetz Equation. The core loss is

$$\overline{P_{core}(t)} = \frac{k}{2^{\beta+1}\pi^{\alpha-1}\left(0.2761 + \frac{1.7061}{\alpha+1.354}\right)} (\Delta B)^{\beta-\alpha} \overline{\left|\frac{dB}{dt}\right|^{\alpha}} \tag{4-7}$$

where ΔB represents peak flux density obtained from the inductor ripple current. The Steinmetz parameters k, α, and β for the cut-type Nanocrystalline C core are 8, 1.621, and 1.982 respectively [102].

4.1.4 Winding Loss

The boost current consists of DC and AC components. The DC winding loss depends on the length and copper cross-sectional area of the conductor. The boost converter DC winding resistance is

$$R_{dc} = \rho_{Cu}\frac{l_w}{A_w} = \rho_{Cu}\frac{N_s \times l_T}{A_w} \tag{4-8}$$

where ρ, N_s, l_T, A_w are the copper resistivity, the number of secondary turns, mean length per turn, and the cross-sectional area of the boost winding. For Litz wire, the cross-sectional copper area of the Litz wire is

$$A_w = n_{str}\left(\frac{1}{4}\pi d_{str}^2\right) \tag{4-9}$$

where, $n_{str}$and d_{str} represent the number of strands in a Litz wire and diameter of the individual strands of Litz wire.

AC resistance can be estimated using the modified Dowell's equation for Litz wire [117, 118]. The effective number of layers of a multiple strands Litz wire is

$$N_{ll} = N_s\sqrt{k} \tag{4-10}$$

where k is the number of strands in the Litz wire. From [117], the AC to DC winding resistance ratio for a Litz wire is

$$F_r = \frac{R_{Wac}}{R_{Wdc}} = A_{str}\left[\frac{\sinh(2A_{str}) + \sin(2A_{str})}{\cosh(2A_{str}) - \cos(2A_{str})} + \frac{2(N_{ll}^2 - 1)}{3}\frac{\sinh(2A_{str}) - \sin(2A_{str})}{\cosh(2A_{str}) + \cos(2A_{str})}\right] \tag{4-11}$$

where the A_{str} is defined as

$$A_{str} = \left(\frac{pi}{4}\right)^{0.75}\frac{d_{str}}{\delta_{str}}\sqrt{\eta} \tag{4-12}$$

where d_{str}, δ_{str}, and η are the strand diameter, skin depth of the strand, and the porosity factor respectively.

The winding loss in the boost converter is then

$$P_{wind} = R_{dc} I_{L_{boost}}^2 + \sum R_{ac,n} \left[\frac{\Delta I_{L_{boost}}}{4} \left(- \frac{2(-1)^n}{n^2 D(1-D)\pi^2} \sin(n\pi(1-D)) \right) \right]^2 \quad (4\text{-}13)$$

where n and $R_{ac,n}$ are the harmonic number and corresponding AC resistance of the harmonic.

4.1.5 Gap Loss

To prevent saturation an air-gap is used in the nanocrystalline core. Since Nanocrystalline material is a conductive material, fringing flux near the airgap cause eddy current flow on the surface of the nanocrystalline lamination [101]. This results in an additional loss in the core. The gap loss is modeled by [99] as

$$P_g = k_g l_g D^{1.65} f_s^{1.72} B_m^2 \quad (4\text{-}14)$$

where k_g, l_g, and D are the core mass coefficient, air-gap of the core, and the depth of the core respectively. The empirical model does not consider the winding orientation. For accurate gap loss evaluation during high frequency transformer operation, FEA based model considering the edge laminations and actual winding orientation is considered.

4.2 DAB Model

A typical DAB transformer has very high magnetizing inductance compared to the leakage inductance [119-121]. As a result, the magnetizing current can be neglected. However, for integrated and hybrid converters, where the same core is used for both DC excitation and AC excitation, an air gap is used to prevent core saturation with peak current. In such applications, the effect of magnetizing inductance needs to be considered for DAB converter modeling.

To investigate the effect of the magnetizing inductance of the high-frequency DAB transformer, the T model is considered as shown in Figure 4.5. The leakage inductance is difficult to estimate accurately since it depends on the winding arrangement. Based on the winding configuration, the coupling coefficient between the primary and secondary changes as well. As shown in Figure 4.6, for overlapping or interleaved winding, the coupling coefficient is higher, and the leakage inductance is lower. The leakage inductance of the DAB transformer can be adjusted using different winding configurations. In general, lower leakage inductance reduces the converter loss by limiting the peak currents of the primary and secondary winding.

The actual transformer parameters are obtained using an impedance analyzer. The primary self-inductance of the integrated transformer

$$L_{P,\,S_{oc}} = L_{lkp} + \frac{L_M}{n^2} \tag{4-15}$$

is measured from the primary side by opening the secondary side of the transformer. The secondary self-inductance

$$L_{S,\,P_{oc}} = L_{lks} + L_M \tag{4-16}$$

is measured from the secondary side by opening the primary side of the transformer.

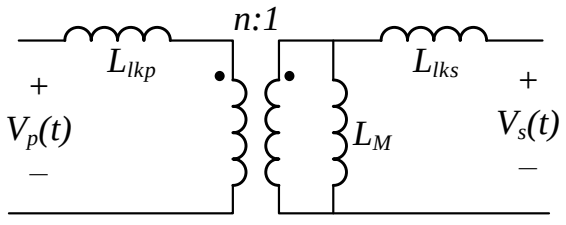

Figure 4.5. Integrated transformer equivalent T model.

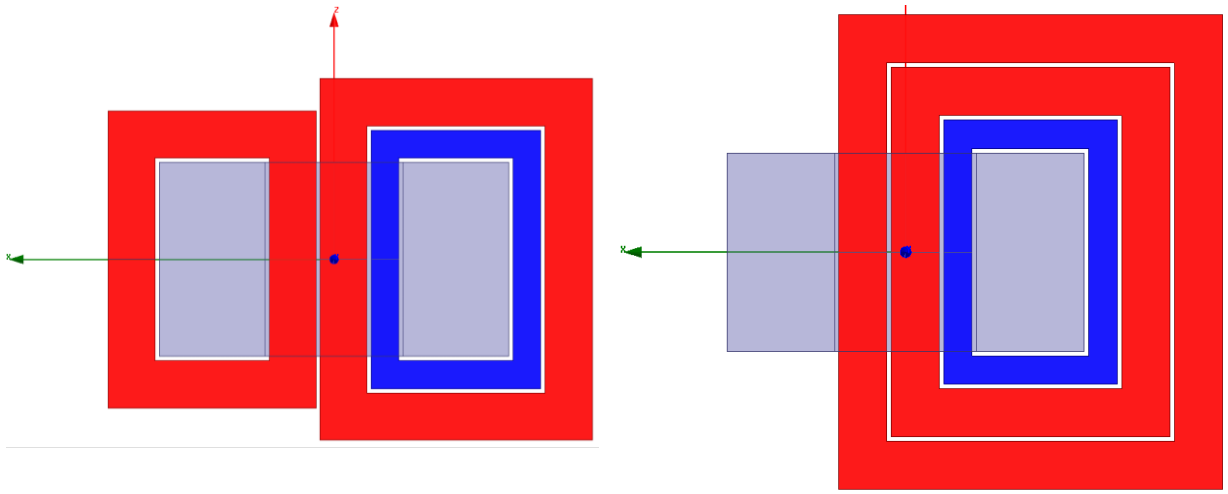

(a) (b)

Figure 4.6. Different winding arrangement for the integrated transformer (a) 89% coupling and (b) 96% coupling.

To evaluate the primary and secondary leakage inductances, the secondary side of the transformer is shorted and total leakage inductance is measured from the primary. Then, the primary is shorted, and the total leakage inductance is measured from the secondary side. The resulting measured inductances are

$$L_{P,S_{SC}} = \frac{L_{lks}}{n} + \frac{L_M L_{lkp}}{L_M + nL_{lkp}} \tag{4-17}$$

$$L_{S,P_{SC}} = nL_{lkp} + \frac{L_{lks} L_M}{L_M + L_{lks}} \tag{4-18}$$

The four unknown parameters L_{lkp}, L_{lks}, L_M, and n can be evaluated. For accurate modeling, it is important to evaluate the parameters at the operating frequency since the current peaks and total power flow are dependent on the leakage parameters and effective turns ratio.

The switching waveforms of S_1-S_8, the primary and secondary voltage, the voltage across the transformer, and the leakage and magnetizing currents of the DAB converter are shown in Figure 4.7. The primary and secondary voltage across the transformer is

$$V_p(t) = \begin{cases} V_B, & 0 < t < \frac{T_{sw}}{2} - T_{dt} \\ -V_B, & \frac{T_{sw}}{2} < t < T_{sw} - T_{dt} \end{cases} \tag{4-19}$$

$$V_s(t) = \begin{cases} -V_{HV}, & 0 < t < T_{sh} - T_{dt} \\ V_{HV}, & T_{sh} < t < \frac{T_{sw}}{2} + T_{sh} - T_{dt} \\ -V_{HV}, & \frac{T_{sw}}{2} + T_{sh} < t < T_{sw} \end{cases} \tag{4-20}$$

where V_B, V_{HV}, T_{sw}, T_{sh} and T_{dt} are the battery voltage, HV bus voltage, switching period, phase shift, and dead time respectively. The T node voltage is

$$V_n(t) = \frac{n^2 L_{lkp} v_s(t) + L_{lks} n v_p(t)}{n^2 L_{lkp}\left(1 + \frac{L_{lks}}{L_m}\right) + L_{lks}} \tag{4-21}$$

where n, L_{lkp}, L_{lks}, and L_M are the effective turns ratio, primary leakage current, secondary leakage current, and magnetizing current respectively.

During the phase shift interval, the magnetizing current, i_M, remains almost constant. Both the primary leakage current, i_{lkp}, and the secondary leakage current, i_{lks}, have a positive slope during the phase shift interval. During the power delivery interval, a portion of the primary leakage

current is circulated back as magnetizing current. The slope of the primary leakage current during the power delivery interval depends on the output voltage. The secondary leakage current has a negative slope and the magnetizing current has a positive slope as shown in Figure 4.7. The peak magnetizing current is

$$I_{M_{peak}} = \frac{\left(\frac{T_{sw}}{2} - T_{sh}\right)\left(nV_B n^2 L_{lkp} + V_{HV} L_{lks}\right) + T_{sh}\left(nV_b L_{lks} - V_{HV} n^2 L_{lkp}\right)}{2L_m\left(n^2 L_{lkp}\left(1 + \frac{L_{lks}}{L_m}\right) + L_{lks}\right)} \tag{4-22}$$

where n is the turns ratio of the transformer. At lower phase shift, higher peak magnetizing current occurs. Due to the presence of the positive magnetizing current, the DAB converter will achieve ZVS at lower power. The dead time is ignored in the derivation for simplicity. The leakage current through the primary winding is

$$I_{lkp2} = \frac{nV_{HV}\left(\frac{T_s}{2} - 2T_{sh}\right)}{2\left(n^2 L_{lkp}\left(1 + \frac{L_{lks}}{L_m}\right) + L_{lks}\right)} - \frac{n^2 V_{bat} Ts\left(1 + \frac{n^2 L_{lks}}{L_M}\right)}{4\left(n^2 L_{lkp}\left(1 + \frac{L_{lks}}{L_m}\right) + L_{lks}\right)} \tag{4-23}$$

The leakage current through the secondary winding is

$$I_{lks1} = \frac{\left(\frac{T_{sw}}{2} - T_{sh}\right)\left(n^2 L_{lkp}(nV_B - V_{HV}) + L_{lks} T_{sh}(V_b n + V_{HV})\right)}{2\left(n^2 L_{lkp}\left(1 + \frac{L_{lks}}{L_m}\right) + L_{lks}\right)} + \frac{\frac{L_{lks}}{L_m} V_{HV} L_p n^2 \left(\frac{T_{sw}}{2} - 2T_{sh}\right)}{2\left(n^2 L_{lkp}\left(1 + \frac{L_{lks}}{L_m}\right) + L_{lks}\right)} \tag{4-24}$$

The current peaks derived for the primary winding, secondary winding, and magnetizing inductance is used for the integrated converter loss evaluation in the DAB mode.

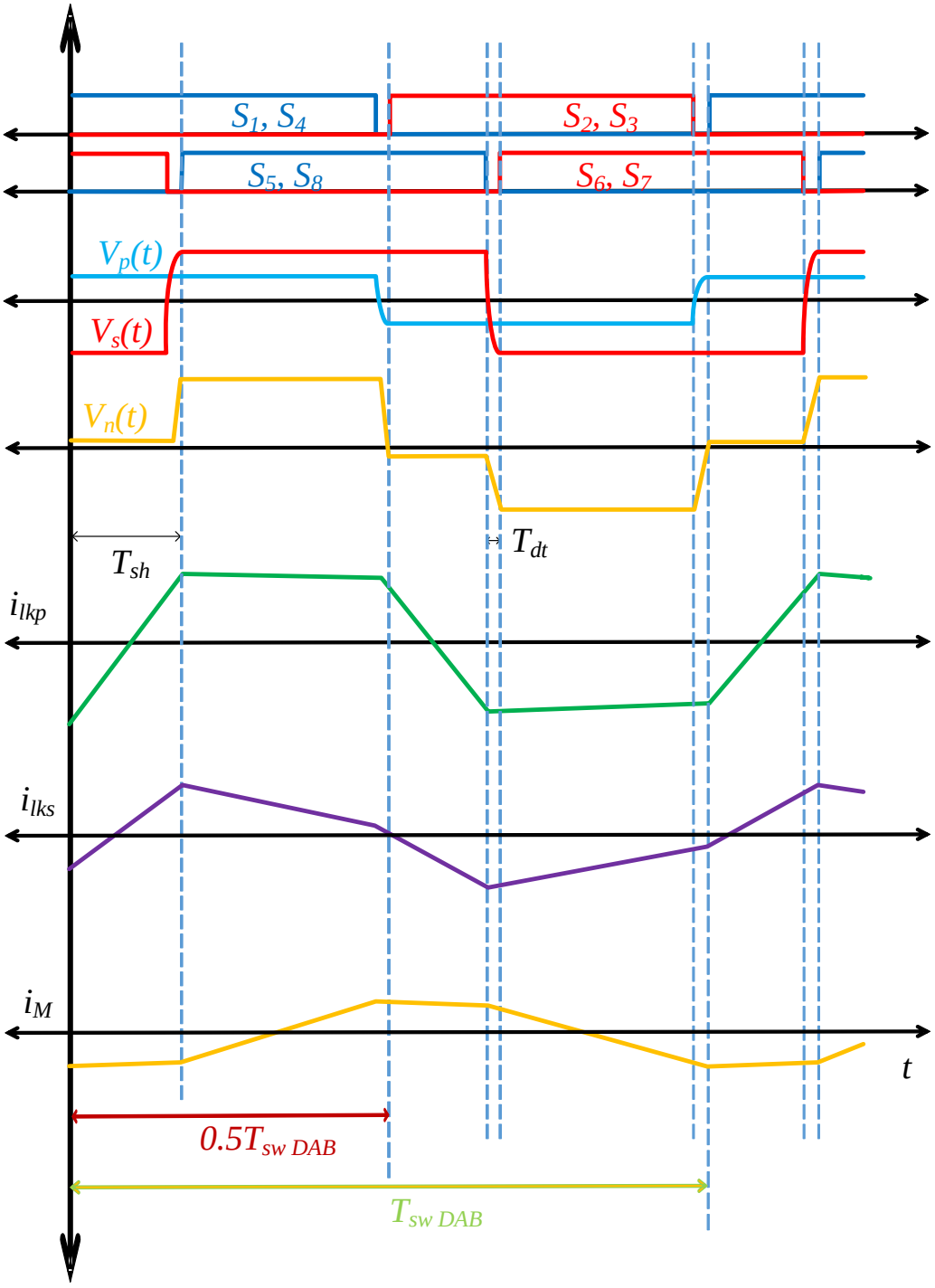

Figure 4.7. DAB converter waveforms for different switching intervals.

4.3 DAB Loss Modeling

The basic loss mechanisms of the DAB converter are conduction loss, switching loss, winding loss, core loss, and gap loss.

4.3.1 Conduction Loss

The conduction loss includes the primary and secondary SiC devices' conduction loss and the diode conduction loss during the dead-time interval. The primary side RMS current is

$$I_{lkp_{rms}} = \sqrt{\begin{matrix}\frac{1}{3}\left(I_{lkp0}^2 + I_{lkp0}I_{lkp1} + I_{lkp1}^2\right)\frac{T_{sh}}{T_s} \\ +\frac{1}{3}\left(I_{lkp1}^2 + I_{lkp1}I_{lkp2} + I_{lkp2}^2\right)\frac{T_s - T_{sh}}{T_s}\end{matrix}} \tag{4-25}$$

Since two SiC devices are turned-on during any conduction interval in the primary and secondary bridge, the primary and secondary device conduction loss is

$$P_{cond,M} = I_{lkp_{rms}}^2\left(2R_{p\,ds_{on}}\right) + I_{lks_{rms}}^2\left(2R_{p\,ds_{on}}\right) \tag{4-26}$$

where $R_{p\,ds_{on}}$ and $R_{p\,ds_{on}}$ are the primary and secondary device on-state resistance respectively.

The diode conduction loss is

$$P_{cond,d} = 4\left(I_{lkp2}V_{f@I_{lkp2}}T_{dp} + I_{lks1}V_{f@I_{lks1}}T_{ds}\right)f_s \tag{4-27}$$

where, $V_{f@I_{lkp2}}$, $V_{f@I_{lks1}}$, T_{dp}, T_{ds}, and f_s are the diode forward voltage drop at the primary and secondary switch current during diode conduction, the diode conduction time, and switching frequency respectively.

4.3.2 Switching Loss

In a traditional DAB, the ZVS capability is lost during the light load operation. However, in the integrated converter, the presence of the magnetizing current at a very low phase shift extends the ZVS range. Considering the zero phase shift condition, the peak magnetizing current is

$$I_{M_{peak}} = \frac{\left(\frac{T_{sw}}{2}\right)\left(nV_B n^2 L_{lkp} + V_{HV} L_{lks}\right)}{2L_m\left(n^2 L_{lkp}\left(1 + \frac{L_{lks}}{L_m}\right) + L_{lks}\right)} \tag{4-28}$$

In a traditional DAB, the magnetizing inductance L_m is big enough to reduce the peak magnetizing current to near zero. For the proposed integrated converter, the magnetizing inductance is smaller than the self-inductance of the secondary coil. As a result, the node voltages will cause sufficient current flow to discharge the device capacitance during the light load switching transition for the primary side devices.

Since the DAB converter is operated in the soft switching operating region, only turn-off switching energy is considered. The total switching energy is evaluated as

$$P_{sw} = \left(4\left(E_{off@V_B@I_{lkp1}} - E_{coss@V_B}\right) + 4\left(E_{off@V_{HV}@I_{lks2}} - E_{coss@V_{HV}}\right)\right) f_s \tag{4-29}$$

where $E_{off@V_B@I_{lkp1}}$, $E_{off@V_{HV}@I_{lks2}}$, $E_{coss@V_B}$, and $E_{coss@V_{HV}}$ are the turn-off switching energy at a given primary and secondary peak currents and the device capacitive energy respectively.

4.3.3 Winding Loss

The DAB primary and secondary winding conduct alternating current. Usually, the primary side and secondary side of the DAB have different magnetic wire or Litz wire construction due to

the current conduction requirement. The primary side and secondary side winding loss of the DAB converter is

$$P_{wind} = \sum_{m=1}^{2n-1} R_{acp,m}\left(\frac{i_{lkp,m}}{2}\right)^2 + \sum_{m=1}^{2n-1} R_{acs,m}\left(\frac{i_{lks,m}}{2}\right)^2 \quad (4\text{-}30)$$

where $R_{acp,n}$, $R_{acs,n}$, and n are the primary winding AC resistance, secondary winding AC resistance, and harmonic number considered for the winding loss, respectively.

4.3.4 Core Loss and Gap Loss

The core loss and gap loss are evaluated using the same method as the boost converter. Since the DAB magnetizing inductor current, i_M, is non-sinusoidal, the core loss is also calculated using the iGSE method [116]. A gap loss model is developed in FEMM 2D to evaluate the gap loss for DAB. A Nanocrystalline U core is modeled in FEMM 2D with actual primary and secondary winding arrangement. Since on-edge lamination is not supported in FEMM AC analysis, in-plane lamination is considered to model the 18 µm uniform lamination in the core. This prevents excessive eddy current flow in the modeled core of the high-frequency transformer. To evaluate the surface eddy current related loss, three 18µm edge lamination model is constructed at the inner and outer edge of the core as shown in Figure 4.8. The fringe flux is very high near the air gap and diminishes further from the air gap. The lamination model provides loss due to the fringe flux near the air gap at different power and switching frequency.

The number of inner and outer layers considered for the gap loss model is varied from two to five as shown in Figure 4.9. Three lamination layers provide good enough estimation for the gap loss. Additional layers do not increase the gap loss significantly since the layers closer to bulk material are shielded by the outer layers. Larger number of layers adds computational time as well.

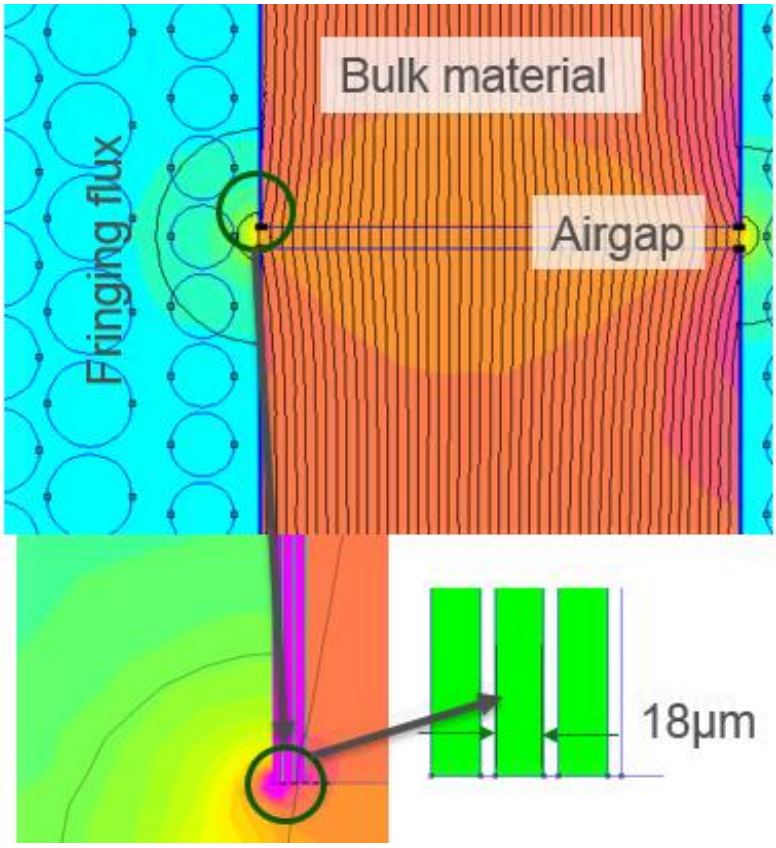

Figure 4.8. Hybrid transformer lamination model.

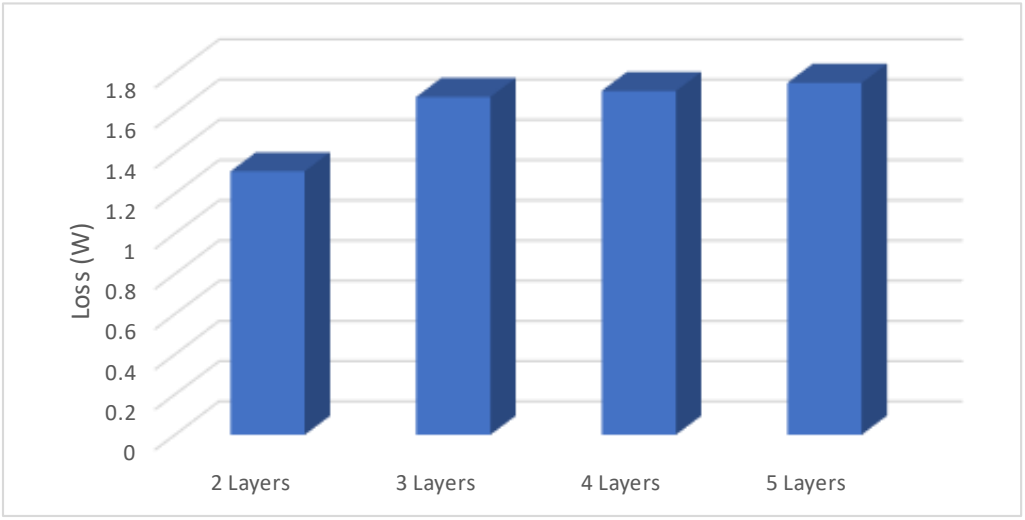

Figure 4.9. The number of layers considered for gap loss modeling.

The model excitation is provided from the fundamental component of primary and secondary winding current at a different power level and switching frequency. The current waveforms can be obtained from simulation or experimental results. After obtaining the FEA results, the loss in the laminar strips are integrated and total loss is evaluated. The modeled fringe flux and the current flow in the adjacent winding induced gap loss at a different frequency and different power for different power level is shown in Figure 4.10. Compared to the gap loss model presented in [99], the FEMM 2D model predicts lower gap loss at lower power. The FEMM 2D gap loss model is used to validate the experimental results in the DAB mode of operation.

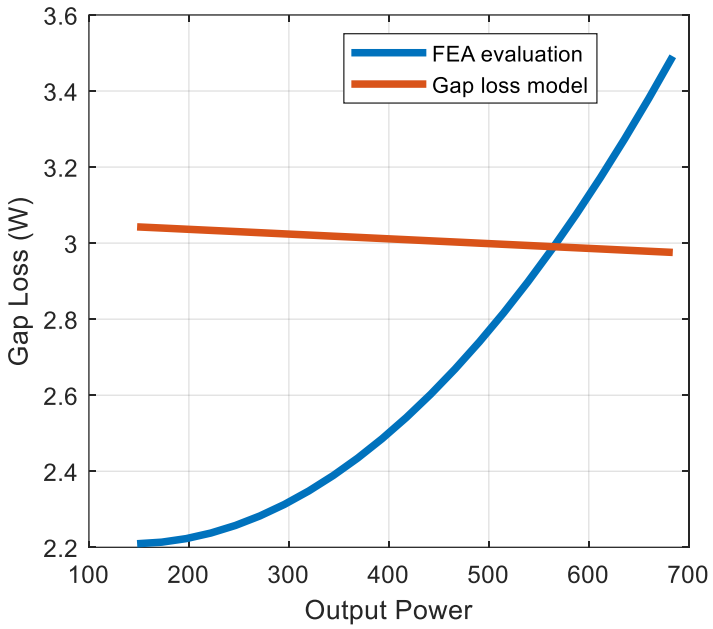

Figure 4.10. Comparison between the gap loss model in [99] and the FEA model for DAB.

4.4 Experimental Results

The low power scaled down proof-of-concept integrated converter prototype is used for the performance evaluation of the integrated converter. Two identical series-connected high-frequency Hitachi FINEMET F3CC0020 Nanocrystalline cores are used for the hybrid transformer. The integrated converter is operated at 50 kHz in both boost and DAB mode. The integrated converter operation in boost mode at 200 V battery voltage and 450 V inverter bus voltage is shown in Figure 4.11. Due to the hard-switching condition, the switching loss is the dominant loss mechanism at high power. At light load, the converter switching loss is reduced due to the partial-ZVS condition. The loss breakdown in DAB mode at 200 V battery voltage and 450 V inverter bus voltage is shown in Figure 4.12. The integrated converter operating in DAB mode can provide higher efficiency at light load as shown in Figure 4.13. During the integrated converter operation at 400 W, the DAB can improve the boost efficiency.

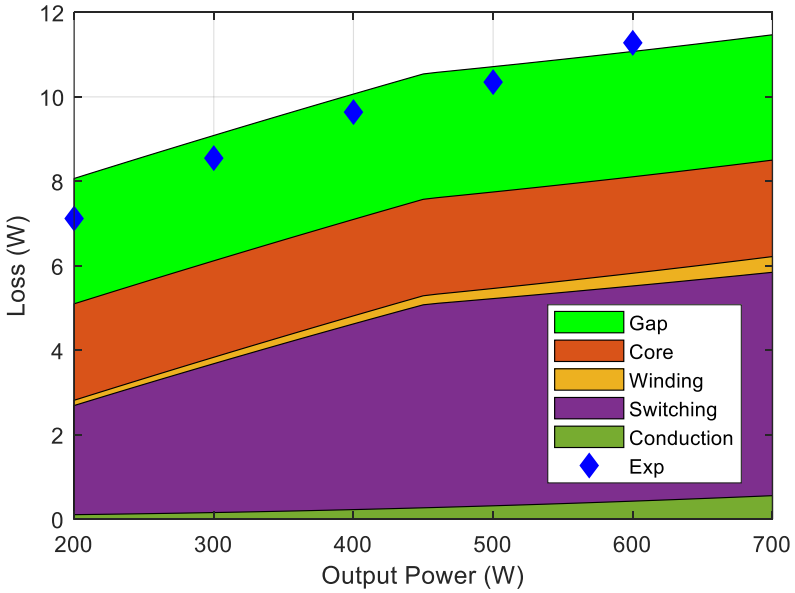

Figure 4.11. Integrated converter loss breakdown in boost mode.

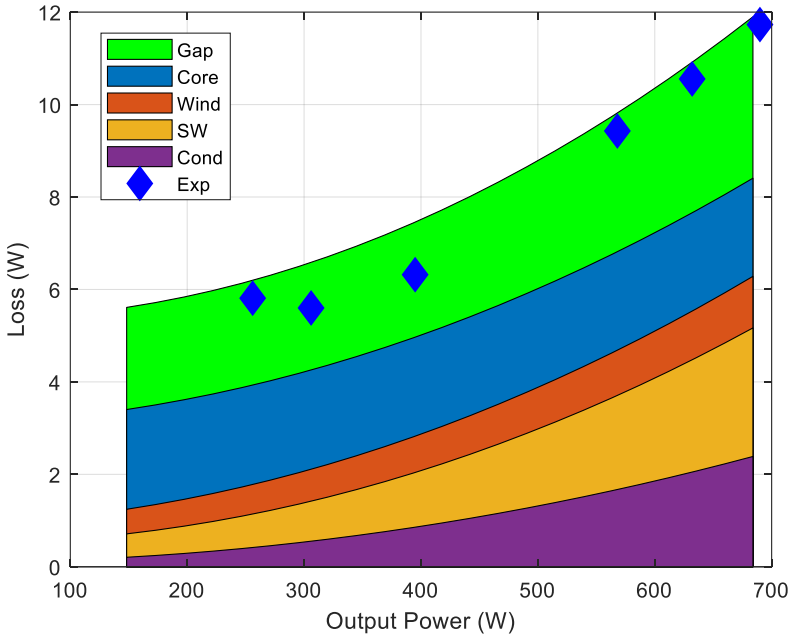

Figure 4.12. Integrated converter loss breakdown in DAB mode.

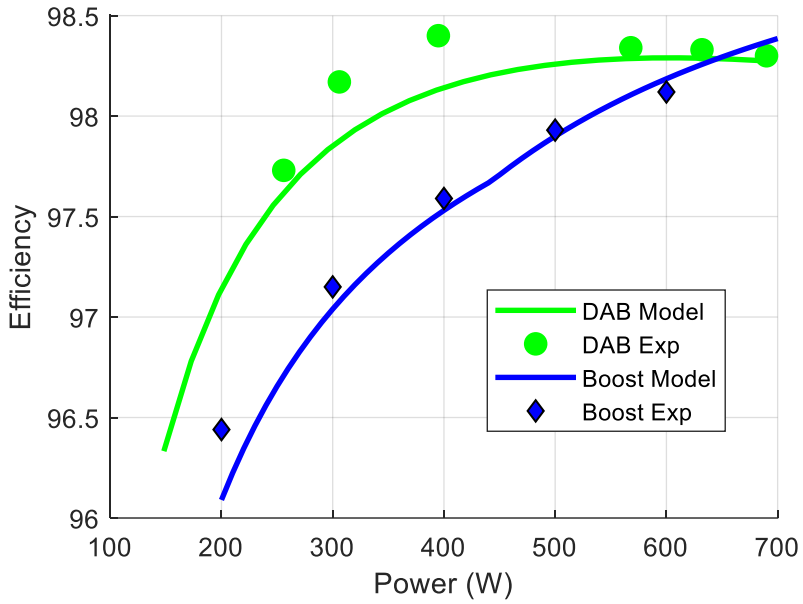

Figure 4.13. Integrated converter efficiency in different operating modes.

4.5 Summary

Different loss mechanisms in the integrated converter are explored in this chapter. A method to estimate the gap loss mechanism in FEMM 2D is also presented which can predict the gap or fringe induced loss more accurately. The integrated converter loss model in both boost mode and DAB mode is validated. At the light load traction operation, the DAB mode provides higher efficiency than interleaved boost mode. As a result, DAB mode can improve the light load traction efficiency. However, the online transition from boost mode to DAB mode during light load traction operation is challenging. The power flows through the BMS contactors during boost mode while the power flows through the isolation transformer during the DAB mode. Moreover, BMS contactors require several milliseconds to connect and disconnect.

5 Online Operating Mode Transition

To maximize integrated converter efficiency during traction operation, the online transition between the boost mode and DAB mode is required. In this chapter, a control strategy is developed for the integrated converter for a seamless transition between the operating modes. The impact of slow BMS contactor behavior is demonstrated. A modulation method is proposed to eliminate power flow interruption and reduce the voltage and current ripple during the online transition.

5.1 Motivation

During traction operation, EV power requirement varies at different points of the city and highway driving condition. To improve traction efficiency during the light load traction operation, the integrated converter can be reconfigured from boost mode to DAB mode. During high power operation, the integrated converted can be reconfigured form DAB mode to boost mode. Operating mode transitions will occur at a frequency determined by vehicle driving dynamics, which are significantly slower than switching dynamics.

To minimize loss, arcing possibility, and maximize the lifetime of the mechanical contactors, the transitions must achieve zero current when the contactor is opened and zero voltage when the contactor is closed. Additionally, to prevent interruption of power flow to the electric drive, transitions must be designed to allow the converter to immediately enter steady-state operation in the new mode without requiring settling time or a lengthy switching transient.

Contactors S_{11} and S_{12} are integrated into many EV battery packs. Table 5.1 details switching dynamics of an example BMS contactor. Though mechanical contactors allow for much greater voltage blocking and lower conduction loss than semiconductor switches, they exhibit lengthy switching transients. Before adopting the transition control strategy developed in this

work, one approach to switching between operating modes is to shut down the converter, switch the contactor, then restart in the new operating mode. To allow enough time to ensure the contactor has closed, this shutdown period should last as long as 22 ms, during which no power is delivered from battery to the motor drive.

The transition from boost mode to DAB mode is shown in Figure 5.1. To comply with the contactor specification given in Table 5.1, 12 ms delay is inserted to allow the contactor switching action to complete. As a result, the power flow is interrupted during the delay interval. The inverter bus voltage also drops about 50 V as shown in Figure 5.1.

Table 5.1. BMS contactor parameters (TE EV200AAANA [122])

Parameters	Time (ms)
Contactor closing time	15
Bouncing time after closing (max)	7
Contactor releasing time	12

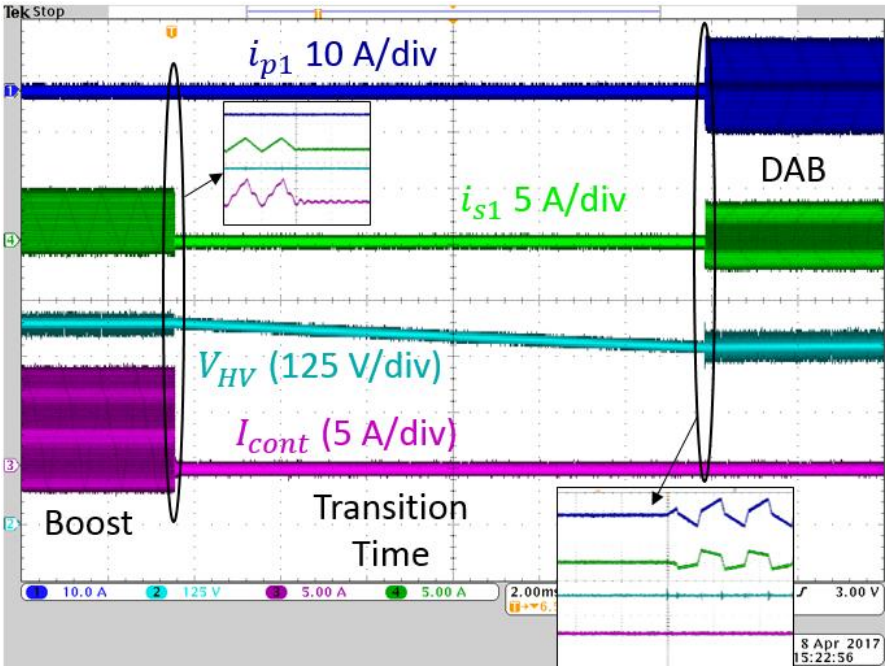

Figure 5.1. Long hold up time for the BMS contactor turn-off.

The transition from DAB mode to Boost mode is shown in Figure 5.2. A 21 ms delay time is added which accounts for both for contactor closing time and contactor bouncing time. The power flow is significantly interrupted during the delay interval and the interval bus voltage drops more than 90 V. During the boost mode start-up, the phase current overshoot is over 4 times the phase current. The soft startup is required as well to suppress the Boost startup generated in Figure 5.2.

Hybrid mechanical and solid-state switches can be used to reduce switching time at the expense of system price and efficiency. Alternately, additional HV bus capacitance can be used to minimize motor drive input voltage ripple during this transient. This approach is nonideal, as capacitor size and price are unnecessarily increased beyond the necessary values determined by the inverter modulation and power requirement only [123, 124]. Instead, a control scheme is developed which allows continuous power delivery during the contactor switching time.

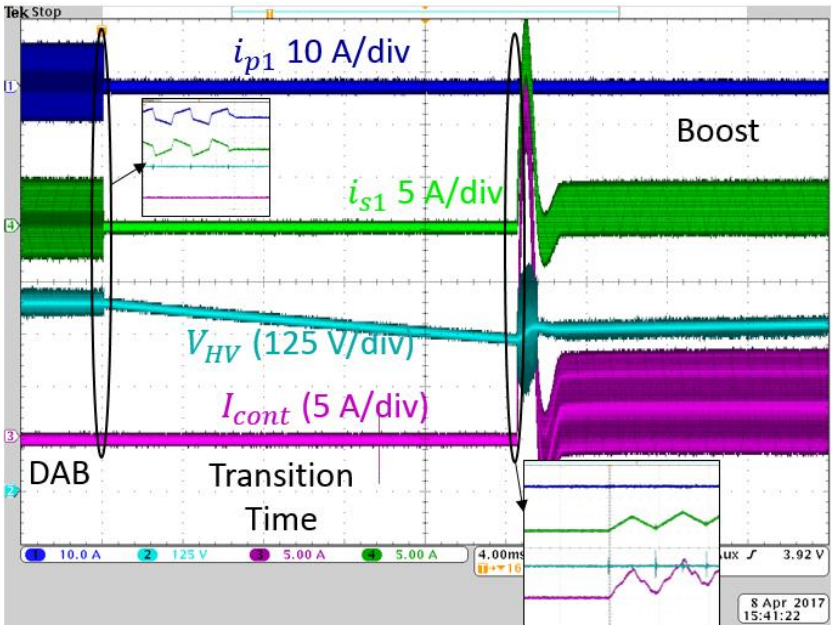

Figure 5.2. Long hold up time for the BMS contactor turn-on.

5.2 Proposed Control

The requirements for the transition control scheme are

1. The converter power flow shifts from boost to DAB or DAB to boost with minimal transient dynamics
2. The converter maintains continuous power delivery during the contactor switching time independent of the instantaneous state of the contactor
3. The contactor current is reduced to zero before opening
4. The contactor voltage is reduced to zero before closing

In the previous chapters of this topology, only the phase-shifted DAB and boost modulation were considered. Boost modulation cannot operate with the contactor open, and phase-shifted

(PS) DAB modulation will result in transformer saturation for most operating points when the contactor is closed; thus neither operating mode is capable of delivering continuous power during the contactor switching and bouncing transition.

Instead, an intermediate operating mode is developed using trapezoidal (Trap.) modulation of the DAB [125-127]. In this mode, by adjusting the duty cycle of the secondary phase legs of the converter (S_5-S_8), power flow through the isolation transformer can be regulated while simultaneously achieving zero voltage and zero current in the contactor. This trapezoidal operating mode is thus unaffected by the switching state of the contactor and can be used to ride through the switching transition without interruption of power delivery. A diagram of mode transitions is given in Figure 5.3, where the trapezoidal modulation is used only during the transition between PS DAB mode and boost mode.

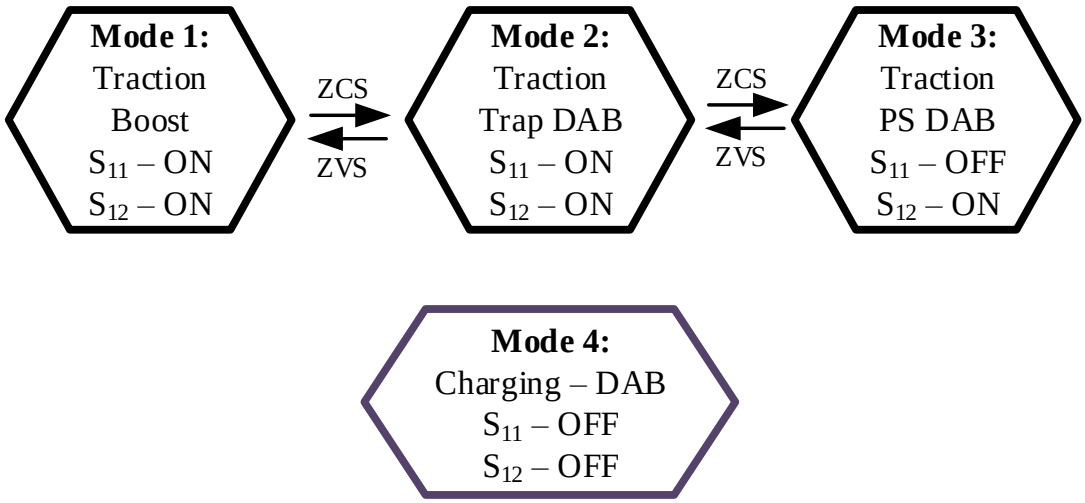

Figure 5.3. Different operation modes of the integrated converter based on BMS contactors.

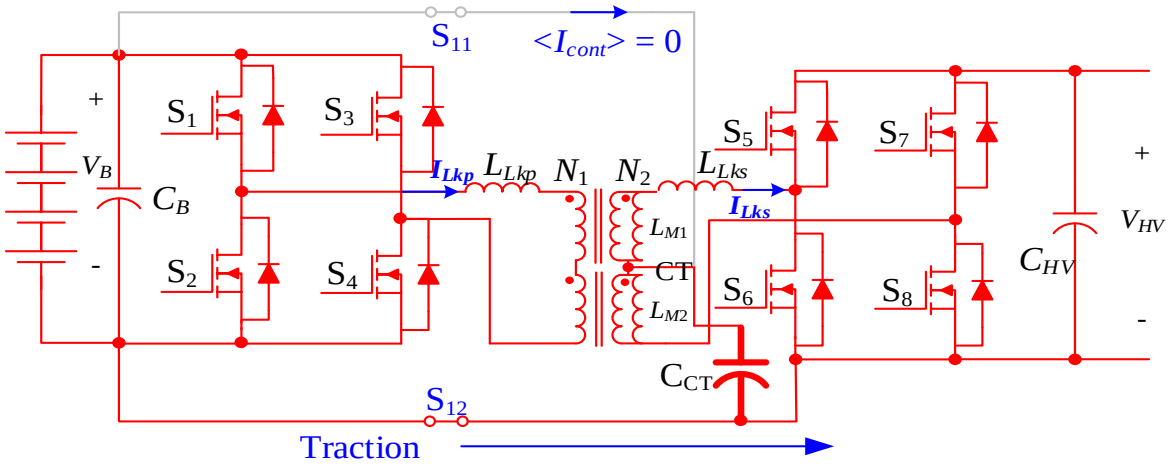

Figure 5.4. DAB Trapezoidal modulation operation for both traction operation (Mode 2).

The Trap DAB configuration is shown in Figure 5.4. In trapezoidal DAB modulation, the average voltage on the center-tap (CT) point of the transformer is regulated to the battery voltage by setting the duty cycle of the secondary side switches (S_1 - S_8) to

$$D_{DAB} = \frac{V_B}{V_{HV}} \tag{5-1}$$

The phase shift between primary and secondary bridges is used to regulate power flow through the transformer. An extra capacitor is placed between the CT node and ground to reduce the CT voltage ripple to its average value, maintaining an instantaneous zero voltage on the contactor S_{11}. This small-valued capacitor does not interfere with steady-state operation.

Because zero voltage and current are applied to S_{11} while in trapezoidal modulation, the contactor can be freely switched with minimal switching stress and without interrupting power delivery, eliminating the impact of the long contactor switching transient. To further develop the transitions, the switching-frequency dynamics of converter mode transition are also minimized

using a switching sequence that allows the converter to immediately transition into steady-state within one switching cycle.

Different startup control schemes for a DAB mode are proposed in [125]. However, due to the special construction of the transformer in this mode, the magnetizing inductance is not significantly larger than the leakage inductance, as would be traditional in a DAB transformer. Because of this, fast, seamless transitions between operating modes require active control of both leakage and magnetizing current states through a set of switching actions of the high-frequency power switches (S_1-S_8).

5.2.1 ZCS Transition

The proposed ZCS transition waveform is shown in Figure 5.5. When the converter transits from the high power region to the low power region, the controller shifts the interleaved boost mode to in-phase boost mode with one switching action. The interleaved phases will get the same current value at

$$\begin{aligned} I(t_1) &= I_{min} + \frac{V_B(|2D-1|T_s + (t_1 - t_0))}{L_{boost}} \\ &= I_{max} - \frac{V_{HV} - V_B}{L_{boost}}(t_1 - t_0) \end{aligned} \tag{5-2}$$

The time required to reach that current level is

$$(t_1 - t_0) = \frac{(I_{max} - I_{min})L_{boost} - T_s V_B(|1-2D|)}{2V_{HV}} \tag{5-3}$$

For 50% duty ratio of the boost mode, the required time is

$$(t_1 - t_0) = \frac{(I_{max} - I_{min})L_{boost}}{V_{HV}} \tag{5-4}$$

The two in-phase currents are then ramped down to zero during the off-time interval, whose duration depends on the minimum value of the ripple current and the boost inductance value. The contactor current is equal to the sum of these two currents; once the currents reduce to zero, zero current is ensured through the BMS contactor. The time required to ramp the current down to zero is

$$(t_3 - t_1) = L_{boost}\frac{I(t_1)}{V_{HV}} \tag{5-5}$$

The controller then sends a signal to disconnect the contactor. To maintain power flow during the lengthy BMS contactor transition time, trapezoidal modulation of the DAB is initiated.

The switching actions at t_3-t_5 are used to achieve steady-state current through the leakage and magnetizing inductance. First, the magnetizing current is raised to its steady-state value by operating primary and secondary bridges in phase. The time required to reach the steady-state magnetizing current developed in Chapter 4 for DAB mode is

$$(t_4 - t_3) = L_M\frac{I_{M_{peak}}}{V_n} \tag{5-6}$$

Once the peak steady-state magnetizing current at that power level is achieved, a smaller phase shift is introduced between the primary and secondary bridge. The phase shift is set to increase the primary and secondary current to the steady-state peak at t_4-t_5. At that time the magnetizing current remains in the steady-state. After t_5 regular trapezoidal modulation is continued.

After a delay to allow the contactor switching to complete, the transition from trapezoidal modulation to phase shift modulation is performed by increasing the duty cycle of the secondary phase legs to increase the continuous DAB mode efficiency [43].

5.2.2 ZVS Transition

The proposed ZVS transition waveform is shown in Figure 5.6. Before t_0, the converter operates in PS DAB mode. Using phase shift modulation, the CT point voltage is approximately half of the HV bus voltage. Due to this, there is a mismatch between the CT voltage and battery voltage; this difference is applied across the open BMS contactor. The converter is transitioned to trapezoidal modulation, controlling the duty cycle so that the CT point voltage is equal to the battery voltage. In this way, ZVS is achieved and the BMS contactor is commanded to once the CT voltage is equal to the battery voltage.

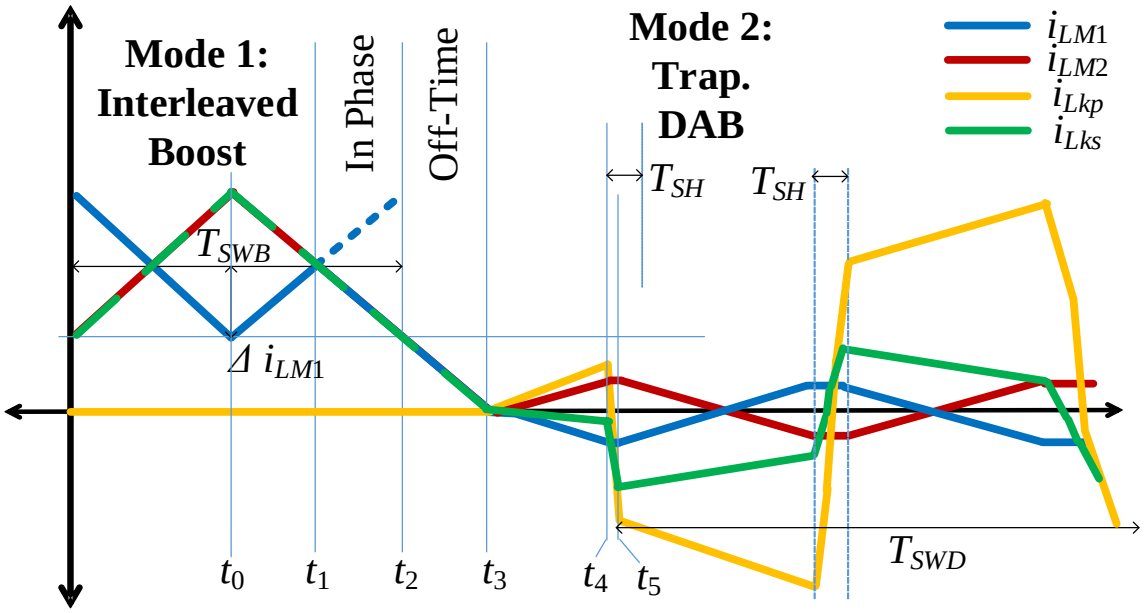

Figure 5.5. Zero current BMS contactor transition method.

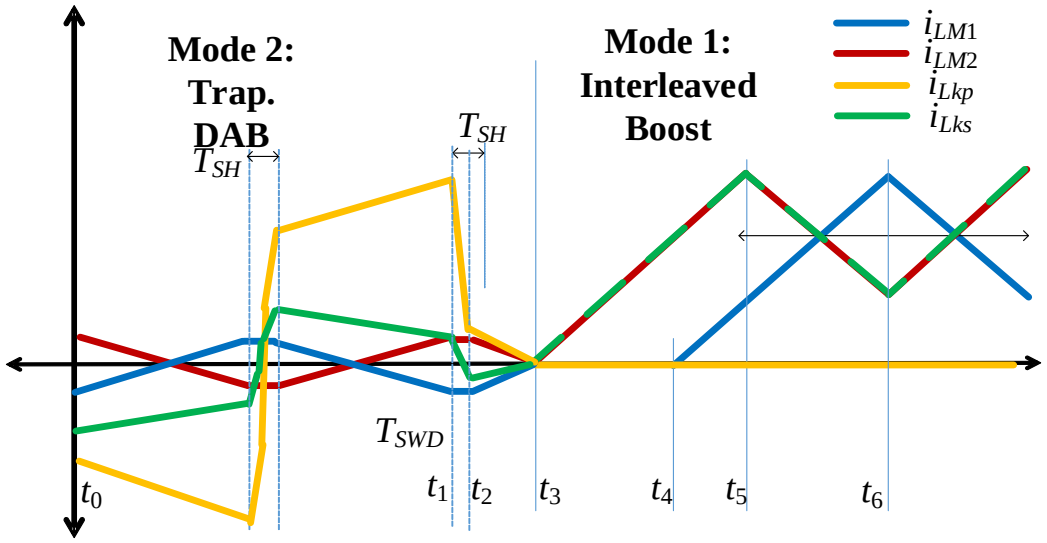

Figure 5.6. Zero voltage BMS contactor transition method.

Once the BMS contactor connects and bouncing subsides, boost operation is initiated. For boost startup, different methods are proposed including soft startup and time optimum control [128, 129]. These methods can be applied for the smooth startup of the boost mode.

5.3 Experimental Results

The transition waveforms are obtained for the 660 W traction operation for ZVS and ZCS transition. The experimental setup is presented in Chapter 3.

5.3.1 ZCS Transition

The integrated converter waveforms during the ZCS transition from boost mode to DAB mode are shown in Figure 5.7. During boost mode, all the currents are flowing through the BMS contactor and no current flows through the transformer primary bridge. From the boost to Trap. DAB transition, the transformer primary current increases from zero without any oscillation. During the trapezoidal modulation, the BMS contactor has a small ripple current due to the smaller

capacitor connected at the CT node. However, the average value of the BMS contactor current is zero. After the BMS contactor is disconnected, the contactor stops conducting current without any interruption in HV voltage or transformer currents. Finally, the PS DAB mode is initiated to reduce the integrated converter loss. The HV bus voltage is not affected by the transitions. The ZCS transition time is selected based on the specifications provided in the datasheet of the TE EV200AAANA Contactor.

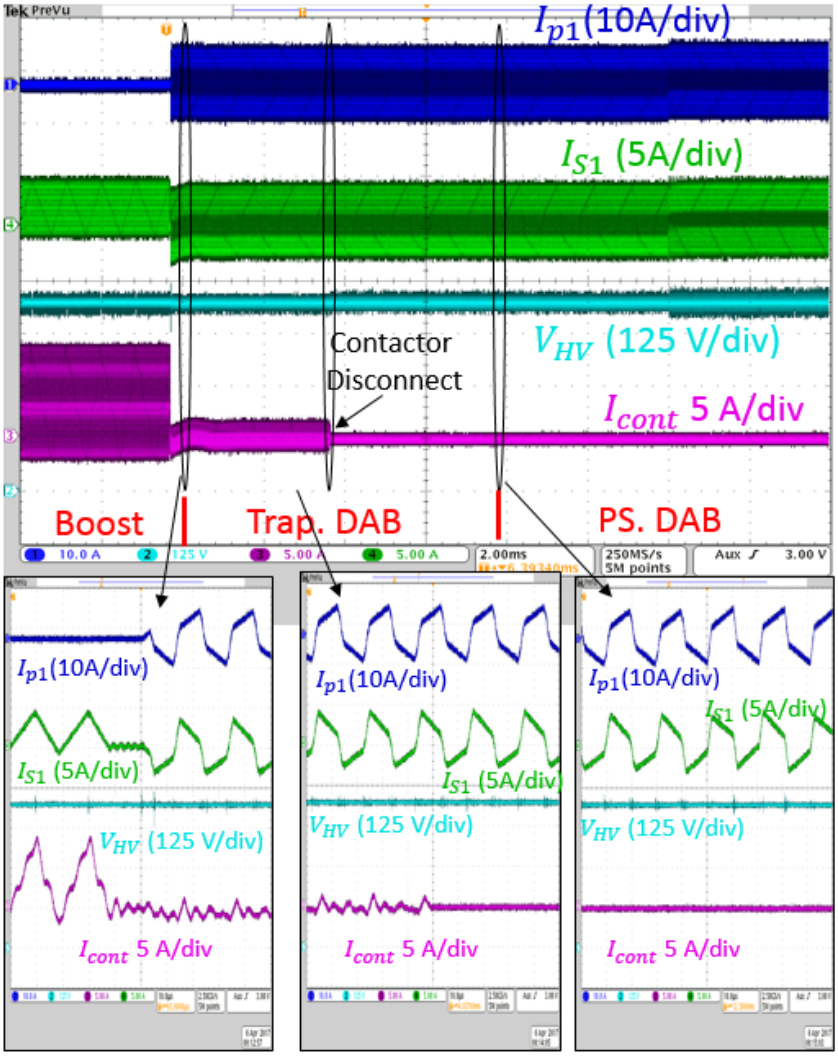

Figure 5.7. ZCS Transition: Mode 1 (Boost), Mode 2 (Trap DAB) and Mode 3 (PS. DAB).

The BMS contactor is disconnected in less than 4 ms in the experimental demonstration since the very small current flowing through the BMS contactor. As a result, less force is required for the BMS contactor disconnect.

5.3.2 ZVS Transition

The integrated converter during the ZVS transition from boost mode to DAB mode is shown in Figure 5.8. During the DAB PS modulation, both the primary and secondary winding of the transformer are conducting. From the PS DAB to Trap. DAB transition, the transformer primary and secondary current do not show any oscillation. During the Trap. DAB mode, the voltage across the BMS contactor is controlled to be as small as possible to ensure ZVS turn-on of the BMS contactor. The BMS contactor is turned on after 10 ms to allow the currents to be stable during Trap. DAB mode. After the BMS contactor is connected, the current starts flowing through the BMS contactor without any interruption in HV voltage or transformer currents. However, some oscillation of the current through the BMS conductor is observed which does not affect the converter operation. The oscillation of the BMS contactor current occurs as the voltage across the capacitor connected at the center node of the hybrid transformer has some ripple. The HV bus voltage remains regulated during the mode transitions. The transition time is selected based on the worst-case consideration given in Table 5.1 and some time is given to stabilize the trap. DAB mode.

The ZVS and ZCS transitions of the integrated converter maintains HV bus voltage regulation. The power flow is not interrupted as shown by the experimental waveforms. As a result, the capacitance requirement for the HV bus voltage holdup is reduced significantly.

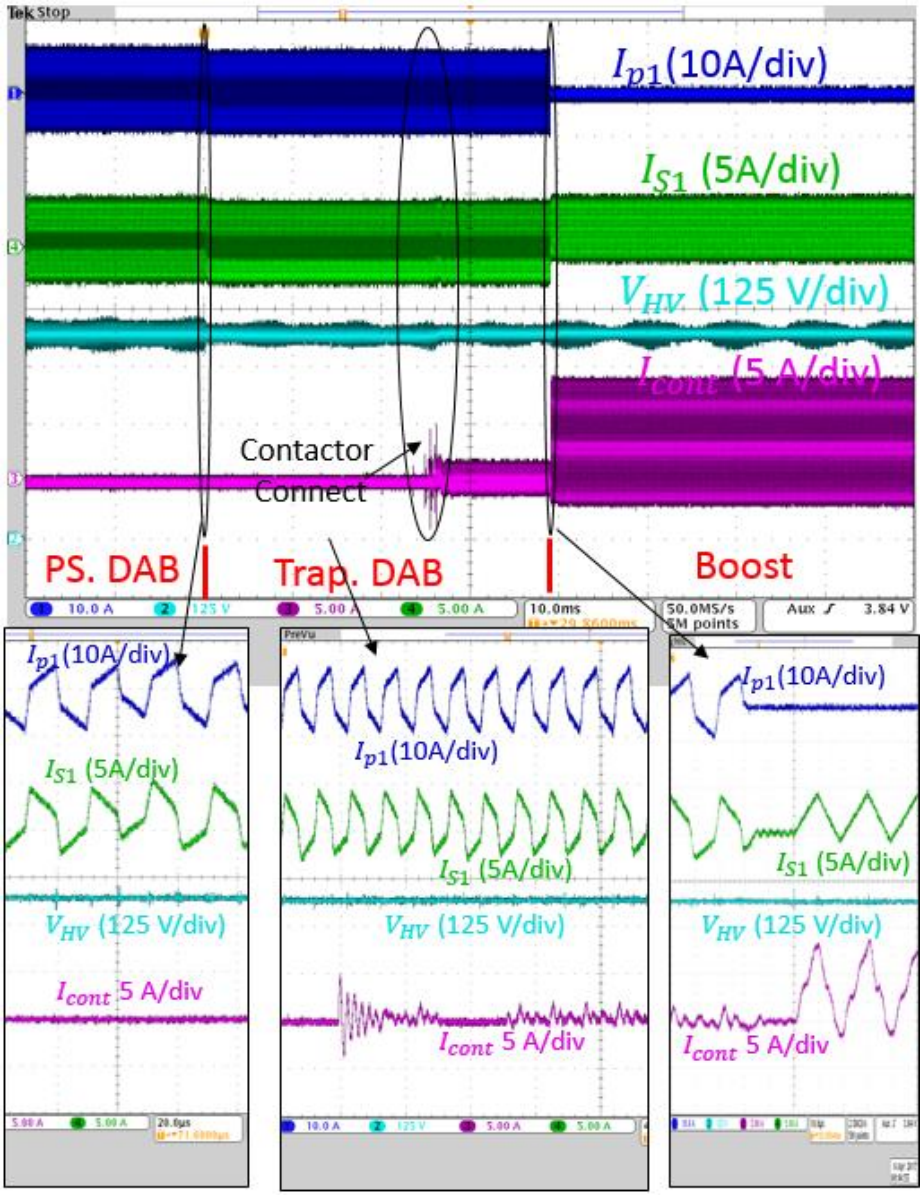

Figure 5.8. ZVS Transition: Mode 3 (PS. DAB), Mode 2 (Trap DAB) and Mode 1 (Boost).

5.4 Summary

A seamless transition strategy for the integrated converter topology for EV powertrains is proposed that will help the converter to achieve higher efficiency in traction operation. Zero current turn-on and zero current turn-off of the BMS contactor is ensured to eliminate stress,

arching, loss, and associated transients. A trapezoidal modulation strategy in DAB mode is adopted to ensure power flow through the transformer during the BMS contactor transition and provide zero voltage across the BMS contactor simultaneously. In this way, the long BMS contactor transition time does not impact the power flow of the system and the requirement of the extra capacitance is eliminated. This allows the integrated converter to reduce the price and weight of EV power electronics without detrimental impacts on passives or robustness of mechanical switches. The online transition also provides the possibility to improve integrated traction efficiency by operating between the boost and DAB mode.

6 Design Optimization

The online transition enables the integrated converter to improve traction efficiency. Using the advantage, a multi-objective optimization is proposed in this chapter to improve the integrated converter design in all aspects – reduced traction energy loss, reduced weight, and reduced price. Different design parameters including devices, cores, hybrid magnetics fill factor, switching frequency, and current ripple are considered to optimize the integrated converter design. The loss models developed in Chapter 4 are used for the integrated converter design optimization.

6.1 Driving Schedule Analysis

The driving schedule or cycle represents the speed of a vehicle versus time on different driving conditions produced by different countries and agencies [130]. The driving schedules are important to evaluate vehicle performance under representative operating conditions.

To demonstrate both city and highway driving conditions, the urban dynamometer drive cycle (UDDS) and highway drive cycle are combined. In Figure 6.1, the aggregated the drive cycle combining one highway drive cycle and two UDDS drive cycle is shown. The required power for an EV to follow this speed profile is

$$P = \left(M_v a + \frac{1}{2}\rho_{air} C_d A_v v^2 + C_r M_v g\right) v \tag{6-1}$$

where, M_v, a, ρ_{air}, C_d, A_v, C_r, g, and v are the mass, acceleration, air density, drag coefficient, frontal area, friction coefficient, gravitational acceleration, and velocity of the vehicle respectively. The vehicle parameters used for the optimization are given in Table 6.1.

Table 6.1. Vehicle parameters used for the optimization

Parameters	Value
Curb weight of vehicle, M_v (kg)	1000
Vehicle frontal area, A_v (m^2)	2.22
The coefficient of drag, C_d	0.25
Air density, ρ_{air} (kg/m^3)	1.204
Gravitational acceleration, g (m/s^2)	9.8
Wheel diameter (inch)	16
The coefficient of friction, C_r	0.01

The instantaneous power required by the integrated converter is shown in Figure 6.2. The peak power required by the integrated DC-DC converter for the drive cycle is 19.8 kW. Based on the vehicle speed and power requirement, the motor speed and torque are solved.

The frequency of occurrence of various operating points for the aggregated drive cycle is shown in Figure 6.3. The EV spends most of the city driving conditions around 4000 RPM speed and 10 N-m torque. The DAB converter can improve the traction efficiency in this region. The highway driving condition is represented at 8500 RPM speed and 20 N-m torque conditions where the boost converter is more efficient.

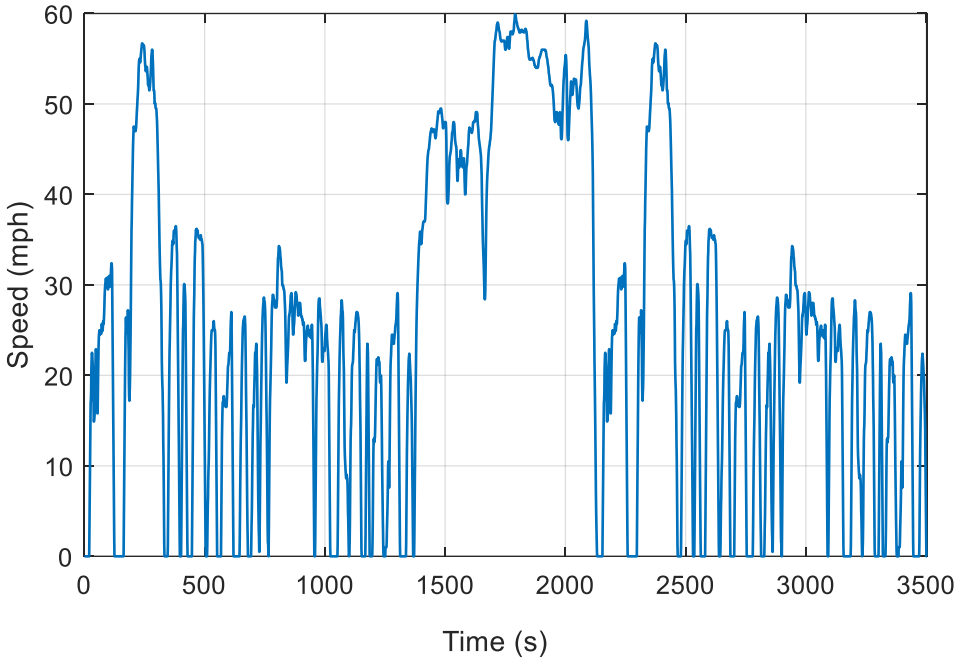

Figure 6.1. Aggregated drive cycle considered for optimization.

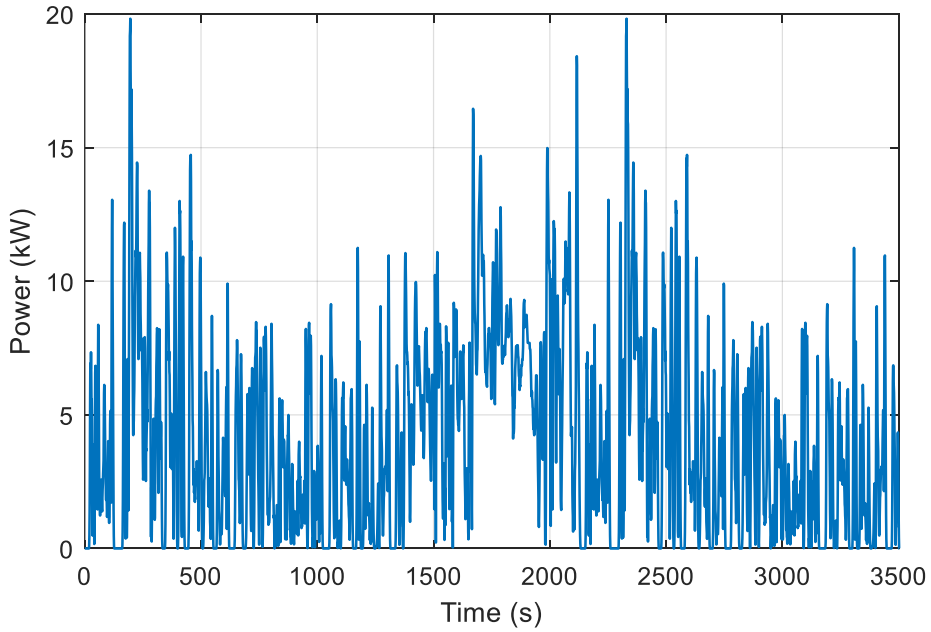

Figure 6.2. Power requirement for the aggregated drive cycle.

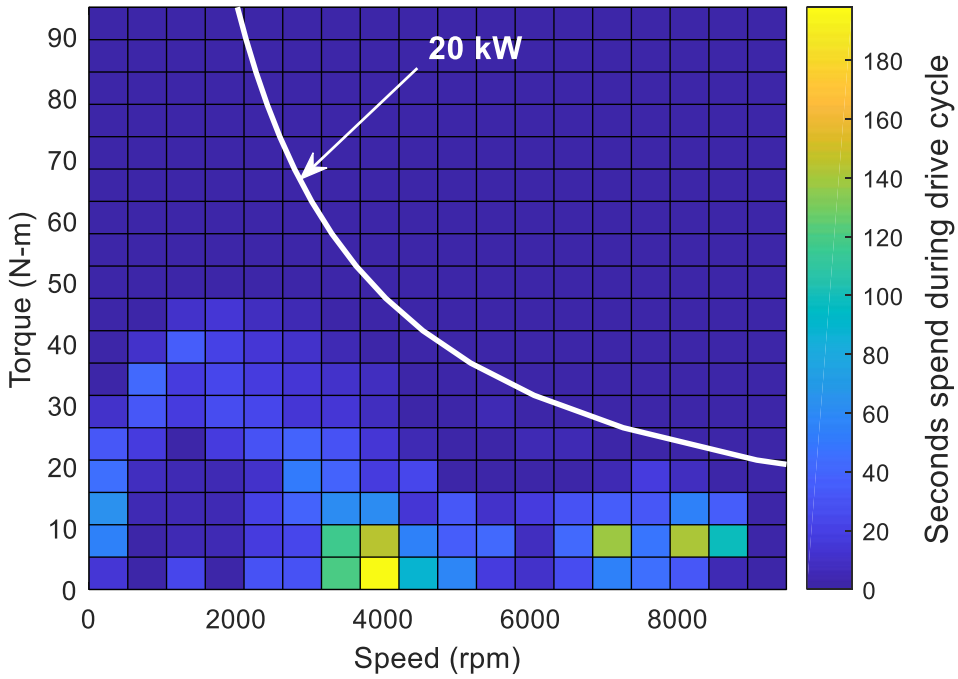

Figure 6.3. Histogram of the required speed-torque characteristics of the EVs.

6.2 Motor-Inverter Efficiency

For the traction drive, the motor-inverter efficiency is also considered along with the integrated converter. The motor-inverter efficiency varies at the different driving condition. The motor-inverter efficiency contours for the 2010 Toyota Prius at different bus voltage are shown in Figure 6.4, Figure 6.5, and Figure 6.6 respectively [13]. The overall traction efficiency is

$$\eta_{traction} = \eta_{integrated\ DC-DC} \times \eta_{inverter} \times \eta_{motor} \tag{6-2}$$

where $\eta_{integrated\ DC-DC}$, $\eta_{inverter}$, and η_{motor} are integrated DC-DC stage efficiency, inverter efficiency, and motor efficiency respectively. The motor-inverter efficiency contour of the 2010 Toyota Prius is considered for the integrated converter design consideration. The integrated DC-

DC converter is designed based on the combined motor-inverter efficiency to reduce converter loss, weight, and price. The efficiency curves are imported as three-dimensional torque, speed, and voltage profile as shown in Figure 6.7. The efficiency points for different inverter bus voltage are interpolated. At light load, low torque condition, high traction drive efficiency can be achieved if the motor-inverter is operated at 650 V bus voltage.

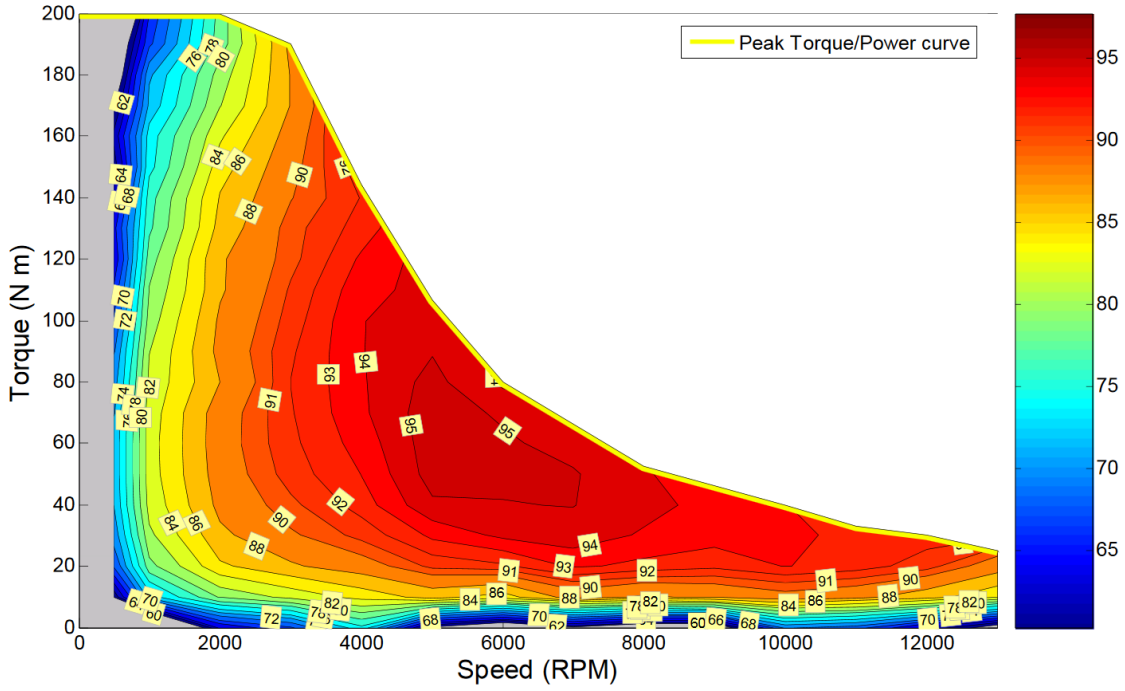

Figure 6.4. Combined motor inverter efficiency contours of 2010 Toyota Prius at 650 V [13].

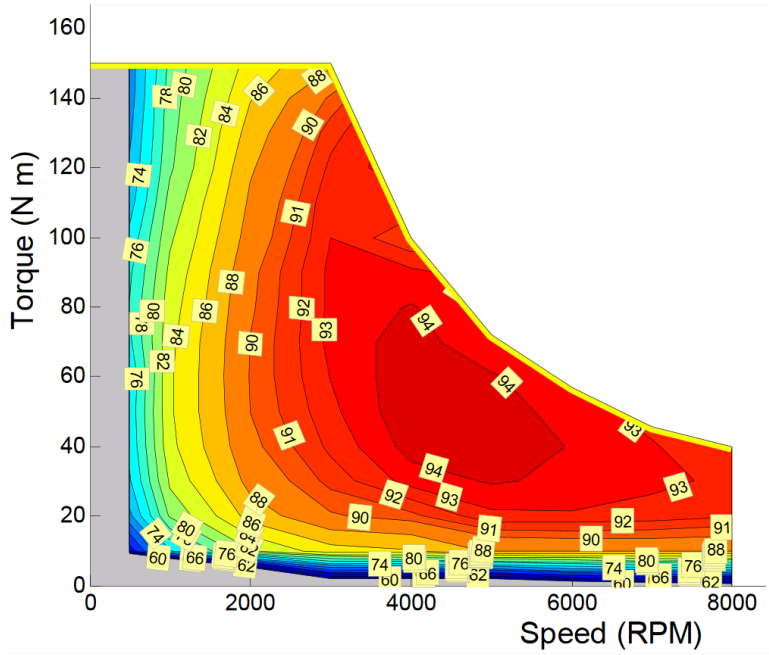

Figure 6.5. Combined motor inverter efficiency contours of 2010 Toyota Prius at 500 V [13].

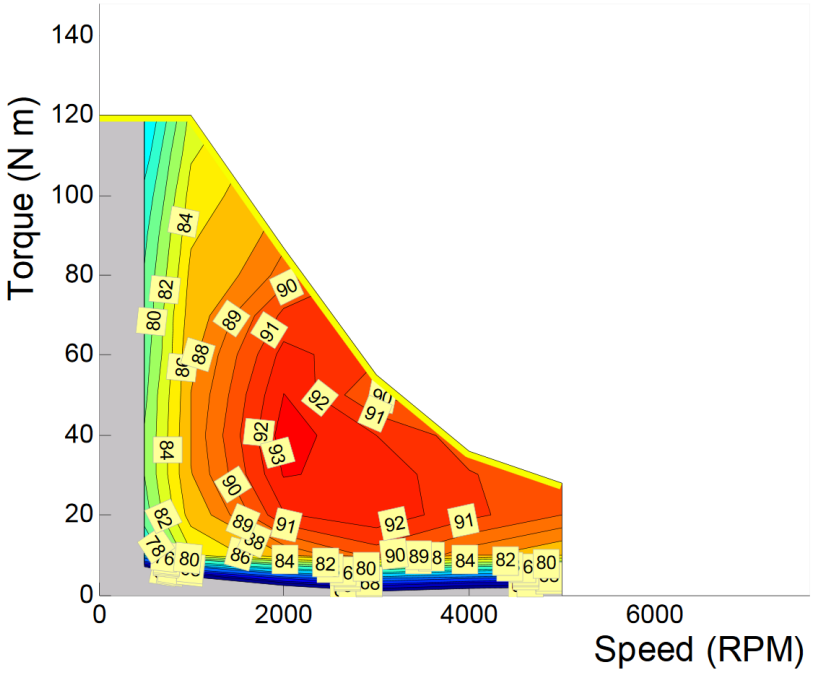

Figure 6.6. Combined motor inverter efficiency contours of 2010 Toyota Prius at 225 V [13].

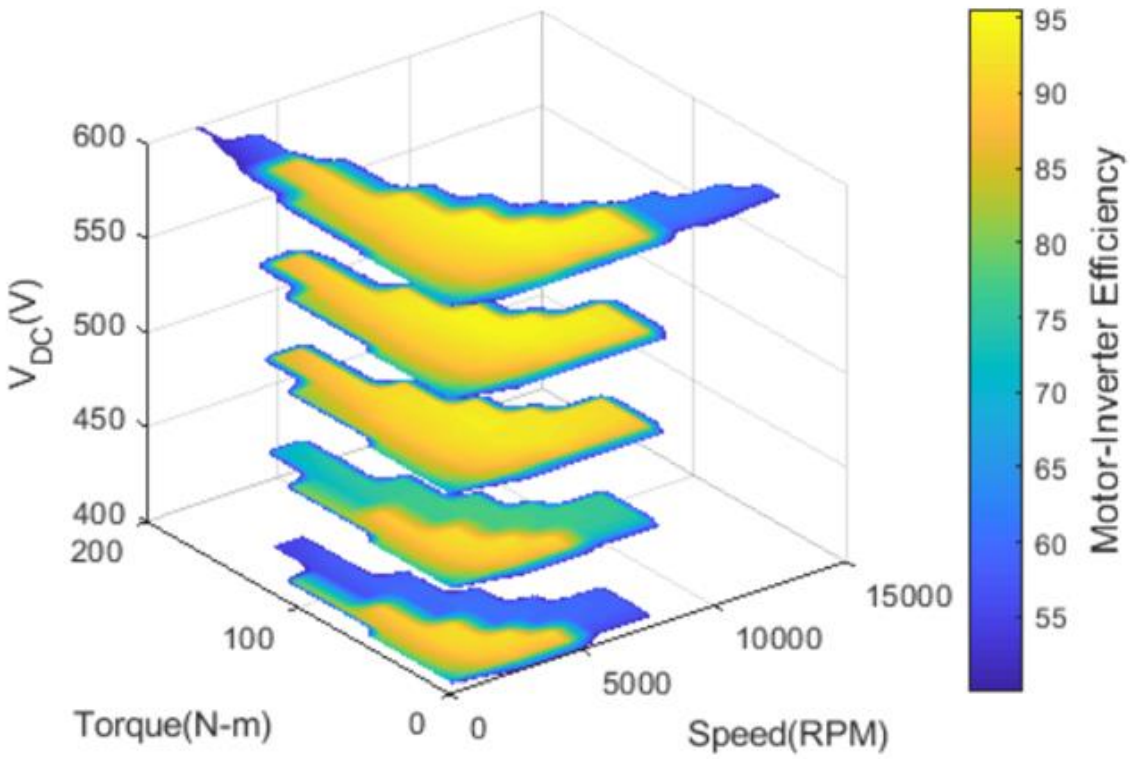

Figure 6.7. Combined motor inverter efficiency for optimization.

6.3 Price and Weight Model

The weight of a DC-DC converter is mainly contributed by the heavy magnetic core, winding, and heat sink [13, 131]. The price of the nanocrystalline core is included for the price analysis since the nanocrystalline core price is comparable with the power devices.

The database for the primary side devices is given in Table 6.2. The devices can be used in parallel as well. The turn-off switching energy for different load current and device output capacitance energy at different voltage is modeled using polynomial curve-fit from the device datasheet. For the high-power boost converter, a custom SiC power module is used. The

performance of a custom power module is compared with the CREE commercial module (CAS325M12HM2) in the optimization as well.

The cost model considers the primary and secondary side device price and the core price. From the device database and core database, the price is evaluated. The F3CC nanocrystalline core price is obtained from the core manufacturers shown in Figure 6.8. The price includes a fixed processing cost and proportional to the weight cost. The core price can be modeled according to the weight of the core

$$C_{\$} = 0.25\ W_{core} + 112.5 \tag{6-3}$$

where W_{core} is the nanocrystalline core weight. The converter price will reduce significantly when a bulk price model is used rather than the unit price model. For simplicity, the converter cost is normalized by \$5,000 which is the approximate maximum total cost of the integrated converter.

The weight of a DC-DC converter is mainly contributed by the heavy magnetic core, winding, and heat sink. The heat sink is required to remove the heat from the power devices and magnetics. The heat sink weight is modeled as

$$W_{HS} = k_{HS} P_{Loss_{MAX}} \tag{6-4}$$

where k_{HS} and $P_{Loss_{MAX}}$ represents the heat sink coefficient and the maximum loss of the integrated converter in the whole operating region respectively. The heat sink coefficient is estimated considering the 2010 Toyota Prius bidirectional DC-DC converter cooling infrastructure. Since the heat sink design is also related to converter loss, it does not change the optimization minimum values.

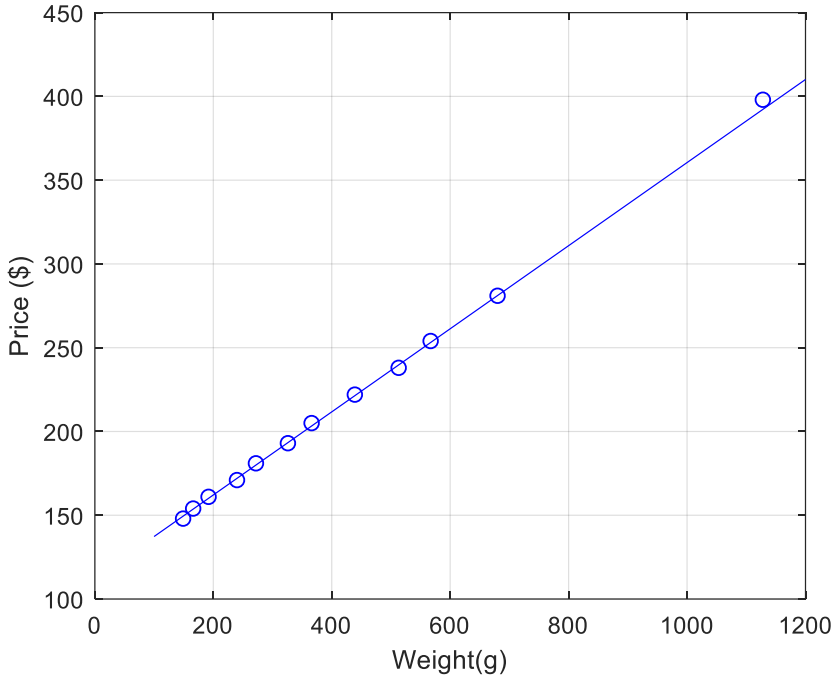

Figure 6.8. F3CC nanocrystalline core price vs. weight model.

Table 6.2. Primary side devices for integrated converter

Devices	Manufacturers	$R_{DS\,on\,@\,25°C}$ (mΩ)	Price ($)
SCT3022AL	ROHM	22	42
SCT3017AL	ROHM	17	97
C3M0030090K	CREE	30	30
C3M0065090J	CREE	65	11

6.4 Design Optimization Process

The objective of the integrated converter design optimization is to reduce the integrated converter weight, cost, and traction energy loss. However, the multi-objective optimization is challenging to solve since there is no unique solution. In the multi-objective optimization process, a set of solutions can be obtained which cannot be improved without adversely affecting at least one other objective [132]. These solutions are the Pareto front. The Pareto front is useful to visualize the tradeoffs of the different solutions.

The main optimization objective is to minimize the integrated converter energy loss, weight, and price. The cost function is

$$C = k_1 E_{loss} + k_2 W + k_3 C_{\$} \tag{6-5}$$

where E_{loss}, W, and $C_{\$}$ are the converter energy loss over the aggregated drive cycle, the weight of the converter, and the price of the converter respectively. The design specifications for optimization are given in Table 6.3.

The design variables are boost converter switching frequency, boost converter current ripple, the DAB converter switching frequency, hybrid transformer fill factor, different nanocrystalline cores, number of core stacks, and different primary side devices. The design flow diagram is shown in Figure 6.9. The boost inductance is calculated for an initial boost fill factor and the given operating conditions for every selection of switching frequency and current ripple using Section 3.4. From the core database, the air-gap, number of turns, and the secondary wire gauge are selected for each core. The core loss, winding loss, and the gap loss are calculated for every core using Section 4.1. The conduction and switching loss are calculated for each device from the device database. The device database includes device on-state resistance, switching energy

information, and the price of the device. For every core, the primary winding area allocation for DAB stage is determined according to Section 3.4. The primary number of turns is evaluated based on the selected secondary number of turns. For each DAB switching frequency, the peak current through the magnetizing inductance is evaluated according to Section 4.2. Based on the current through the magnetizing inductance, the core loss, and gap loss are evaluated. The copper loss is evaluated from the winding thickness and the primary current through the winding. Using the DAB switching frequencies and the primary side device database, the primary side loss is evaluated for every device and every set of switching frequencies according to Section 4.3.

From the combined boost-DAB converter efficiency and the inverter efficiency, the energy loss in the drive cycle is evaluated using Equation 6-2. The heat sink weight is defined from maximum integrated converter loss using Equation 6-4. The core also adds to the converter weight. From the device database and core database, the price is evaluated. Using the energy loss, price, and weight the Pareto front solutions are derived.

Table 6.3. Specification for the integrated converter prototype

Converter	**Boost Converter**	**DAB Converter**
Battery Voltage ($\boldsymbol{V_B}$) (V)	220	220
HV Bus Voltage ($\boldsymbol{V_{HV}}$) (V)	400 – 600	550 – 600
Power (kW)	20	6.6

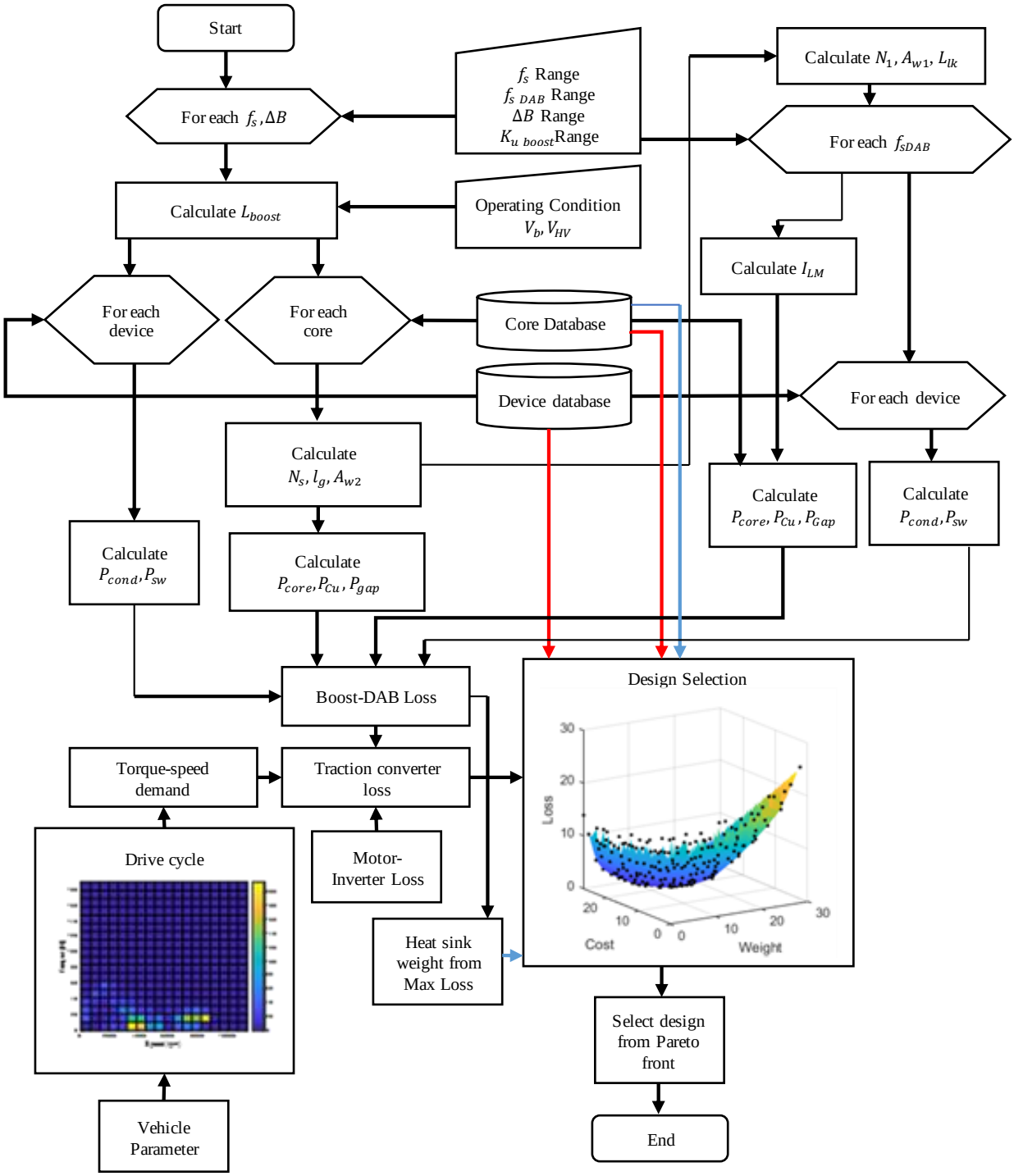

Figure 6.9. Design flow chart for the integrated converter.

The Pareto front optimization results for different boost winding fill factor ($k_{u,boost}$) are shown in Figure 6.10. The Pareto front that is closer to the origin results better results with lower traction energy loss, weight, and cost. The traction energy loss versus weight for different fill factors is shown in Figure 6.11. Comparing the Pareto front of 50%, 85%, and 94% boost winding fill factor, 85% boost winding fill factor provides lower traction energy loss and lower core weight. The energy loss versus normalized price is shown in Figure 6.12. The integrated converters with 85% boost winding fill factor generate lower loss and core weight compared to 50% and 94% boost winding fill factor designs. As a result, integrated converters with 85% boost winding fill factor is selected for the integrated converter design.

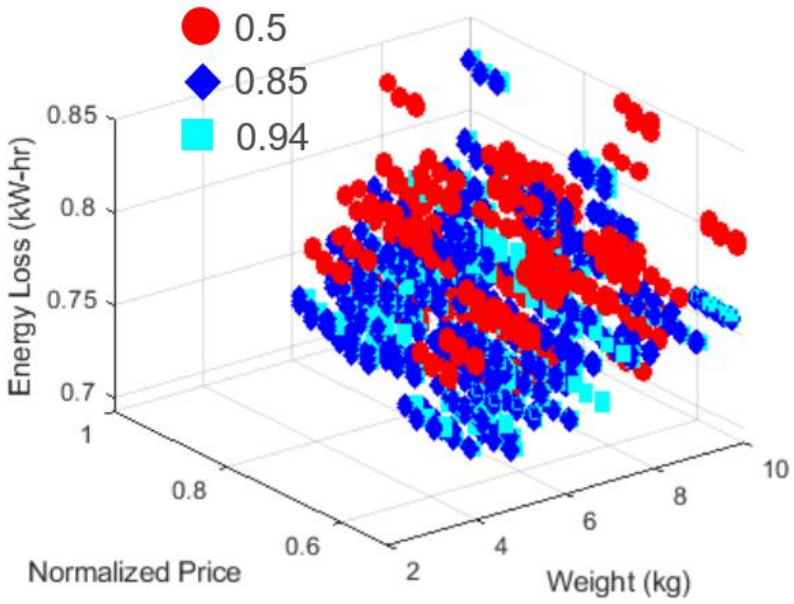

Figure 6.10. Pareto front optimization results for different boost winding fill factor.

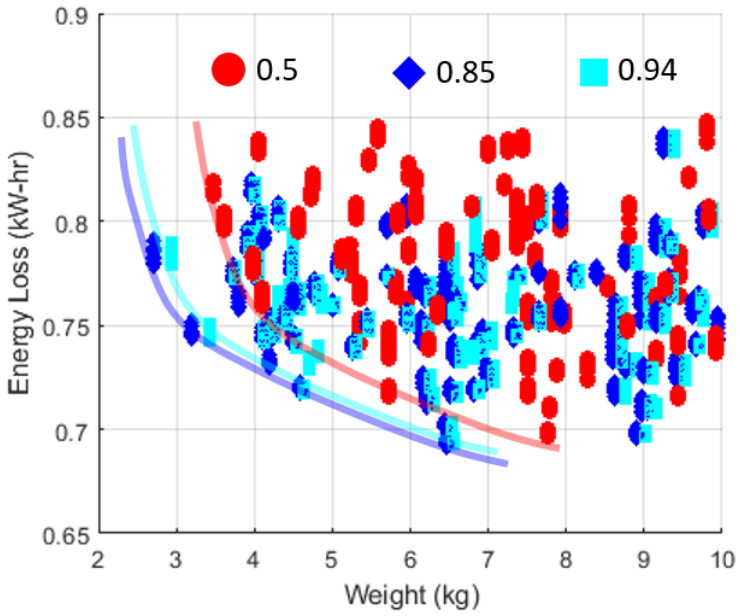

Figure 6.11. Pareto front for traction energy loss versus weight for different boost winding fill factor.

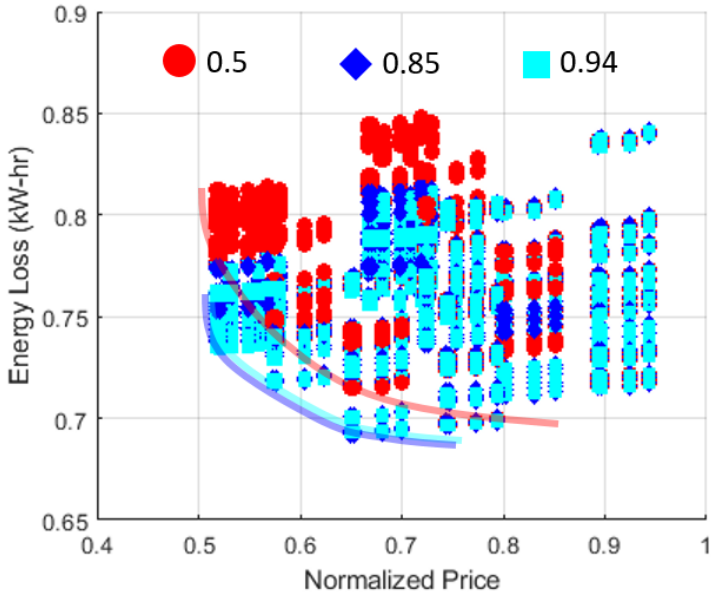

Figure 6.12. Pareto front for traction energy loss versus normalized price using the Pareto front optimization.

The Pareto front optimization results for different integrated converter solutions with 85% boost winding fill factor and separated boost-DAB converter are presented in Figure 6.13. The traction energy loss versus converter weight is shown in Figure 6.14. The integrated converter reduces the traction energy loss compared to a separate boost-DAB converter solution while reducing the total converter weight. The traction energy loss versus normalized price is shown in Figure 6.15. The integrated converter can reduce the traction energy loss by the online transition between the interleaved boost and DAB mode. At the same time, the cost is also reduced by sharing power devices and integrated magnetics. From the Pareto front, the integrated converter design is selected with 0.713 kW-hr energy loss, 4.58 kg weight, and 0.604 unit normalized price.

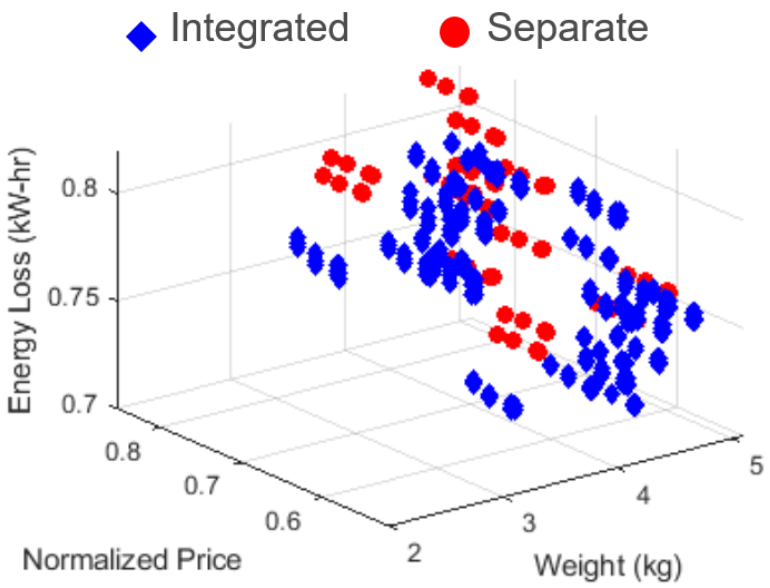

Figure 6.13. Pareto front optimization results for the integrated converter with 85% fill factor versus separate boost-DAB converter solutions.

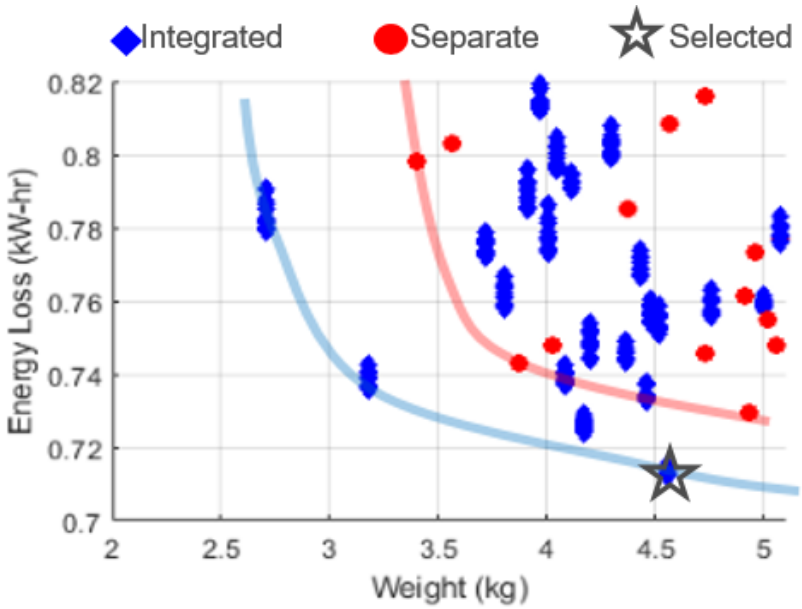

Figure 6.14. Pareto front for traction energy loss versus weight for integrated and separate boost-DAB solutions.

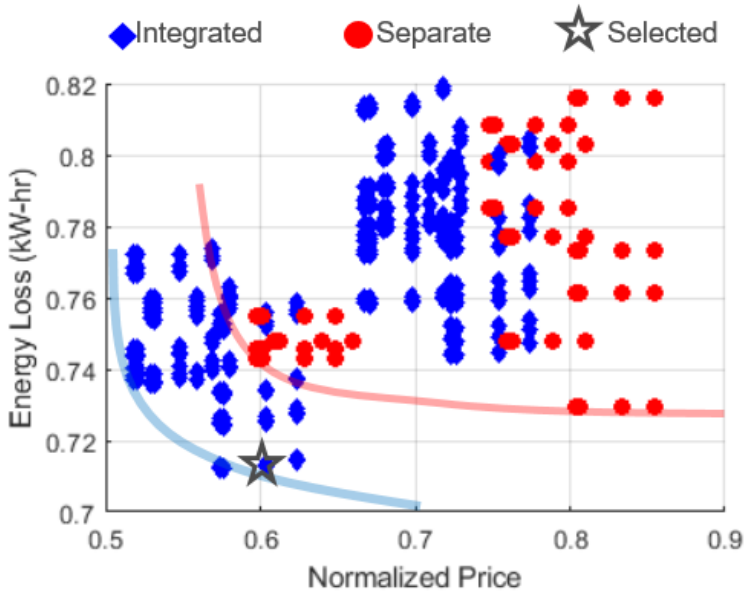

Figure 6.15. Pareto front for traction energy loss versus normalized price for integrated and separate boost-DAB solutions.

The traction energy loss comparison among integrated converter, separate converter, and integrated converter without online transition is presented in Figure 6.16. The integrated converter with an online transition can reduce traction loss as DAB can improve light-load efficiency. The separate boost converter efficiency is higher since the DAB mode is not available to improve the light load efficiency. The integrated converter without online transition results in the highest traction energy loss since the partial window area is allocated for the DAB winding.

The total energy required during the drive cycle is 2.51 kW-hr for the selected design choice from the Pareto front. The energy loss distribution is shown in Figure 6.17. The road load loss causes about 72% of the total energy consumption provided by the battery. The motor-inverter dissipates 0.64 kW-hr which is about 25% of the energy dissipated by the battery. The integrated DC-DC converter using online transition dissipates 0.0749 kW-hr which is 3% of the energy dissipated by the battery. For a separate boost converter solution, the energy lost during the traction drive cycle is 0.0823 kW-hr. As a result, utilizing the online transition between DAB and boost mode in traction operation can reduce traction energy loss by 8%.

Based on the design parameters, the boost stage will be operated with 50 kHz switching frequency, 25% current ripple, 85% boost winding fill factor, DAB operating frequency of 60 kHz, and 247 µH boost inductance using F3CC0125 nanocrystalline core. For the primary side, two parallel CREE SiC C3M0030090K devices are selected based on the optimization. The efficiency contour of the integrated converter in DAB mode is shown in Figure 6.19. The highest efficiency is achieved at around 3.5 kW and 600 V region. The efficiency contour of the integrated converter in boost mode is shown in Figure 6.20. The boost converter efficiency is low at the light-load region with a higher boosting ratio.

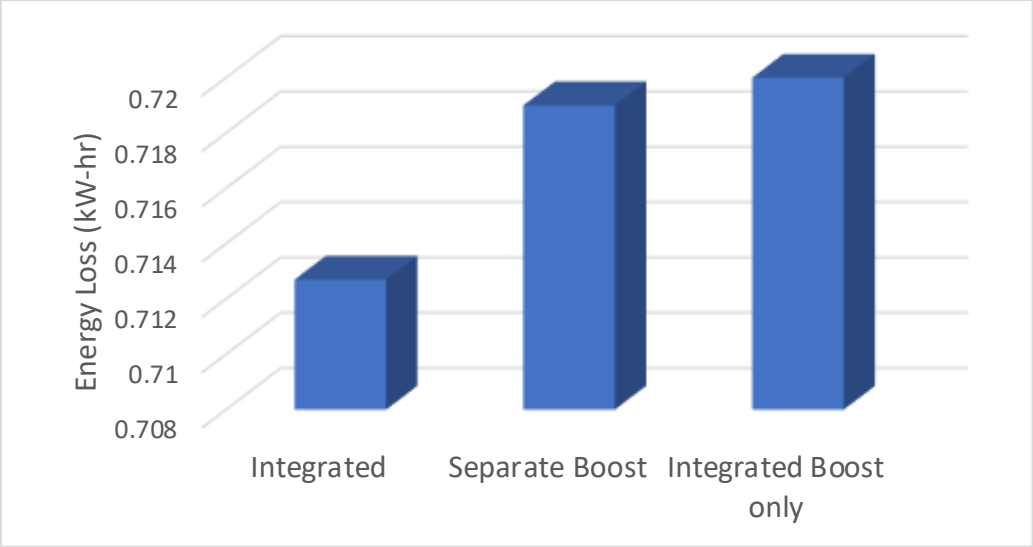

Figure 6.16. Energy loss comparison for the traction drive using different DC-DC traction converter.

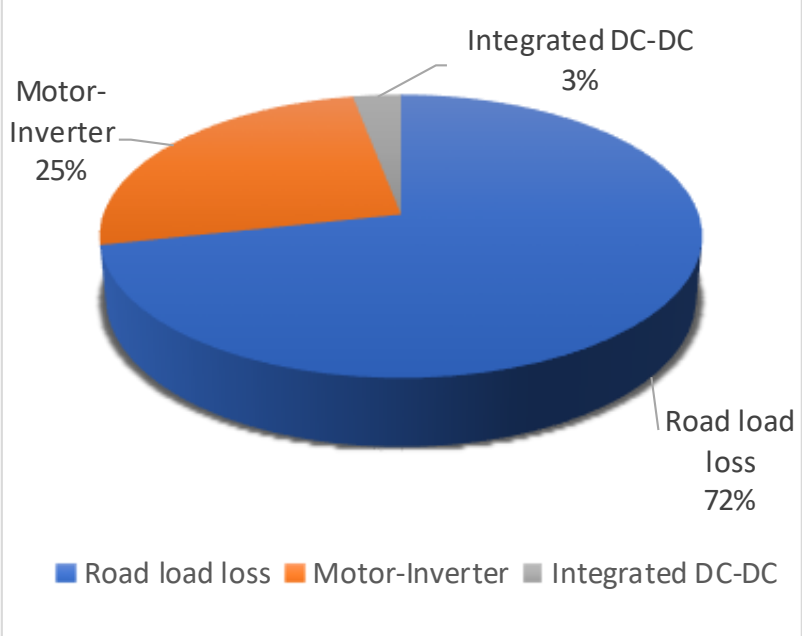

Figure 6.17. Energy loss breakdown for EV rolling and frontal resistance, motor-inverter, and integrated DC-DC converter.

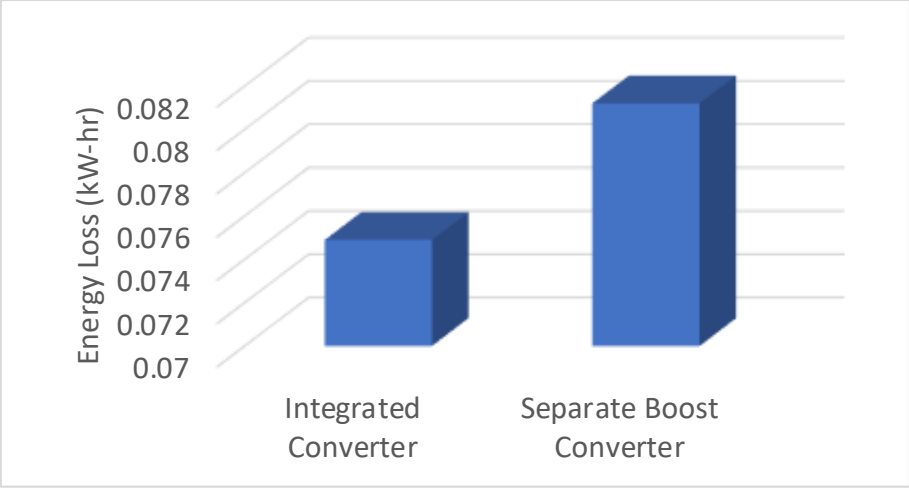

Figure 6.18. Energy loss comparison between the DC-DC stage for the drive system with integrated converter and a separate boost converter.

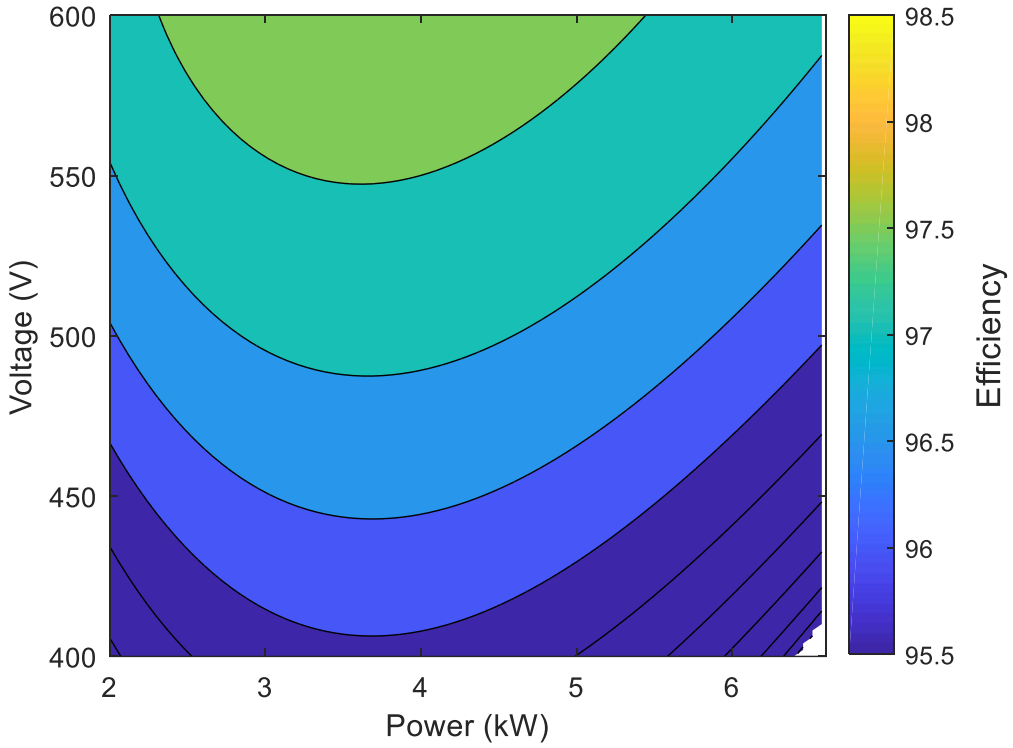

Figure 6.19. Integrated converter efficiency contour in DAB mode.

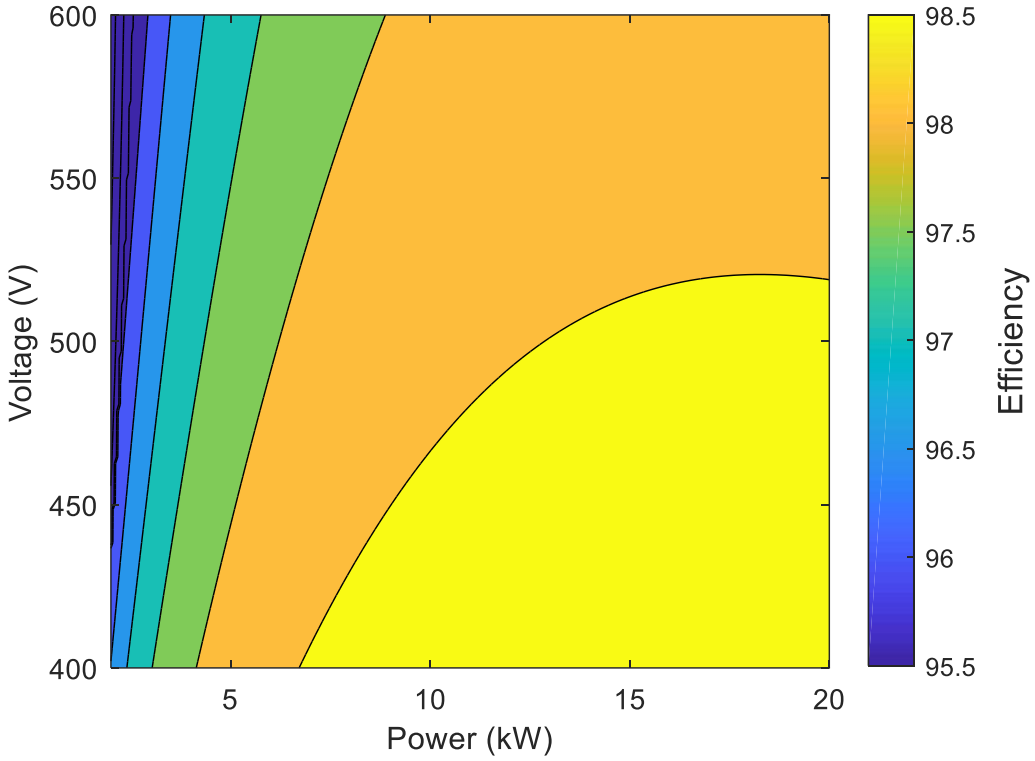

Figure 6.20. Integrated converter efficiency contour in boost mode.

The combined efficiency achieved by the online transition between the boost and DAB mode is presented in Figure 6.21. The integrated converter operates in DAB mode at the low power high voltage operating condition. Beyond 6.6 kW, the integrated converter automatically makes the transition from the DAB mode to the boost mode. In this way, the overall traction loss during the aggregated drive cycle can be reduced by 9%. Using the integrated converter design parameters obtained from optimization, a 20 kW prototype is developed to verify the power converter efficiency in different operating modes. An automatic closed-loop control system is developed as well to operate the integrated converter at different voltage and power levels.

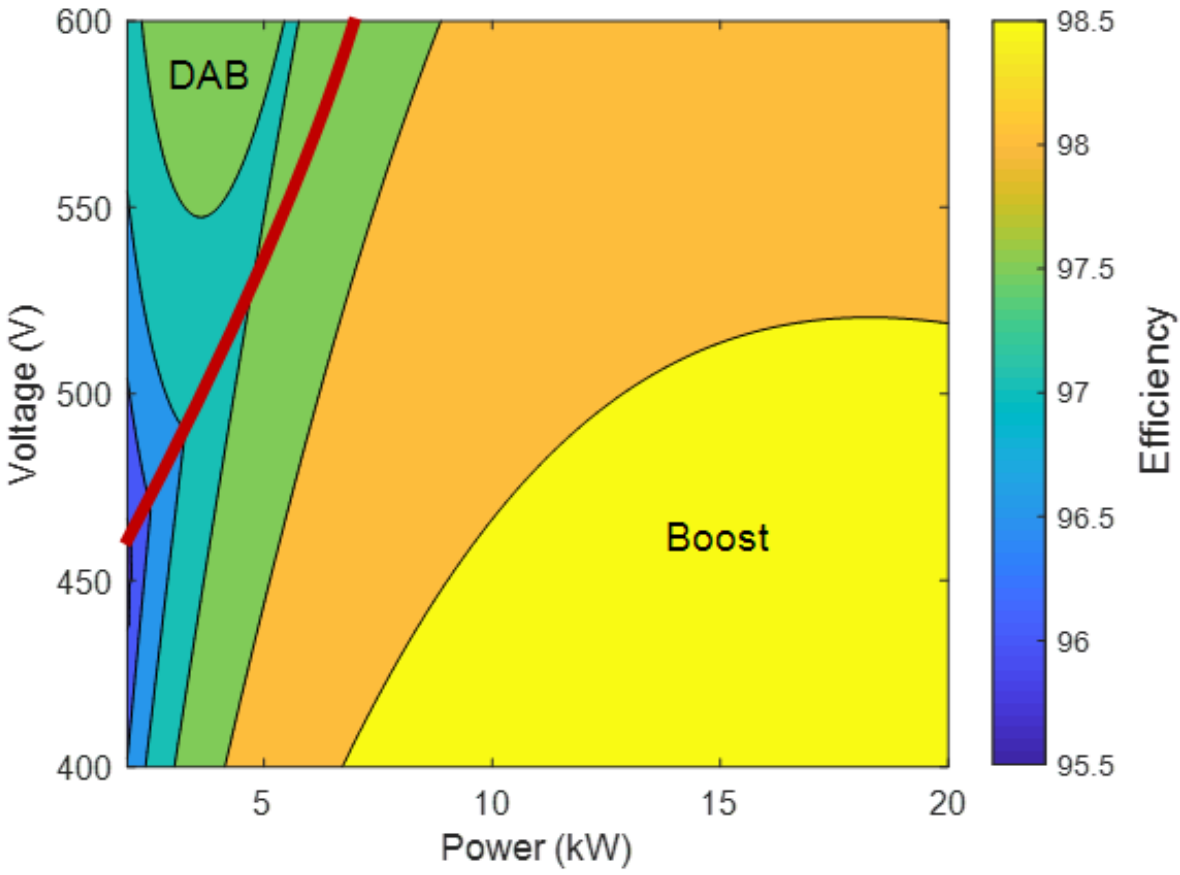

Figure 6.21. Integrated converter efficiency contours with the online transition algorithm.

Using the FEA model developed for gap loss evaluation in DAB mode in Section 4.3.4, the winding orientation is selected to reduce the loss in the hybrid transformer. The hybrid transformer winding orientation from the hybrid transformer is shown in Figure 6.22. The primary winding is placed in between the secondary winding to reduce the leakage inductance compared with the winding orientation next to the core or outside of the core. Interior and exterior lamination strips are modeled as described in Section 4.3.4 to evaluate the DAB fringe flux related loss near the air gap.

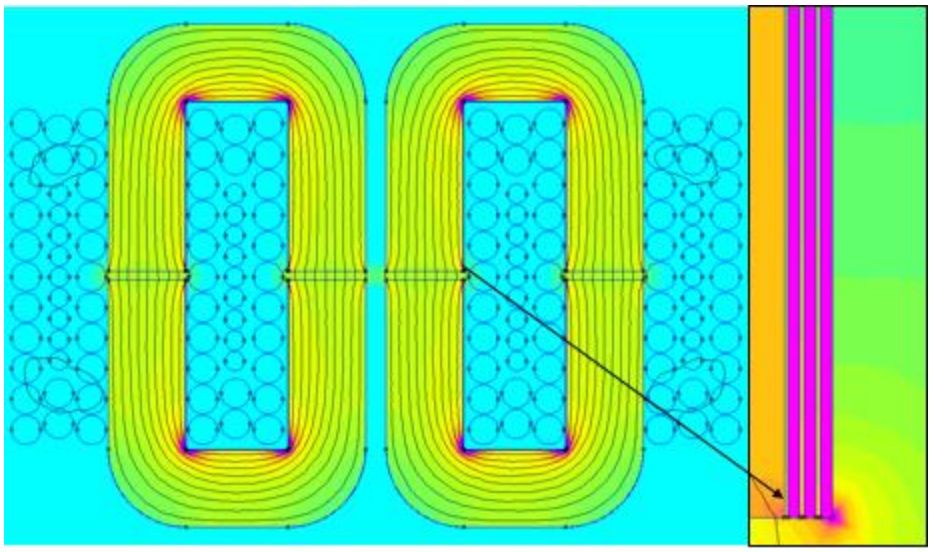

Figure 6.22. Primary and secondary winding orientation in the hybrid transformer for the full-power prototype.

6.5 Summary

Using the Pareto front optimization method, the integrated converter design parameters are optimized for full-power prototype development. The integrated converter can reduce the DC-DC stage energy consumption by 8% using the online transition algorithm. Compared with a separate powertrain-charger solution, the integrated converter can reduce the price by 9% and the weight by 12%. The DAB converter extends the traction boost efficiency from 96% to 98% at 600 V 3.5 kW traction operation. The next section describes an automated system that can detect the integrated converter power level, regulate the integrated converter output voltage, and ensure a seamless transition between the boost and DAB modes.

7 High Power Integrated Converter

In this chapter, the high-power integrated converter prototype based on the optimization in the previous chapter is presented. Since the integrated converter can be operated in both boost mode and DAB mode, a closed-loop controller is developed for both modes. The automated transition algorithm proposed in Chapter 5 is implemented in the closed-loop controller. Finally, the integrated converter is tested at different points of a drive cycle to demonstrate closed-loop performance and online transition capability.

7.1 High Power Prototype Development

The integrated DC-DC converter includes a primary H bridge, secondary H bridge, and hybrid transformer designed based on Pareto front optimization. A digital signal processor (DSP) is used as the controller to operate the integrated converter in different operating modes, regulate the output voltage, monitor the power flow, control the online transition, and change the output voltage reference voltage at different point of the drive cycle based on a lookup table. The current and voltage sensors are also integrated to obtain feedback signals for the controller to regulate and monitor the output voltage, output power, and phase currents as shown in Figure 7.1.

7.1.1 Integrated Converter Development

The primary H bridge of the integrated converter is constructed using two parallel CREE C3M0030090K discrete devices for each switches S_1-S_4. The equivalent device turn-on resistance of the primary side switches is 15mΩ. The gate driver for the primary switches is designed with desaturation protection at 120 A peak current. The DC bus bar is constructed using a PCB board where the input filter capacitor is mounted and the phase current to hybrid transform is connected. The primary H bridge assembly with the cold plate is shown in Figure 7.2.

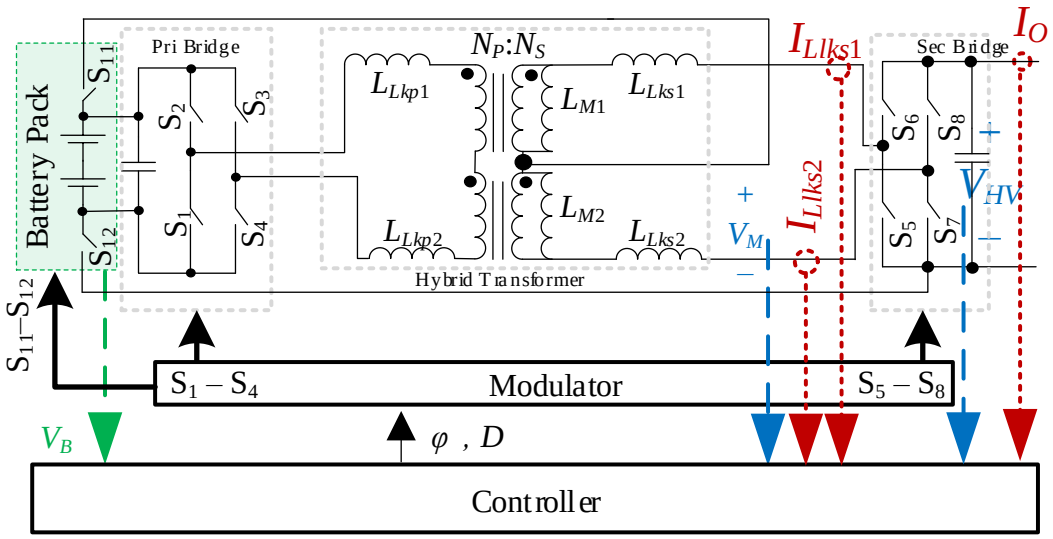

Figure 7.1. Integrated converter with primary and secondary H bridge, hybrid transformer, and feedback signals.

The secondary H bridge is constructed using a custom phase leg power module developed at ORNL described in [133, 134]. Six trench SiC dies are paralleled to implement the secondary side switches S_5-S_8. The bus bar is constructed using copper bars and the filter capacitor is attached to the copper bus bar. The secondary H bridge assembly with the cold plate is shown in Figure 7.3.

The hybrid transformer connects the primary and secondary H bridge. The hybrid transformer is constructed using two F3CC0125 Nanocrystalline U core pairs as shown in Figure 7.4. Using the design optimization, the primary winding is constructed using 10 AWG Litz wire and the secondary winding is constructed using 6 AWG Litz wire. The individual strand of the 10 AWG and 6 AWG Litz wire is selected as 38 AWG. For 50 kHz to 100 kHz switching frequency operation, Litz wire with 38 AWG of individual strands is recommended. The primary and

secondary winding is interleaved to reduce the AC loss and the winding orientation is shown in Figure 6.22. The hybrid transformer parameters are given in Table 7.1.

A TMS320F28335 DSP is used to control and generate modulating signals for SiC devices of the integrated converter as shown in Figure 7.5. For interleaved boost phase current measurement, two 200 kHz current sensors are used. For output current measurement, a 100 kHz bandwidth current sensor is used. To measure the output voltage and midpoint voltage of the hybrid transformer, two voltage sensors are used.

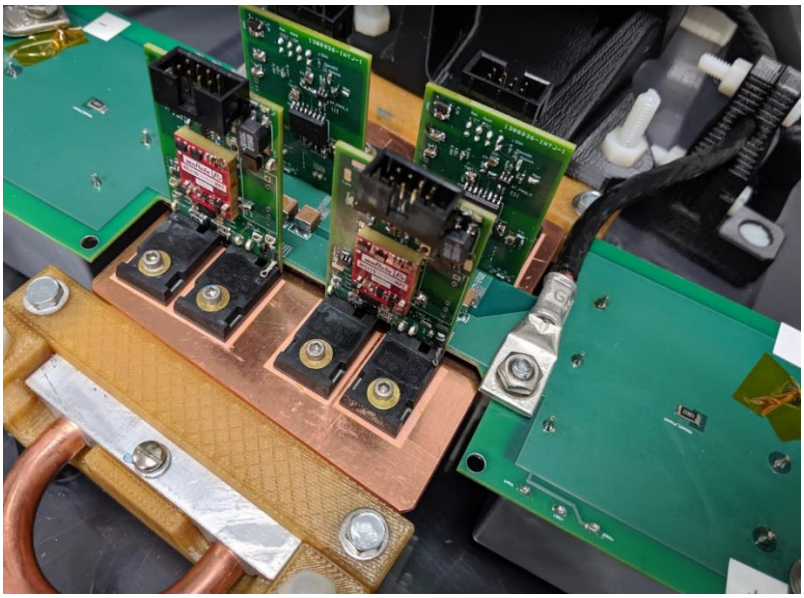

Figure 7.2. Experimental setup for the primary bridge of integrated converter.

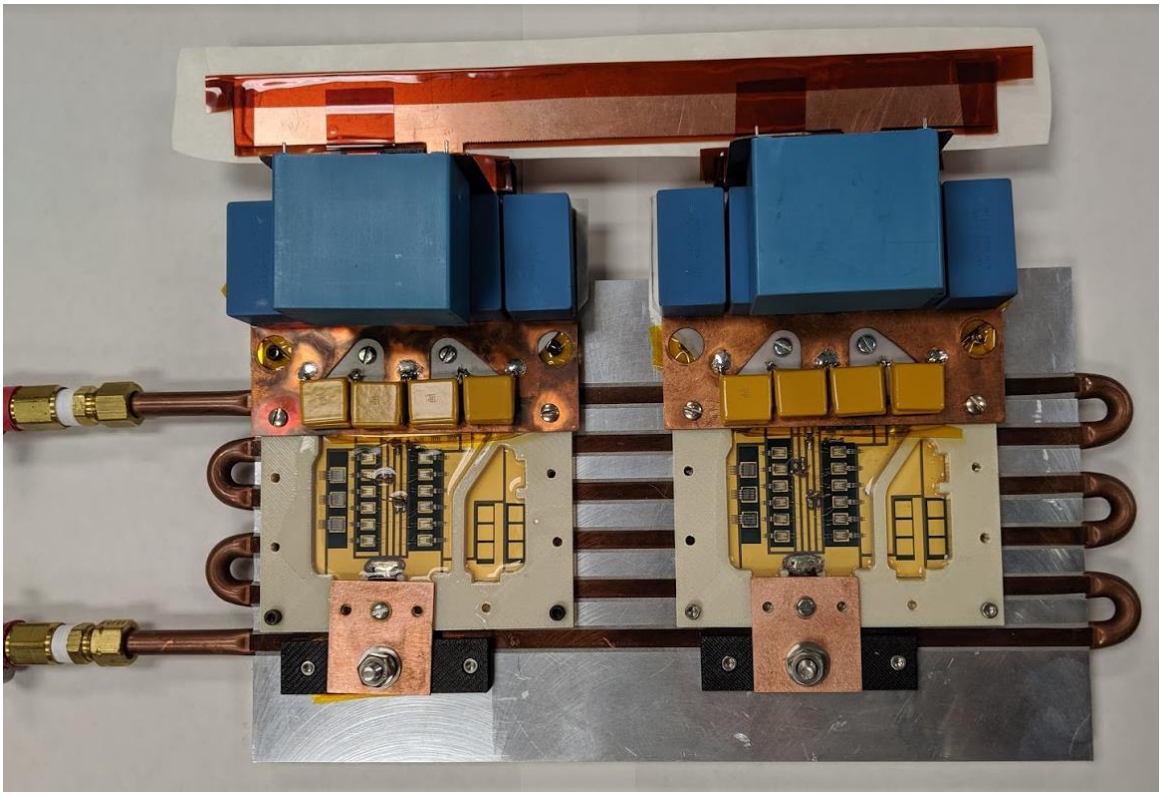

Figure 7.3. Experimental setup for the secondary bridge of integrated converter.

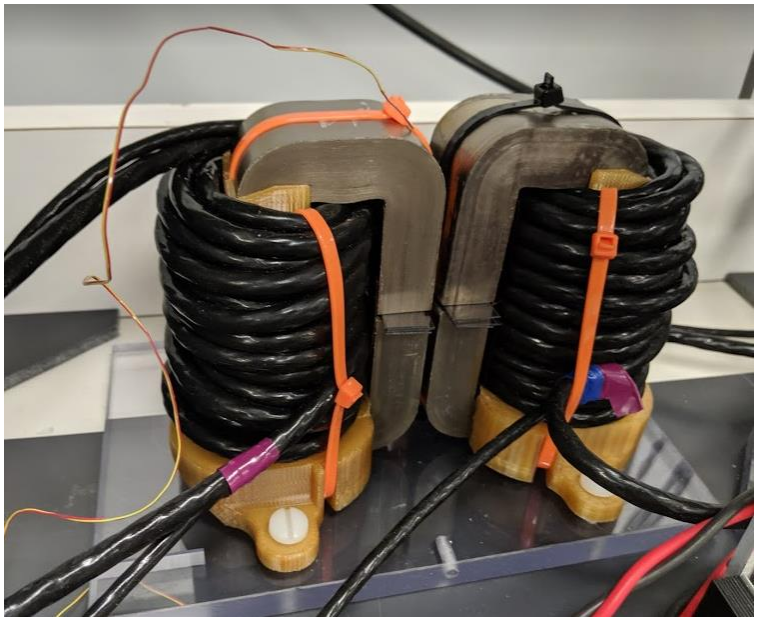

Figure 7.4. Hybrid magnetics for the integrated converter.

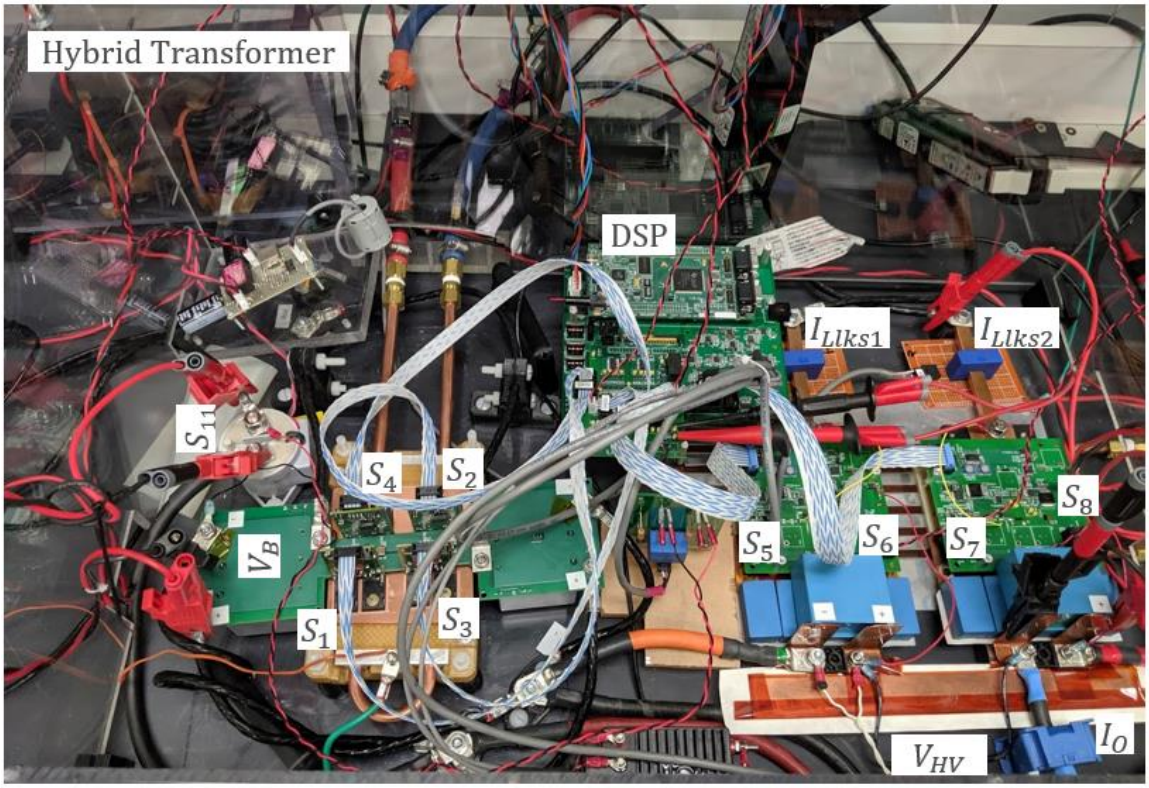

Figure 7.5. Integrated converter with controller and sensors.

Table 7.1. Hybrid transformer parameters

Parameters	Value
Nanocrystalline U Core Part	F3CC0125
Secondary leakage, L_M (µH)	220.61
Primary leakage inductance, L_{lkp} (µH)	2.53
Secondary leakage inductance, L_{lks} (µH)	17.89
Primary Number of Turns, N_P	9
Secondary number of turns, N_S	26
Effective turns ratio, n	2.66
Primary number of strands in Litz wire	660
Secondary number of strands in Litz wire	1650
Primary equivalent AWG	10
Secondary equivalent AWG	6
Primary and secondary individual strands AWG	38

7.1.2 Experimental Results

The integrated converter is tested in both boost mode and DAB. The interleaved boost mode is tested up to 20 kW and the phase shift DAB mode is tested up to 6.6 kW. The primary and secondary H bridge of the integrated converter is cooled at room temperature using a liquid cooling system. The hybrid transformers are cooled using forced airflow. A DC emulator from E&M power is used as a DC source of the integrated converter. For the integrated converter load, the Chroma 63210 DC electronic load and high voltage battery test system 9300 series from NH research is used.

The integrated converter is tested in DAB mode up to 6.6 kW where the phase shift is varied to control the output power of the integrated converter for a given reference voltage. The experimental waveform for the integrated converter operating in DAB mode at 3 kW at 600 V output voltage is shown in Figure 7.6. Both primary and secondary bridge is operating at ZVS operation. The waveshape of the current through the primary and secondary winding is different due to the presence of magnetizing current. The current peaks of the hybrid magnetics winding derived in Chapter 4 are also validated for different power levels during phase shift DAB operation shown in Figure 7.7. The efficiency sweep of the integrated converter in DAB mode for 550 V and 600 V output voltage is shown in Figure 7.8. The DAB mode is more efficient at 600 V than 550 V due to the turns ratio of the hybrid transformer. The DAB mode can provide higher efficiency due to the soft switching operation. During phase shift DAB operation, around 98% peak efficiency is recorded. The loss breakdown of the DAB converter at 600 V bus voltage is presented in Figure 7.9. The primary and secondary side conduction loss, switching loss, and winding loss increase at high of power. The core loss including gap loss is reduced slightly with increased power flow as more phase shift is required at a higher output power level.

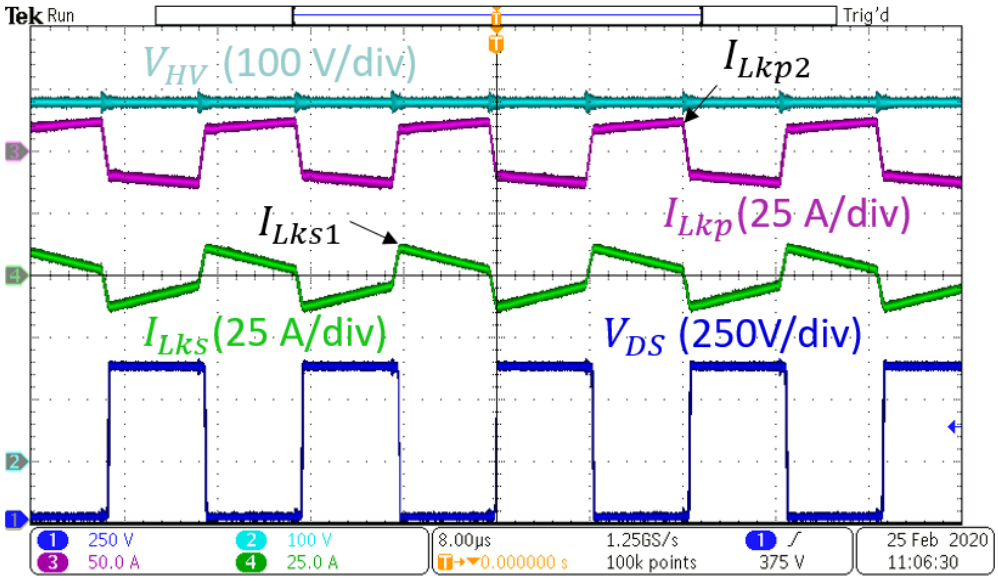

Figure 7.6. Integrated converter operating at 3 kW in DAB mode.

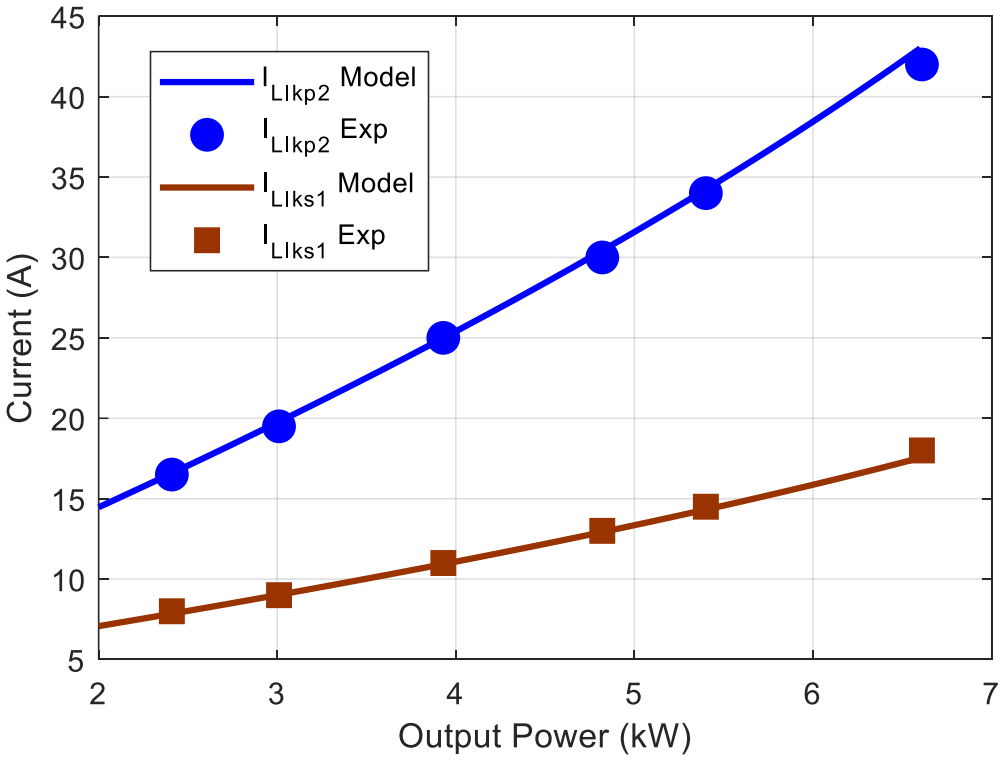

Figure 7.7. DAB mode current peaks for 600 V output voltage operation.

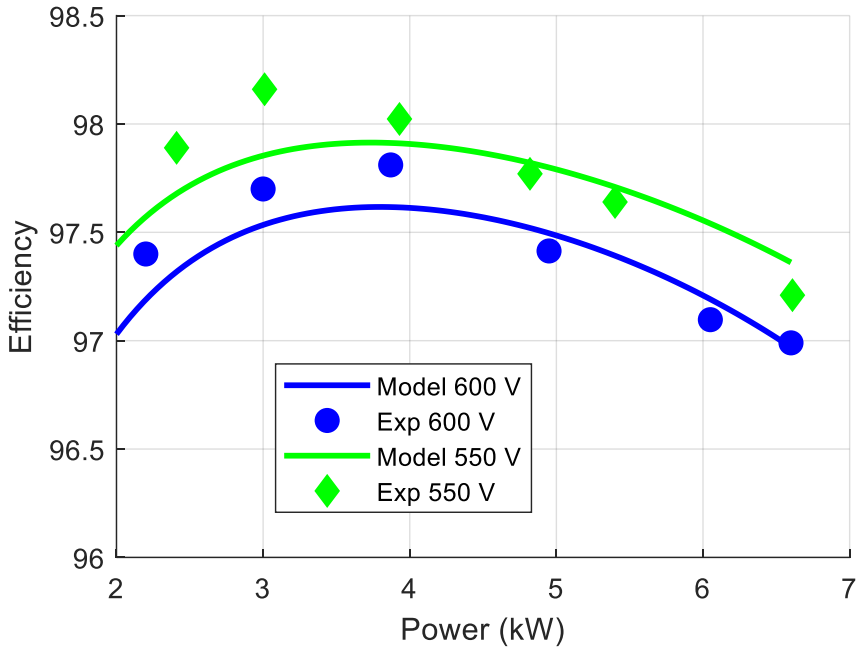

Figure 7.8. Efficiency sweep of the integrated converter in DAB mode.

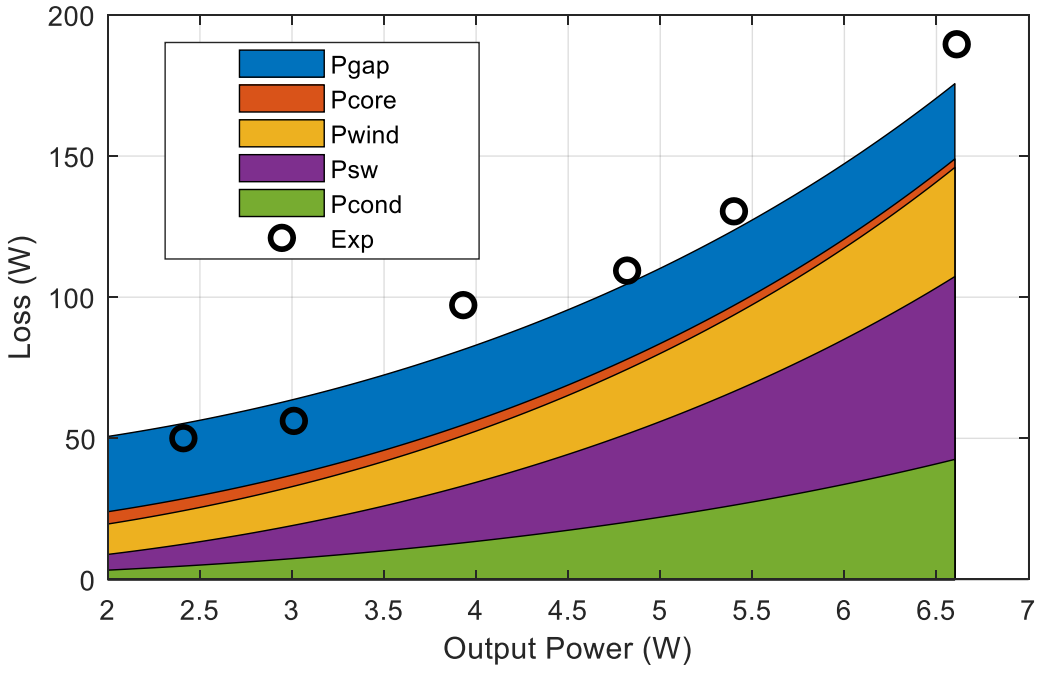

Figure 7.9. Loss breakdown in DAB mode at 600V bus voltage.

The interleaved boost converter is tested up to 20 kW for 400 V to 600 V output voltage. The experimental waveform of the interleaved boost converter operating at 19.83 kW at 600 V output voltage is shown in Figure 7.10. The currents in the interleaved windings are actively controlled to ensure equal current sharing. The efficiency of the integrated converter operating at interleaved boost mode for different output voltage is shown in Figure 7.11. With higher output voltage, the boost efficiency drops due to higher current peaks required for a higher boost ratio. The boost converter efficiency is low at the high voltage light load condition. The loss breakdown of the interleaved boost mode of operation at 600 V output voltage is shown in Figure 7.12. The hard switching loss is the major loss contributor for the interleaved boost converter. The efficiency comparison of the integrated converter operating at boost mode and DAB mode at 600V output voltage is shown in Figure 7.13. Using the online transition algorithm, DAB can improve light load efficiency during the traction operation.

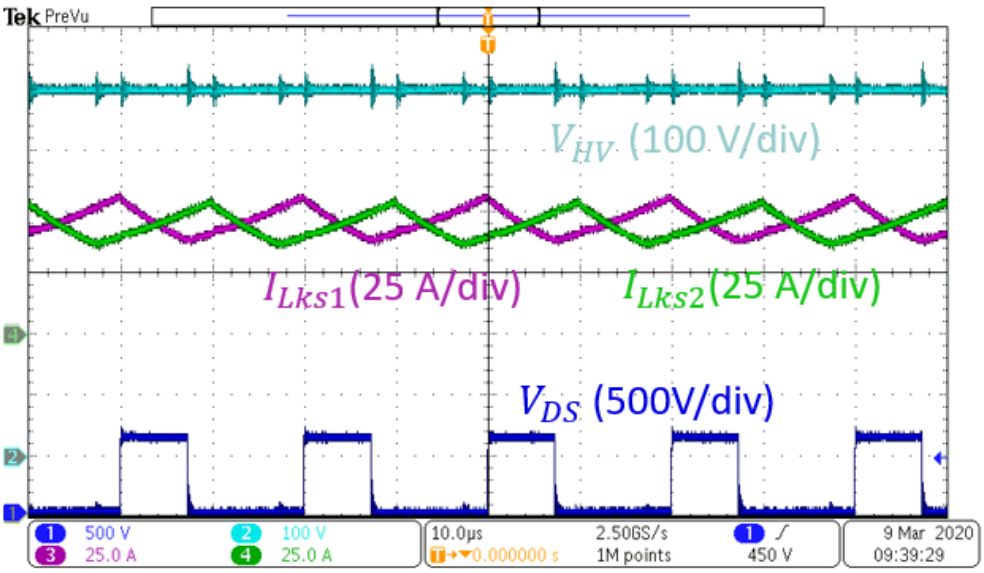

Figure 7.10. Integrated converter operating in interleaved boost mode at 19.83 kW.

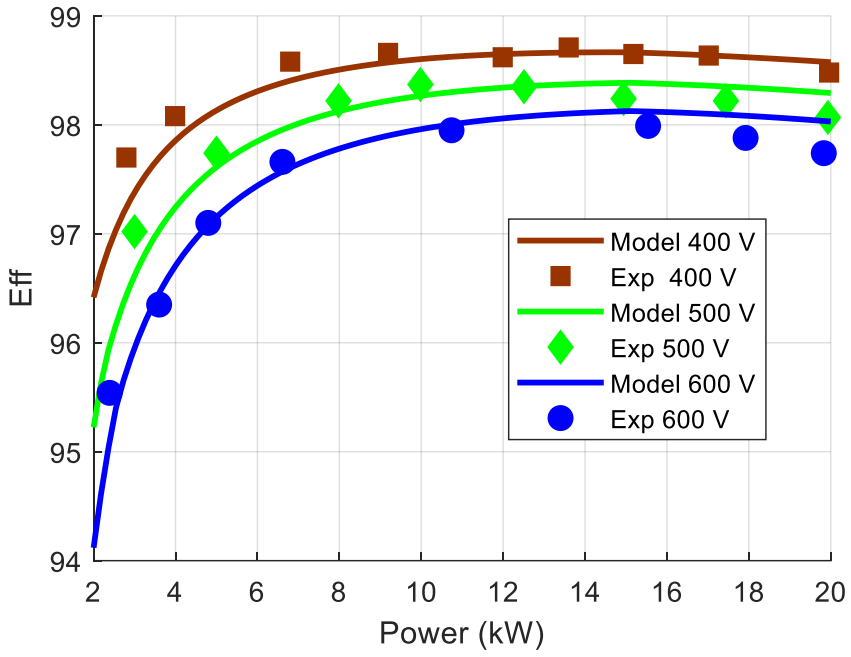

Figure 7.11. Efficiency sweep of the integrated converter in interleaved boost mode.

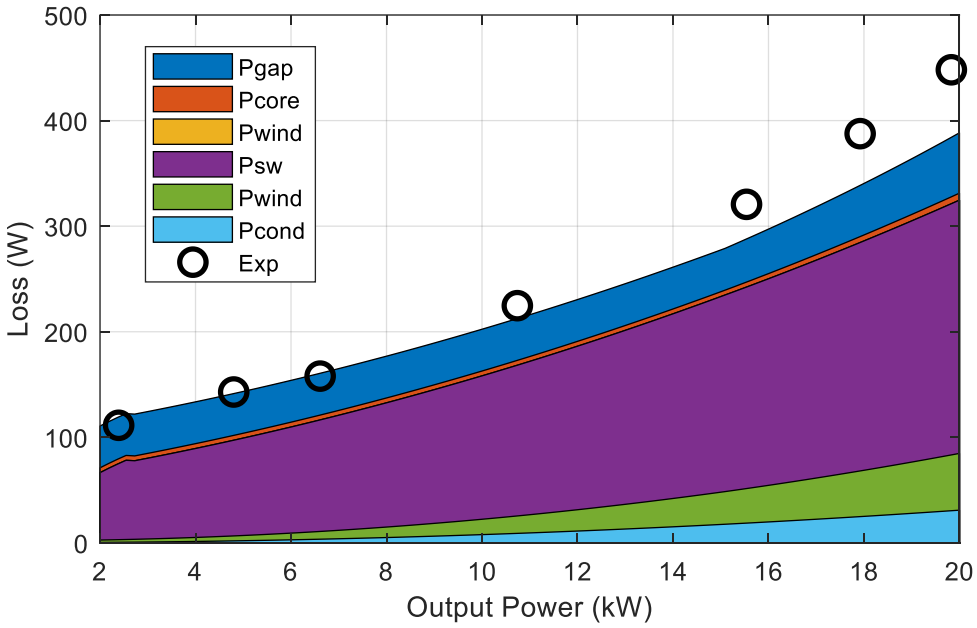

Figure 7.12. Loss breakdown in interleaved boost mode at 600 V output voltage.

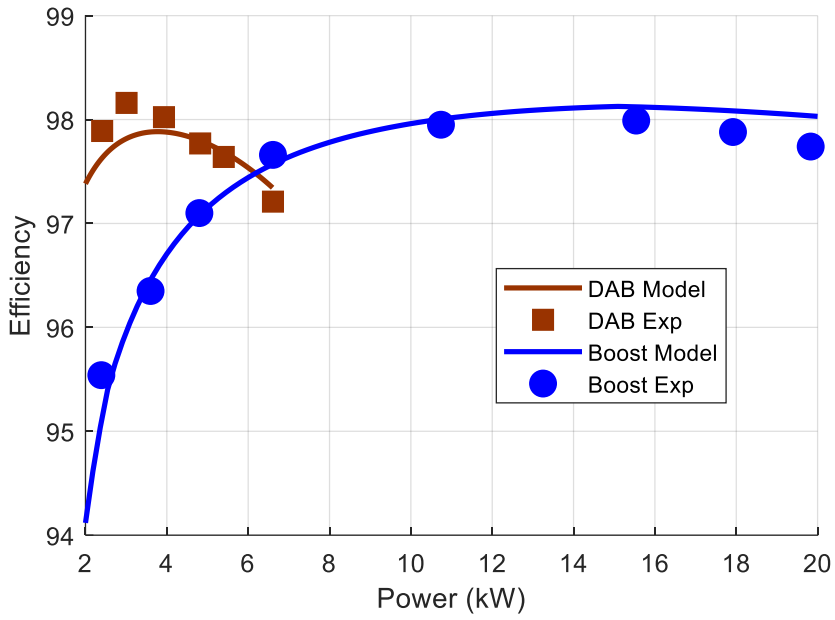

Figure 7.13. Integrated converter efficiency comparison between the interleaved boost mode and DAB mode at 600 V output voltage.

7.2 Closed-Loop Control Implementation

The main objective of the closed-loop controller in the integrated converter is to regulate the output voltage set by the controller in both the interleaved boost and DAB mode. The output torque and speed of the traction motor varies at different inverter input voltage level. The inverter efficiency can be improved by changing the input of inverter bus voltage at different torque and speed demands during the drive cycle as shown in Chapter 6.

The block diagram of the closed-loop controller is shown in Figure 7.14. The controller senses the currents through the interleaved boost windings, the output current, the midpoint voltage of the hybrid transformer, and the output voltage. Based on the output voltage and output current, the controller estimates the output power. Using the efficiency mapping stored in the controller

database, the converter decides whether the converter needs to operate in boost or DAB mode. If a mode transition is required, the controller initiates the online transition between the boost and DAB mode. The objective of the transition is to ensure stable output bus voltage using the closed loop controller. Reduced primary and secondary current oscillation is also ensured by the controller by pre-estimating the current peaks according the integrated converter model developed in Chapter 4. The converter output reference voltage is set by a high-level supervisory controller to minimize the overall traction system loss based on the traction system mapping.

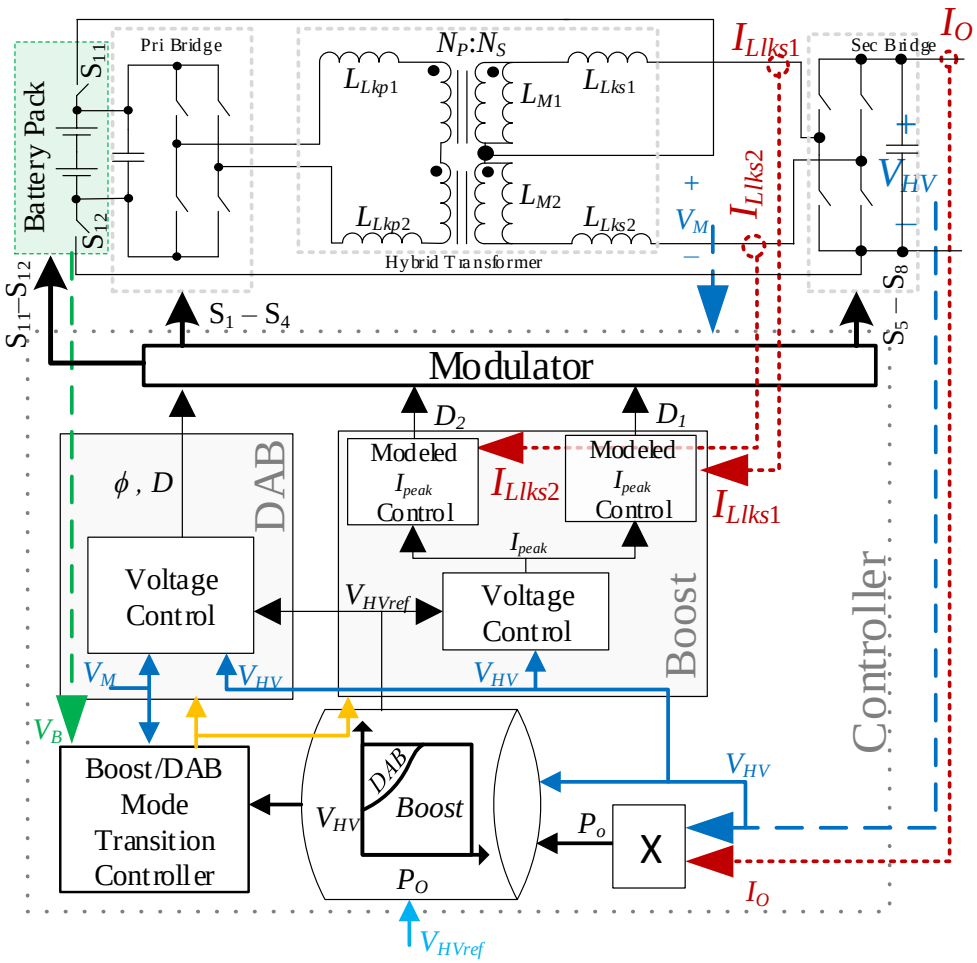

Figure 7.14. Closed-loop control architecture of the integrated converter.

In interleaved boost mode, the role of the controller is to regulate the integrated converter output voltage set by the voltage reference. The output voltage is regulated by adjusting the duty cycle of the interleaved stages. The controller also ensures equal current sharing between the windings of the interleaved stage. To regulate the boost stage duty cycle, a proportional-integral (PI) controller is used to generate the control current reference (i_{peak}) for the interleaved boost stages. Using the hybrid transformer secondary winding current sensors, the periodic average boost current is evaluated. The peak current is then estimated as

$$i_{peakx}[n-1] = i_{avx} + \frac{V_B d_x[n-1]}{2 f_s L_B} \tag{7-1}$$

where x, i_{avx}, f_s, $d_x[n-1]$, and L_B are the phase number, average inductor current, switching frequency of boost mode, previous period cycle duty, and boost inductance respectively. The duty cycle

$$d[n] = \frac{\frac{i_c}{2} - i_{px}[n-1]}{m_c} f_s \tag{7-2}$$

is calculated for each phase using the estimated peak current controller presented in [135, 136]. where m_c represents the slope compensation which is selected as

$$m_c = \frac{V_{HV} - V_B}{L_B} \tag{7-3}$$

The interleaved boost mode without and with the current controller are shown in Figure 7.15. The current is imbalanced between the phases due to imperfect matching between the two boost inductors. Using the current program control, the current is balanced evenly between the two interleaved boost windings. To visualize the dynamics of the interleaved boost converter control

system, the output voltage reference is changed with an 8 V step as shown in Figure 7.16. The voltage reaches steady-state and the phase currents are distributed evenly during the transition. The load step change from 2.5 kW to 4.7 kW is shown in Figure 7.17.

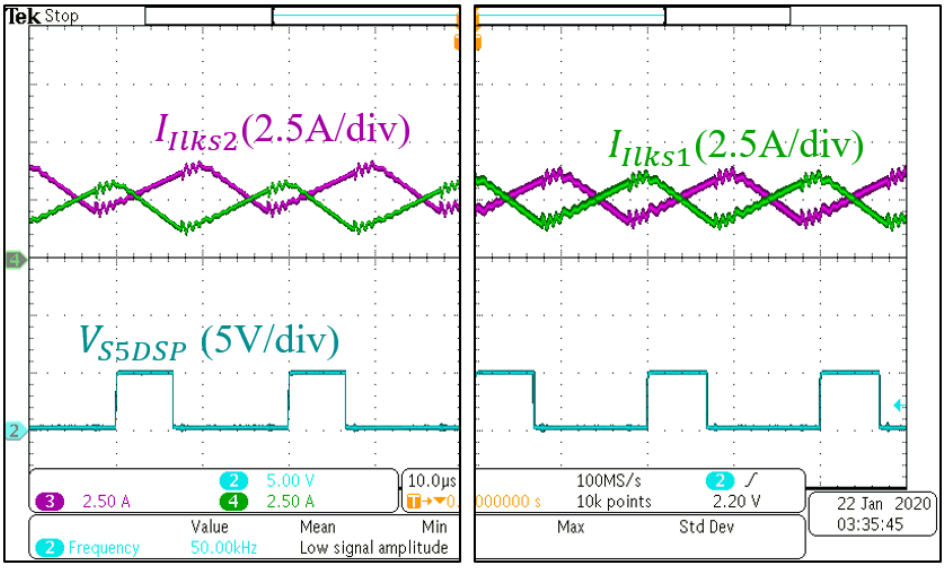

(a) (b)

Figure 7.15. Interleaved boost mode of operation (a) without current control (b) with current control.

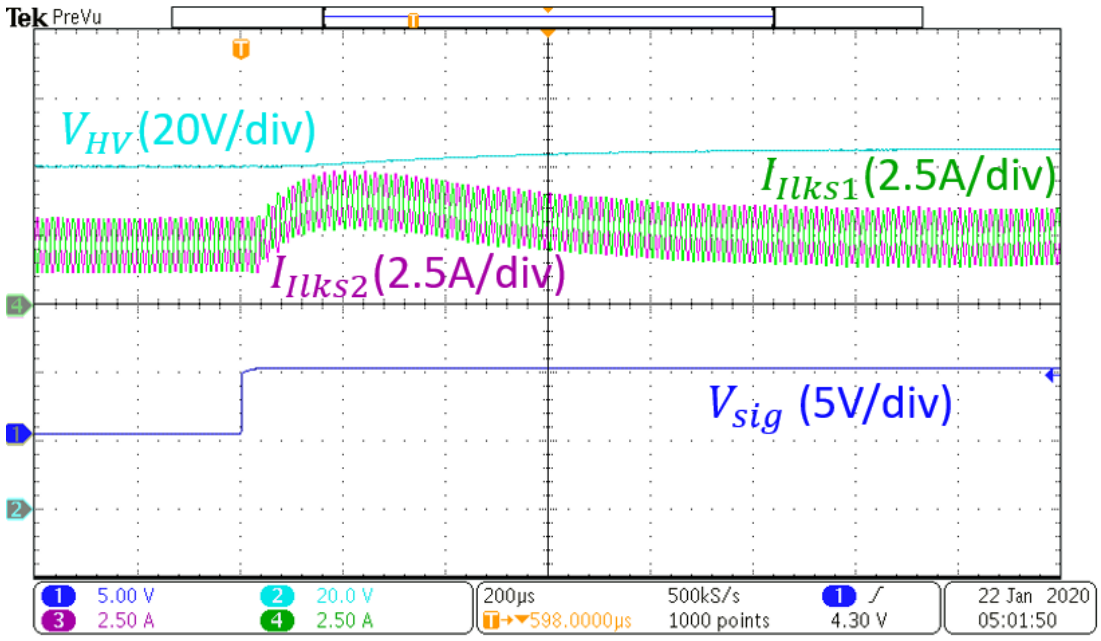

Figure 7.16. The voltage step change of the integrated converter in boost mode.

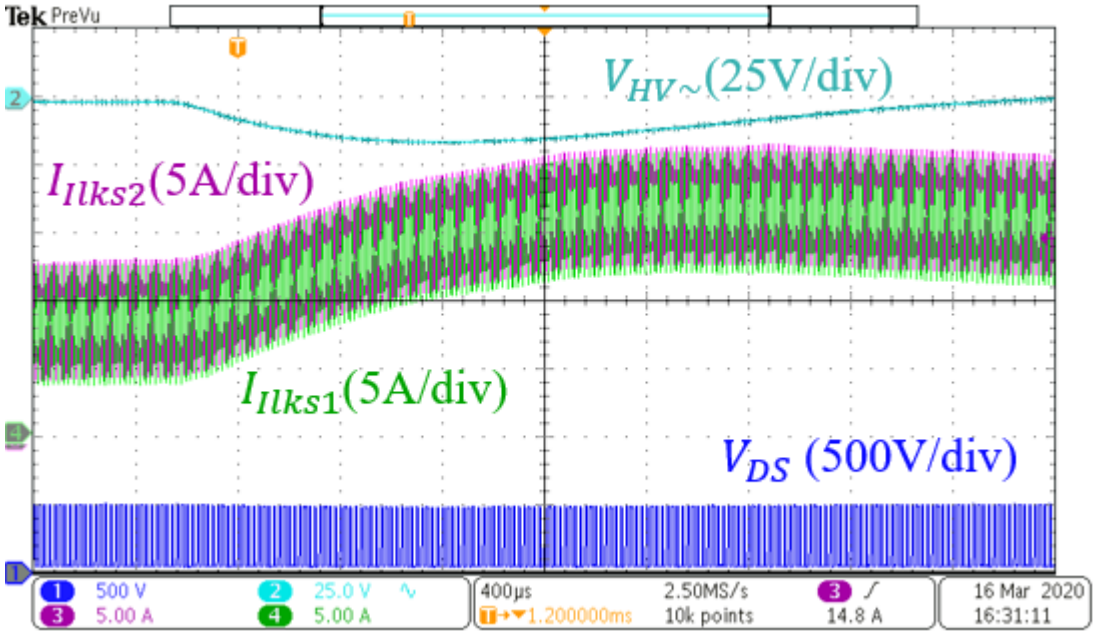

Figure 7.17. Load transient of the integrated converter in the boost mode.

In DAB mode, the controller regulates the output voltage by adjusting the phase shift between the primary and the secondary bridge. The controller also controls the duty of the DAB converter to operate it at the trapezoidal modulation during the transition. Including the impact of the magnetizing inductance during the phase shift control of the DAB mode, the control-to-output voltage transfer function is

$$G_{v\phi}(s) = \frac{nV_B\left(1-\frac{2\varphi}{\pi}\right)R_{load}}{(C_{HV}R_{load}s+1)\left(n^2L_{Lkp}+L_{Lks}+\frac{n^2L_{Lkp}L_{Lks}}{L_M}\right)} \tag{7-4}$$

where n, V_B, φ, R_{load}, C_{HV}, L_{Lkp}, L_{Lks}, and L_M are effective turns ratio, battery voltage, steady-state phase shift, load resistance, output capacitance, primary leakage inductance, secondary leakage inductance, and magnetizing inductance. The DAB is controlled by a PI controller to set the phase shift of the controller based on the reference HV inverter bus voltage obtained from the lookup table. The open-loop response for the integrated converter in DAB mode is given in Figure 7.18.

The output voltage reference is changed with a 10 V step signal. The step response of the DAB converter is shown in Figure 7.19. The load step change in DAB mode from 2.5 kW to 4.7 kW is shown in Figure 7.20.

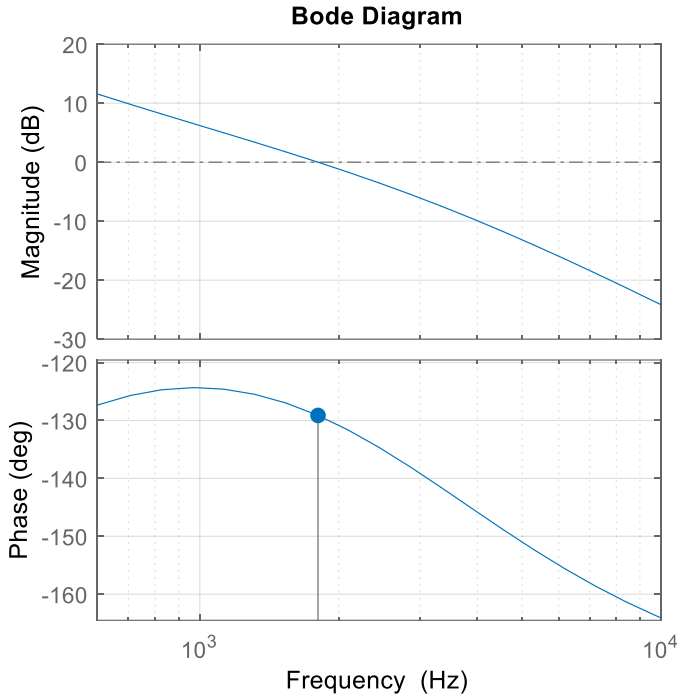

Figure 7.18. Open-loop response of the integrated converter in DAB mode.

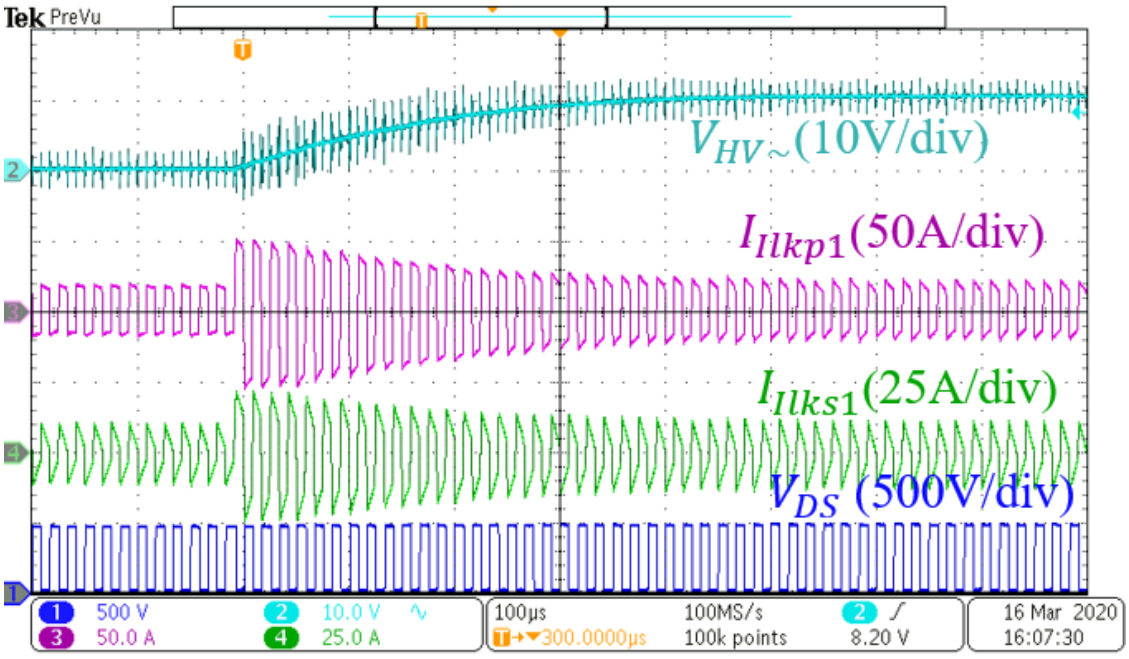

Figure 7.19. The voltage step change of the integrated converter in DAB mode.

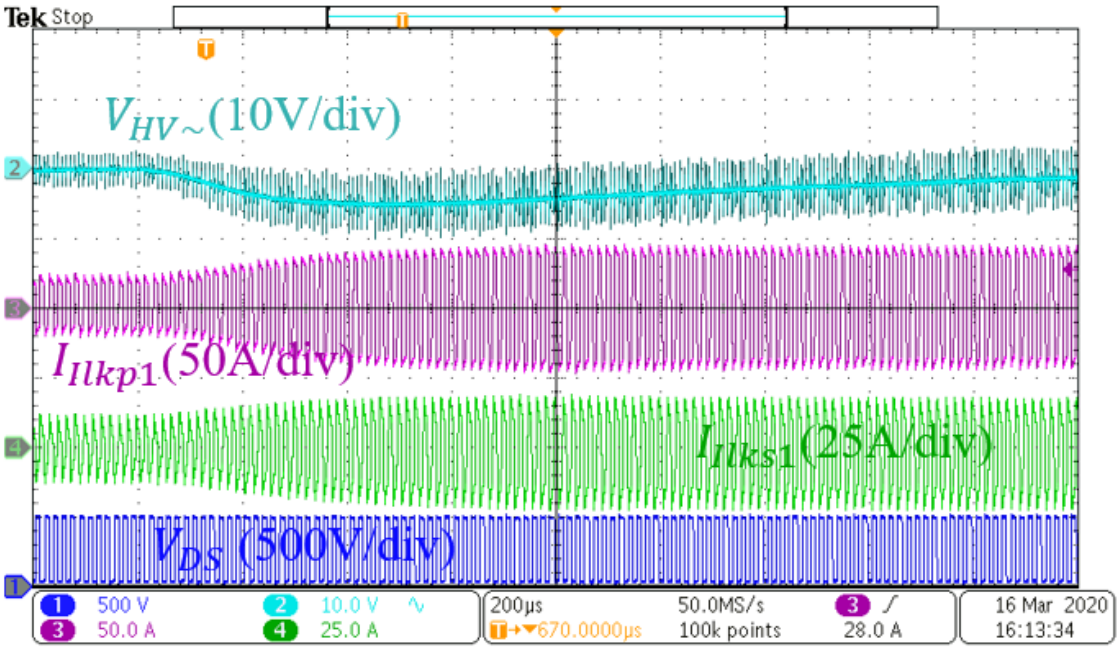

Figure 7.20. Load transient of the integrated converter in the DAB mode.

7.3 Online Mode Transition

Based on the efficiency mapping, the controller will automatically select the operating mode and output voltage to improve the overall traction efficiency. To improve the light load efficiency of the integrated converter, an online transition from boost to DAB mode is performed at a regulated output voltage as described in Chapter 5. The controller objective during the transition is to ensure stable output voltage without sag or swell, seamless power flow, and reduced current oscillation during the transition.

The online transition from boost to DAB mode at 3 kW at 600 V bus voltage is shown in Figure 7.21. The boost to DAB transition time is estimated at around 8.4 ms. At the onset of the boost to DAB transition, the interleaved boost currents are reduced to zero as shown in Figure 7.22. After four switching cycles, the DAB mode is initiated using trapezoidal modulation. The duty of

the trapezoidal modulation is regulated by the controller to ensure zero voltage across the BMS contactor S_{11}. The startup process of the DAB mode is performed without any voltage and current oscillation. The BMS contractor is disconnected during the trapezoidal modulation since the current is diverted from the BMS contractor to the hybrid transformer. The transition from trapezoidal modulation to phase modulation is performed after 8.4 ms as shown in Figure 7.23. The phase shift modulation provides lower loss since the current peaks are reduced. The transition from trapezoidal modulation to phase shift modulation in DAB mode is performed without any current and voltage oscillation.

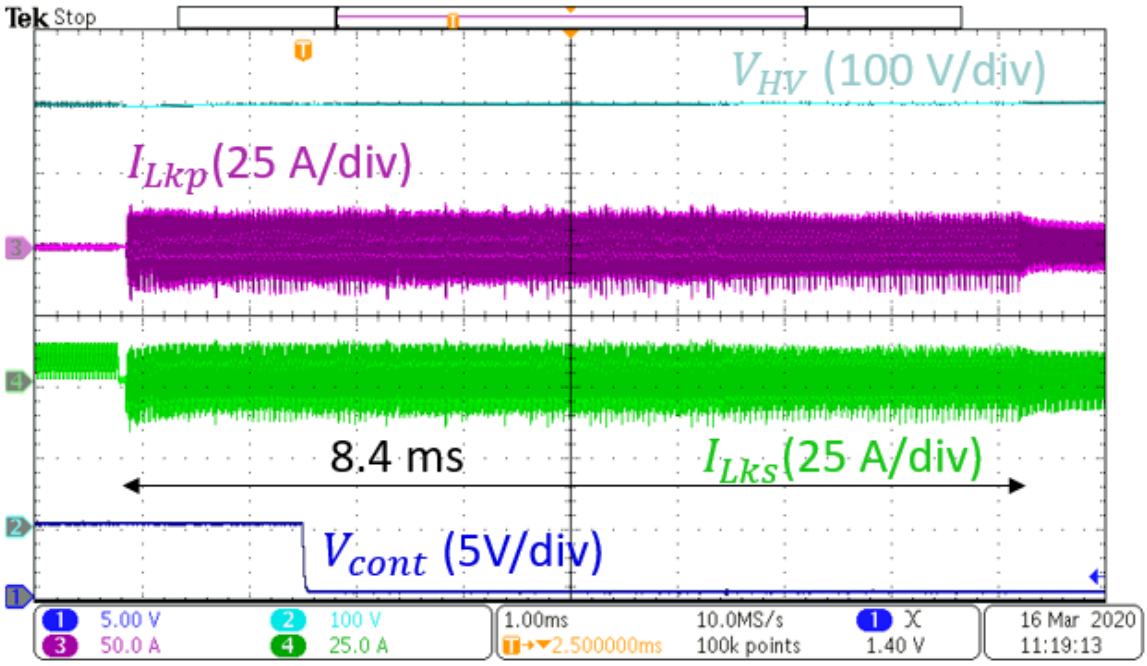

Figure 7.21. Boost mode to DAB mode transition at 3 kW.

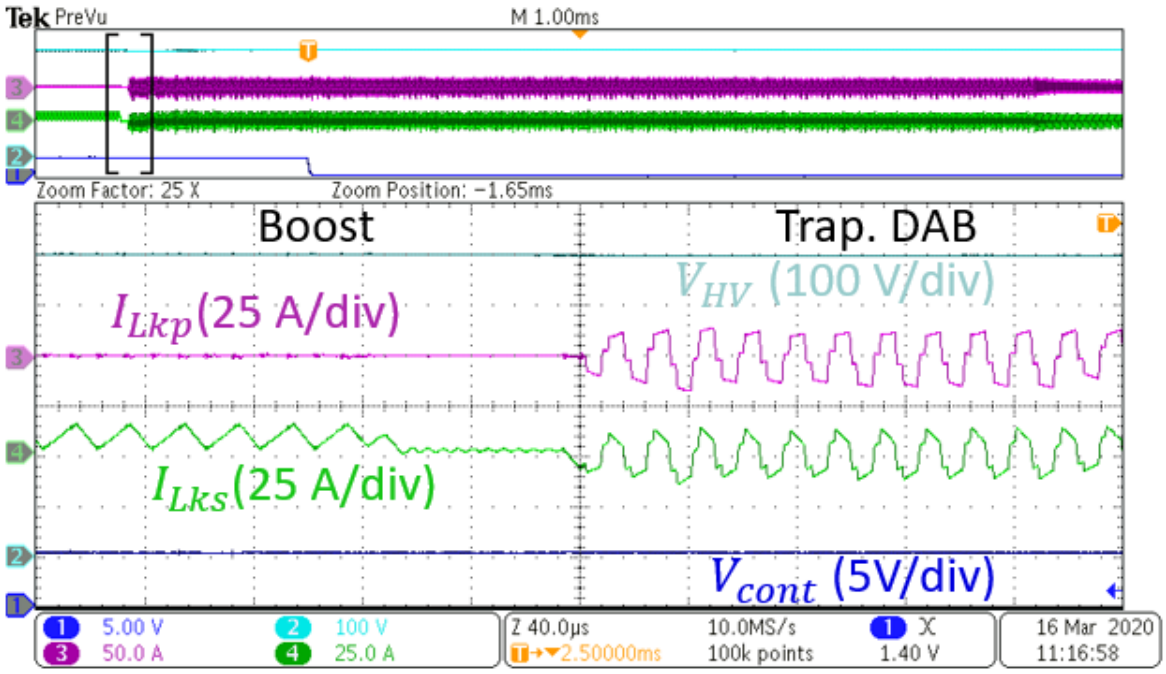

Figure 7.22. Boost to Trapezoidal DAB transition at 3 kW.

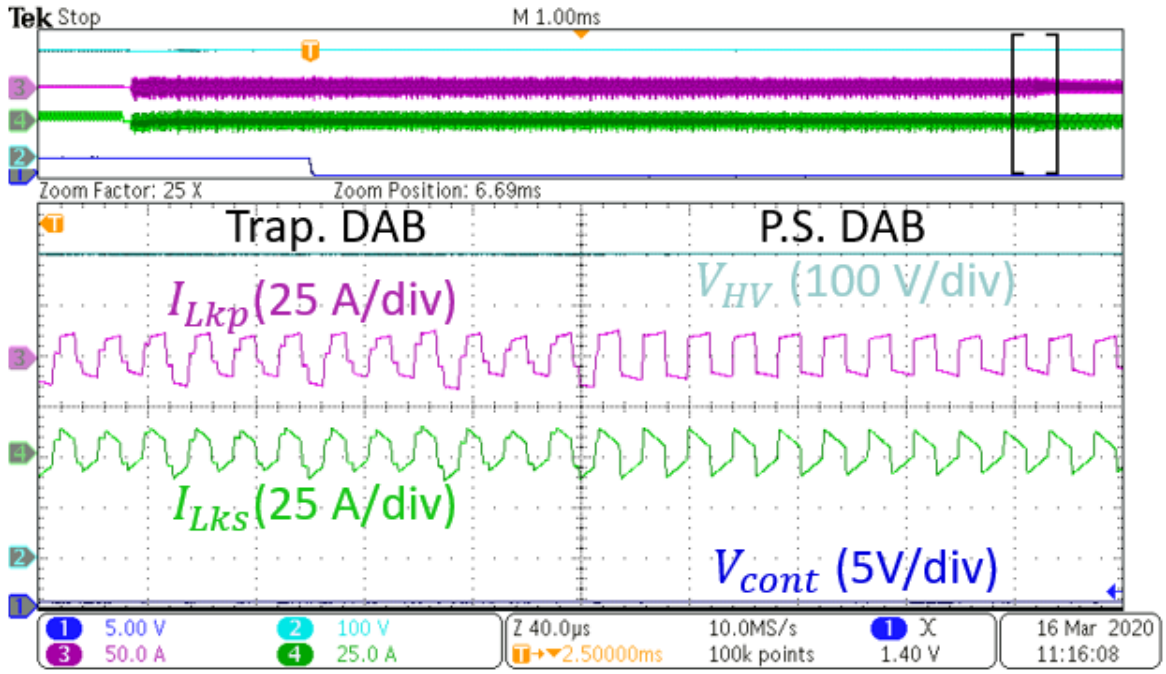

Figure 7.23. Trapezoidal DAB to phase shift DAB transition at 3 kW.

Once the integrated converter power demand exceeds 6.6 kW, the converter makes the transition from DAB mode to boost mode. The online transition from DAB to Boost mode at 7 kW is presented in Figure 7.24. The total transition time is estimated at around 20 ms. At the onset of the transition, the BMS contactor signal is turned on and the DAB modulation is changed from phase shift modulation to trapezoidal modulation as shown in Figure 7.25. The duty of the trapezoidal modulation is controlled by the controller to ensure the voltage across the BMS contactor S_{11}. After the BMS contactor connection time and bouncing time, the transition from DAB to boost mode is performed as shown in Figure 7.26. The inductor current is ramped up to the modeled peak steady-state boost current to charge the output capacitor and reduce the current oscillation. In this way, the soft start of the Boost mode is ensured for any power and voltage level.

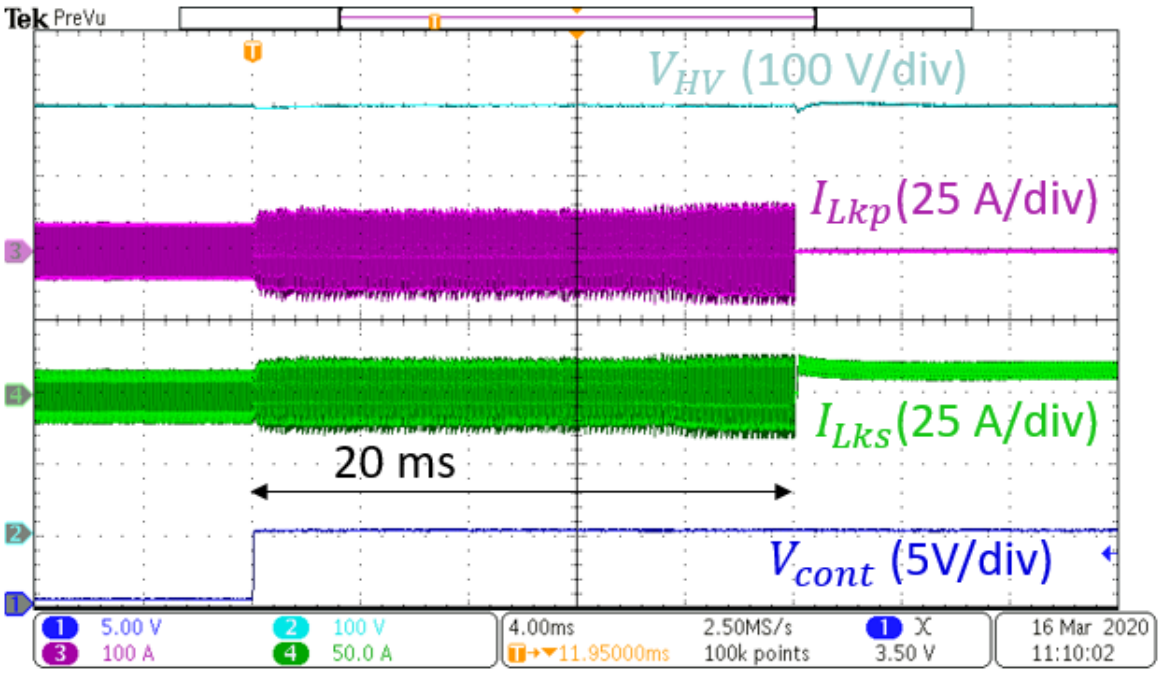

Figure 7.24. DAB mode to interleaved Boost mode transition at 7 kW.

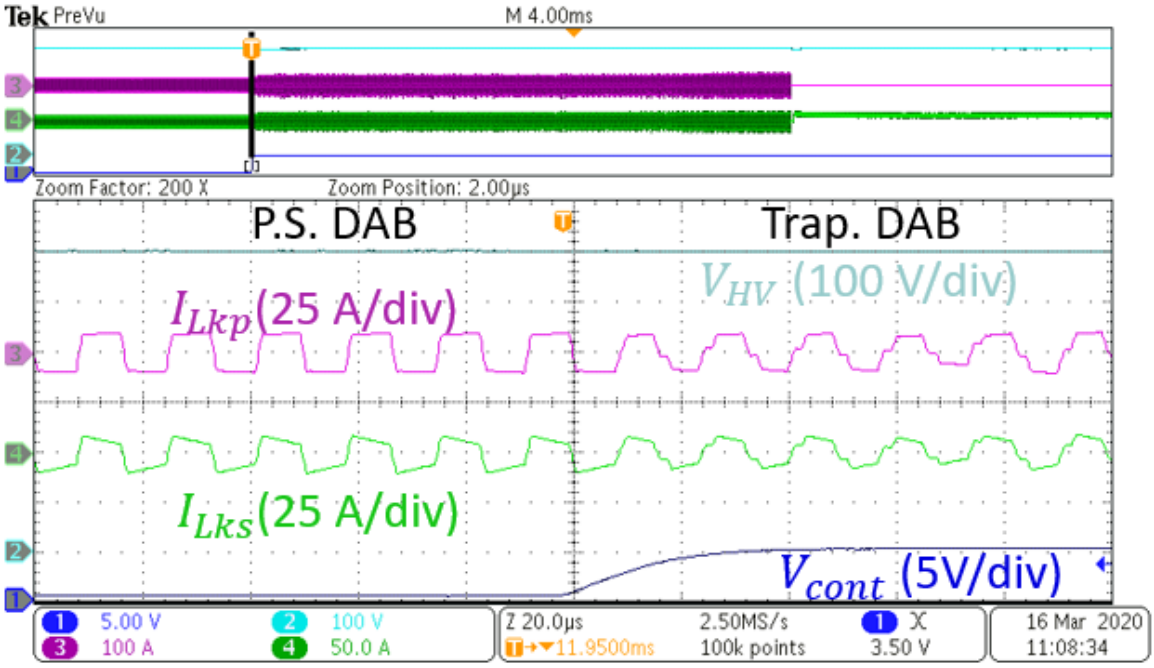

Figure 7.25. Phase shift to trapezoidal DAB at 7 kW.

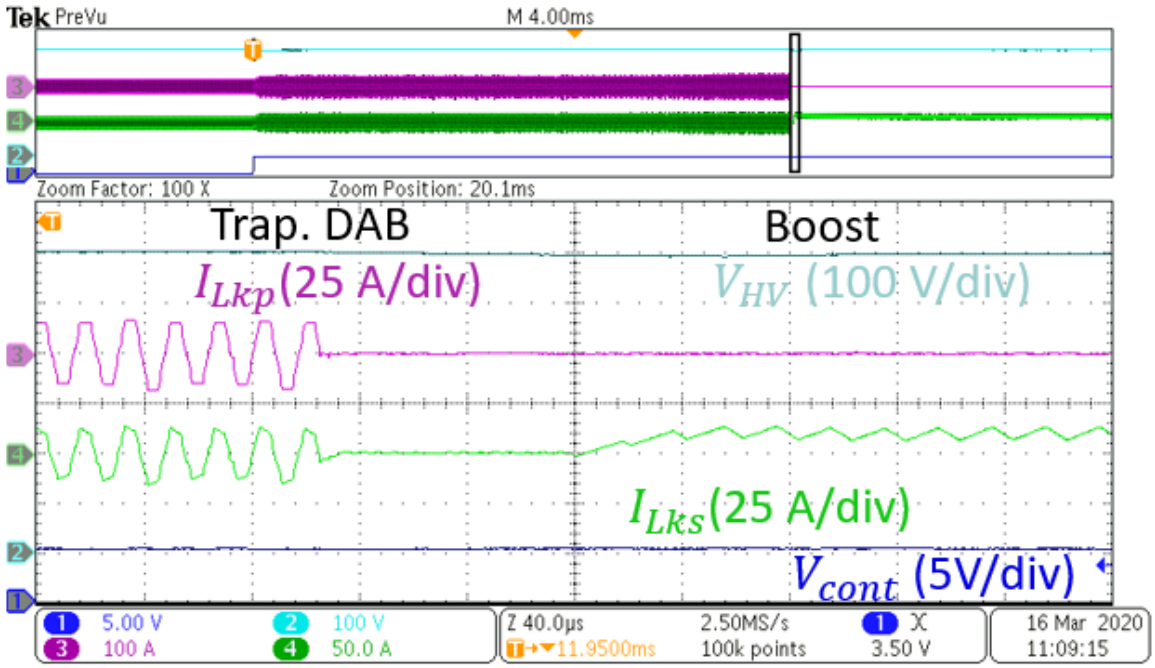

Figure 7.26. Trapezoidal DAB to Boost transition at 7 kW.

During the drive cycle, the integrated converter power demand varies for different torque and speed requirements. The operation of the integrated converter in a drive cycle is presented in Figure 7.27. The converter is started using a soft start of the output voltage controller and constant current load. The output load is then programmed to change after 30 seconds to emulate the drive cycle scenario. Based on the sensed output power and the look-up table implemented in the DSP, the converter automatically selects the operating modes and output voltage reference. After the output voltage is set, the controller evaluates which operating modes provide better efficiency. The mode transition controller initiates the transition to improve the overall traction efficiency at different points of the drive cycle.

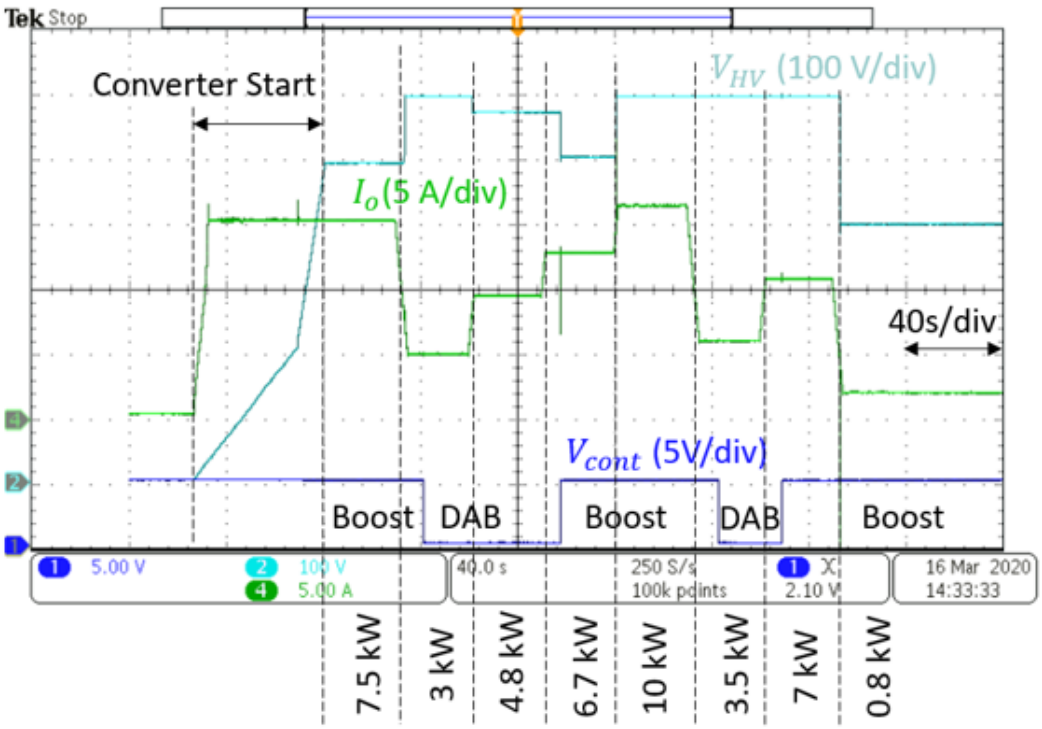

Figure 7.27. Integrated converter operation during the drive cycle.

The proposed integrated converter performance is shown in Figure 7.28. The performance is compared in terms of peak traction DC-DC efficiency and the maximum power over the total core weight. The aim is to design towards the top-right region which exhibits higher efficiency and lower core weight. Compared with other integrated converter solutions in the literature, the proposed integrated converter improved the converter efficiency and output power to core weight ratio simultaneously. The core weight of DC-DC stage of Level 2 OBC is also added to the separate traction DC-DC stage for comparison. Compared with separated DC-DC traction power converter solutions, the proposed integrated converter also exhibits good efficiency and output power to total core weight ratio.

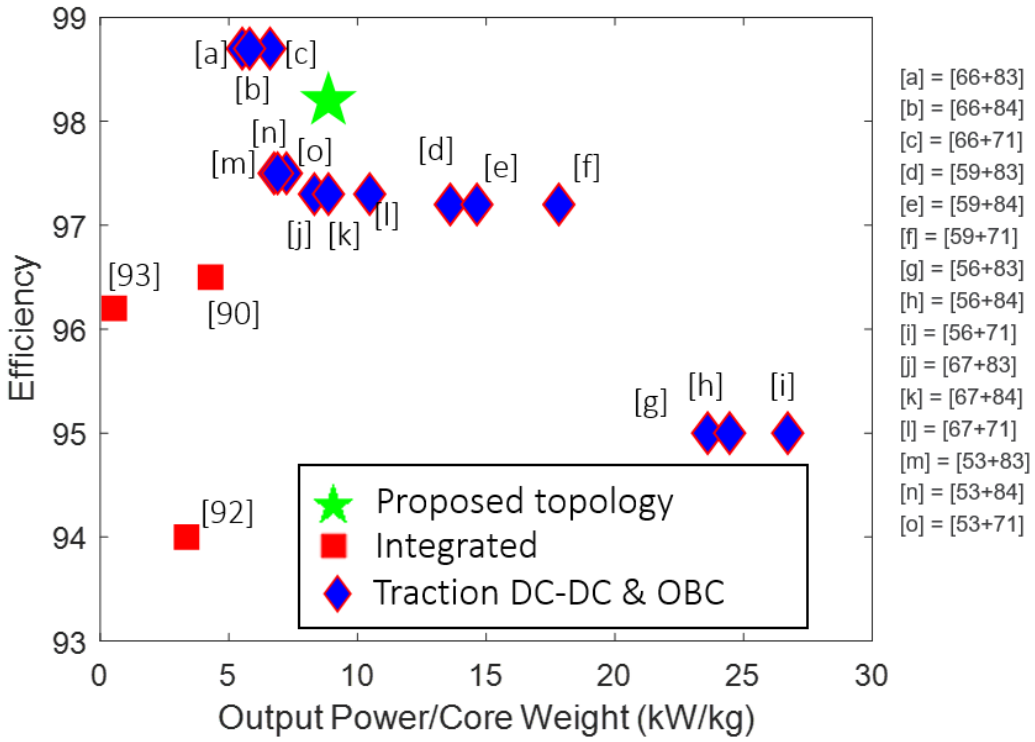

Figure 7.28. Comparison of proposed integrated converter efficiency and output power/core weight.

7.4 Summary

In this chapter, a 20 kW integrated converter prototype is developed to demonstrate the integrated converter operation in different modes. The integrated converter model is validated for different voltage and power levels. A closed-loop controller is developed to regulate the output voltage in both boost mode and DAB mode. The controller is responsible for the automatic transition between modes, ensuring a smooth transition between modes. The closed-loop converter is also responsible for sharing the boost phase currents equally between the hybrid transformer. Finally, the converter is tested for a drive cycle to demonstrate the automated voltage transition and voltage reference selection capabilities.

8 Conclusions and Future Work

The major takeaways of the integrated converter research are highlighted in this chapter. The future works of the research are also presented in this chapter.

8.1 Conclusion

The design methodology of an integrated DC-DC converter is presented in this dissertation. The major research contributions are concluded as follows.

First, a new integrated DC-DC converter topology is proposed to combine the functionality of traction boost converter and DAB converter of OBC using a hybrid transformer. The design process of the hybrid transformer is investigated. the DAB model including the effect of magnetizing inductance is investigated. In conventional DAB, the transformer airgap is significantly smaller than the hybrid transformer. As a result, the primary and secondary current waveform has similar waveshape in conventional DAB. The primary, secondary and magnetizing currents in the hybrid transformer in DAB mode are modeled for loss evaluation and design optimization. Although the higher current peaks in the hybrid transformer increase the RMS currents, the higher magnetizing current extends the ZVS range of the DAB converter. The current peaks are also validated using the experimental results.

Second, a method is developed to model the loss associated with air gap and fringe flux in FEMM 2D finite element analysis tool. The primary and secondary winding arrangement in the hybrid transformer is considered for loss evaluation. The gap loss model improves the analytical gap loss prediction for the hybrid converter operating in DAB mode.

Third, an online transition algorithm is developed for the seamless transition between the boost and DAB modes to improve the traction efficiency. The online transition is essential for the

integrated DC-DC converter leveraging the existing BMS contactors are reconfiguration switches. The main objective of the online transition is to ensure constant DC output voltage of the integrated converter and eliminate power flow interruption during the mode transition. The transition algorithm ensures zero current through the BMS contactor during disconnecting and zero voltage across the BMS contractor during connecting. A trapezoidal modulation for DAB mode is proposed where the duty of the secondary bridge is set online based on the battery voltage and operating output voltage. During the mode change, a soft start is also essential to prevent current and voltage oscillation. The soft-start is achieved by using the current peaks modeled for the hybrid transformer.

Fourth, a Pareto front optimization is developed to improve the integrated converter design for all aspects including weight, price, and traction loss. An aggregated drive cycle is considered for design optimization which includes both city and highway driving conditions. The converter price and weight model are also developed. A dataset of primary devices, secondary power modules, and nanocrystalline cores are chosen for the integrated converter design. Different converter operating parameters including switching frequency, ripple, and hybrid transformer fill factor is considered. the optimization improves the integrated converter design to reduce traction energy loss, converter weight, and price. Compared with separate boost and DAB converter solution, the integrated converter reduced DC-DC stage energy loss by 8%, weight by 12%, and price by 9%. A 20 kW prototype is developed based on the optimization results.

Fifth, an automated controller is developed for the integrated converter that can control the integrated converter transition between the boost and the DAB mode by automatically sensing the output power and using the lookup table implemented in the DSP. During the automated transition, the converter regulates the output voltage and resets the operating mode switching frequency

online. The controller operation at different power levels is demonstrated as well where the controller changed the inverter bus voltage based to achieve the best efficiency during the traction operation.

8.2 Future Work

The possible future works of the integrated converter are given below:

8.2.1 Unified Hybrid Transformer

In this study, two separate core pairs are used for the hybrid transformer design. The hybrid transformer design can be further integrated by combining the core pairs. In this way, the core weight, volume, and price can be reduced further. A custom core is required to optimize the unified hybrid transformer design. The main challenge of this approach is to optimize the core width and length. Using finite element analysis software, the leakage inductance for the DAB operation can be varied by optimizing the custom core geometry.

8.2.2 Variable Frequency DAB Operation

The switching frequency of the DAB converter is kept constant in this research for the integrated converter operation. However, operating the DAB at different switching frequencies during different power levels of the traction operation can improve the light load efficiency further. The design optimization for the variable frequency DAB operation is also challenging since an inner optimization loop is required to identify the DAB frequency profile for a given drive cycle.

8.2.3 Battery Voltage Variation

The battery voltage of the integrated converter is kept constant for the integrated converter design. In EVs, the input voltage will change with the state of the charge of the battery. The battery

voltage state of the charge reduction with the advancement of the drive cycle can provide more practical results. The battery voltage variation can be used as an optimization variable as well to identify the integrated converter loss as well. From the total energy requirement and the battery state of the charge specification, the battery pack size required for a certain vehicle can be optimized as well.

Reference

[1] A. Poullikkas, "Sustainable options for electric vehicle technologies," *Renewable and Sustainable Energy Reviews,* vol. 41, no. 0, pp. 1277-1287, 2015.

[2] Z. L. Shiqi Ou, Zhixin Wu, Jihu Zheng, Renzhi Lyu, Steven Przesmitzki, Xin He, "A Study of China's Explosive Growth in the Plug-in Electric Vehicle Market," Oak Ridge National Laboratory, 2017. [Online]. Available: https://info.ornl.gov/sites/publications/files/Pub72210.pdf

[3] "Fast Fact U.S. Transportation Sector Greenhouse Gas Emissions " https://www.epa.gov/sites/production/files/2018-06/documents/420f18013.pdf.

[4] "24 Factors That Will Affect the Rate of EV Adoption " http://evadoption.com/24-factors-that-will-affect-the-rate-of-ev-adoption-part-1/.

[5] I. Subotic, N. Bodo, E. Levi, and M. Jones, "Onboard Integrated Battery Charger for EVs Using an Asymmetrical Nine-Phase Machine," *Industrial Electronics, IEEE Transactions on,* vol. 62, no. 5, pp. 3285-3295, 2015.

[6] C. Giles, C. Ryder, and S. Lommele. "Workplace Charging: Charging Up University Campuses." https://afdc.energy.gov/files/u/publication/wpc_charging_university_campuses.pdf.

[7] B. A. Welchko, "Analytical calculation of the RMS current stress on the DC link capacitor for a VSI employing reduced common mode voltage PWM," *2007 European Conference on Power Electronics and Applications, Vols 1-10,* pp. 2232-2239, 2007.

[8] "Timeline: History of the Electric Car." https://www.energy.gov/articles/history-electric-car.

[9] "EV Sales and Gasoline Price." http://www.anl.gov/sites/anl.gov/files/evsales_fig5_8-16.jpg.

[10] http://www.21stcentech.com/electric-vehicles-35-car-sales-globally-2040/.

[11] "Electrical and Electronics Technical Team Roadmap." https://www.energy.gov/sites/prod/files/2017/11/f39/EETT%20Roadmap%2010-27-17.pdf.

[12] 2013. "EV Everywhere Grand Challenge Blueprint." https://www.energy.gov/sites/prod/files/2014/02/f8/eveverywhere_blueprint.pdf.

[13] T. A. Burress *et al.*, "EVALUATION OF THE 2010 TOYOTA PRIUS HYBRID SYNERGY DRIVE SYSTEM," 2011. [Online]. Available: https://info.ornl.gov/sites/publications/files/pub26762.pdf

[14] A. Emadi, Y. J. Lee, and K. Rajashekara, "Power Electronics and Motor Drives in Electric, Hybrid Electric, and Plug-In Hybrid Electric Vehicles," *IEEE Transactions on Industrial Electronics,* vol. 55, no. 6, pp. 2237-2245, 2008.

[15] F. Krismer and J. W. Kolar, "Efficiency-Optimized High-Current Dual Active Bridge Converter for Automotive Applications," *IEEE Transactions on Industrial Electronics,* vol. 59, no. 7, pp. 2745-2760, 2012.

[16] W. Dong-Gyun, K. Yun-Sung, and L. Byoung-Kuk, "Effect of PWM schemes on integrated battery charger for plug-in hybrid electric vehicles: Performance, power factor, and

efficiency," in *IEEE Applied Power Electronics Conference and Exposition*, 16-20 March 2014 2014, pp. 3243-3248.

[17] "Electric Vehicle Architectures." http://evsummit.org/speakers/presentations/2016/Workshop_Powertrain_Qin.pdf.

[18] "ELECTRIC DRIVE STATUS AND CHALLENGES." https://www1.eere.energy.gov/vehiclesandfuels/pdfs/ev_everywhere/4_rogers_ed.pdf.

[19] "Electric traction inverter (HEV/EV)." https://www.danfoss.com/en/markets/automotive/dsp/electric-traction-inverter-hevev/#tab-overview.

[20] T. Burress. "Benchmarking EV and HEV Technologies." https://www.energy.gov/sites/prod/files/2016/06/f32/edt006_burress_2016_o_web.pdf.

[21] X. Jing, B. A. Welchko, C. Stancu, and P. J. Savagian, "Control strategies for a high frequency DC-DC converter for electrified vehicles," in *2017 IEEE Energy Conversion Congress and Exposition (ECCE)*, 1-5 Oct. 2017 2017, pp. 558-565.

[22] T. Burress. "Benchmarking State-of-the-Art Technologies." https://www.energy.gov/sites/prod/files/2014/03/f13/ape006_burress_2013_o.pdf.

[23] K. Hamada, M. Nagao, M. Ajioka, and F. Kawai, "SiC—Emerging Power Device Technology for Next-Generation Electrically Powered Environmentally Friendly Vehicles," *IEEE Transactions on Electron Devices,* vol. 62, no. 2, pp. 278-285, 2015.

[24] J. A. Baxter, D. A. Merced, D. J. Costinett, L. M. Tolbert, and B. Ozpineci, "Review of Electrical Architectures and Power Requirements for Automated Vehicles," in *2018 IEEE Transportation Electrification Conference and Expo (ITEC)*, 13-15 June 2018 2018, pp. 944-949.

[25] M. Yilmaz and P. T. Krein, "Review of Battery Charger Topologies, Charging Power Levels, and Infrastructure for Plug-In Electric and Hybrid Vehicles," *Power Electronics, IEEE Transactions on,* vol. 28, no. 5, pp. 2151-2169, 2013.

[26] T. Burress. "Benchmarking EV and HEV Technologies " https://www.energy.gov/sites/prod/files/2014/07/f17/ape006_burress_2014_p.pdf.

[27] I. Subotic and E. Levi, "A Review of Single-Phase On-Board Integrated Battery Charging Topologies for Electric Vehicles," *2015 Ieee Workshop on Electrical Machines Design, Control and Diagnosis (Wemdcd),* pp. 136-145, 2015.

[28] J. C. Gomez and M. M. Morcos, "Impact of EV battery chargers on the power quality of distribution systems," *IEEE Transactions on Power Delivery,* vol. 18, no. 3, pp. 975-981, 2003.

[29] *Standard for Electric Vehicle (EV) Charging System Equipment*, UL, 2009. [Online]. Available: https://standardscatalog.ul.com/standards/en/standard_2202_2

[30] "Overview of the DOE Advanced Power Electronics and Electric Motor R&D Program." https://www.energy.gov/sites/prod/files/2014/09/f18/fy_2014_vto_amr_apeem_overview-final_version.pdf.

[31] "Benchmarking EV and HEV Technologies " https://www.energy.gov/sites/prod/files/2014/07/f17/ape006_burress_2014_p.pdf.

[32] T. A. Burress *et al.*, "EVALUATION OF THE 2008 LEXUS LS 600H HYBRID SYNERGY DRIVE SYSTEM," 2009.

[33] C. Whaling. "Electric Drive Power Electronics: An Overview." https://tec.ieee.org/newsletter/december-2013/electric-drive-power-electronics-an-overview.

[34] "Tesla - Model S." https://www.tesla.com/models/design.

[35] G. Li *et al.*, "A simplified IGBT behavioral model with a tail current module for switching losses estimation," in *2017 IEEE 18th Workshop on Control and Modeling for Power Electronics (COMPEL)*, 9-12 July 2017 2017, pp. 1-6.

[36] K. B. S. Narumanchi, D. DeVoto, G. Moreno, J. Rugh, and S. Waye "Advanced Power Electronics and Electric Motors Annual Report," 2013. [Online]. Available: https://www.nrel.gov/docs/fy15osti/60621.pdf

[37] M. März, A. Schletz, B. Eckardt, S. Egelkraut, and H. Rauh, "Power electronics system integration for electric and hybrid vehicles," in *2010 6th International Conference on Integrated Power Electronics Systems*, 16-18 March 2010 2010, pp. 1-10.

[38] M. Yilmaz and P. T. Krein, "Review of integrated charging methods for plug-in electric and hybrid vehicles," in *Vehicular Electronics and Safety (ICVES), 2012 IEEE International Conference on*, 24-27 July 2012 2012, pp. 346-351.

[39] D. Han, S. Li, W. Lee, and B. Sarlioglu, "Adoption of wide bandgap technology in hybrid/electric vehicles-opportunities and challenges," in *2017 IEEE Transportation Electrification Conference and Expo (ITEC)*, 22-24 June 2017 2017, pp. 561-566.

[40] A. Albanna, A. Malburg, M. Anwar, A. Guta, and N. Tiwari, "Performance comparison and device analysis Between Si IGBT and SiC MOSFET," in *2016 IEEE Transportation Electrification Conference and Expo (ITEC)*, 27-29 June 2016 2016, pp. 1-6.

[41] M. N. Yoder, "Wide bandgap semiconductor materials and devices," *IEEE Transactions on Electron Devices,* vol. 43, no. 10, pp. 1633-1636, 1996.

[42] D. Han, J. Noppakunkajorn, and B. Sarlioglu, "Comprehensive Efficiency, Weight, and Volume Comparison of SiC- and Si-Based Bidirectional DC–DC Converters for Hybrid Electric Vehicles," *IEEE Transactions on Vehicular Technology,* vol. 63, no. 7, pp. 3001-3010, 2014.

[43] Y. Wang, S. W. H. d. Haan, and J. A. Ferreira, "Optimal operating ranges of three modulation methods in dual active bridge converters," in *2009 IEEE 6th International Power Electronics and Motion Control Conference*, 17-20 May 2009 2009, pp. 1397-1401.

[44] Q. Tian *et al.*, "A novel energy balanced variable frequency control for input-series-output-parallel modular EV fast charging stations," in *2016 IEEE Energy Conversion Congress and Exposition (ECCE)*, 18-22 Sept. 2016 2016, pp. 1-6.

[45] A. Garcia-Bediaga, I. Villar, A. Rujas, L. Mir, and A. Rufer, "Multiobjective Optimization of Medium-Frequency Transformers for Isolated Soft-Switching Converters Using a

Genetic Algorithm," *IEEE Transactions on Power Electronics,* vol. 32, no. 4, pp. 2995-3006, 2017.

[46] D. Tran, S. Chakraborty, Y. Lan, J. Van Mierlo, and O. Hegazy, "Optimized Multiport DC/DC Converter for Vehicle Drivetrains: Topology and Design Optimization," *Applied Sciences,* vol. 8, no. 8, 2018.

[47] U. Badstuebner, J. Biela, D. Christen, and J. W. Kolar, "Optimization of a 5-kW Telecom Phase-Shift DC–DC Converter With Magnetically Integrated Current Doubler," *IEEE Transactions on Industrial Electronics,* vol. 58, no. 10, pp. 4736-4745, 2011.

[48] H. Kim, H. Chen, D. Maksimović, and R. Erickson, "Boost composite converter design based on drive cycle weighted losses in electric vehicle powertrain applications," in *2016 IEEE Energy Conversion Congress and Exposition (ECCE)*, 18-22 Sept. 2016 2016, pp. 1-7.

[49] H. Cha, C. Rogers, X. Lu, and F. Z. Peng, "Design of high efficient and high density integrated magnetics for interleaved DC-DC boost converter for series hybrid electric bus," in *2009 IEEE Vehicle Power and Propulsion Conference*, 7-10 Sept. 2009 2009, pp. 1428-1433.

[50] B. C. Barry, J. G. Hayes, and M. S. Ryłko, "CCM and DCM Operation of the Interleaved Two-Phase Boost Converter With Discrete and Coupled Inductors," *IEEE Transactions on Power Electronics,* vol. 30, no. 12, pp. 6551-6567, 2015.

[51] S. Haghbin, S. Lundmark, M. Alakula, and O. Carlson, "Grid-Connected Integrated Battery Chargers in Vehicle Applications: Review and New Solution," *IEEE Transactions on Industrial Electronics,* vol. 60, no. 2, pp. 459-473, 2013.

[52] G. J. Su and L. X. Tang, "An Integrated Onboard Charger and Accessory Power Converter for Traction Drive Systems with a Boost Converter," *2016 Ieee Energy Conversion Congress and Exposition (Ecce),* 2016.

[53] T. A. Burress, "EVALUATION OF THE 2007 TOYOTA CAMRY HYBRID SYNERGY DRIVE SYSTEM," 2008. [Online]. Available: https://www.osti.gov/servlets/purl/928684

[54] K. Raggl, T. Nussbaumer, G. Doerig, J. Biela, and J. W. Kolar, "Comprehensive Design and Optimization of a High-Power-Density Single-Phase Boost PFC," *IEEE Transactions on Industrial Electronics,* vol. 56, no. 7, pp. 2574-2587, 2009.

[55] M. R. Ahmed, G. Calderon-Lopez, F. Bryan, R. Todd, and A. J. Forsyth, "Soft-switching SiC interleaved boost converter," in *2015 IEEE Applied Power Electronics Conference and Exposition (APEC)*, 15-19 March 2015 2015, pp. 941-947.

[56] A. Merkert, J. Müller, and A. Mertens, "Component design and implementation of a 60 kW full SiC traction inverter with boost converter," in *2016 IEEE Energy Conversion Congress and Exposition (ECCE)*, 18-22 Sept. 2016 2016, pp. 1-8.

[57] O. Hegazy, J. V. Mierlo, and P. Lataire, "Analysis, control and comparison of DC/DC boost converter topologies for fuel cell hybrid electric vehicle applications," in *Proceedings of the 2011 14th European Conference on Power Electronics and Applications*, 30 Aug.-1 Sept. 2011 2011, pp. 1-10.

[58] K. J. Hartnett, M. S. Rylko, J. G. Hayes, and M. G. Egan, "A comparison of classical two phase (2L) and transformer — Coupled (XL) interleaved boost converters for fuel cell applications," in *2010 Twenty-Fifth Annual IEEE Applied Power Electronics Conference and Exposition (APEC)*, 21-25 Feb. 2010 2010, pp. 787-793.

[59] M. R. Ahmed, R. Todd, and A. J. Forsyth, "Soft-switching operation of the dual-interleaved boost converter over all duty ratios," *IET Power Electronics,* vol. 10, no. 11, pp. 1250-1258, 2017.

[60] G. Calderon-Lopez and A. J. Forsyth, "High-Power Dual-Interleaved ZVS Boost Converter with Interphase Transformer for Electric Vehicles," in *2009 Twenty-Fourth Annual IEEE Applied Power Electronics Conference and Exposition*, 15-19 Feb. 2009 2009, pp. 1078-1083.

[61] M. Hirakawa *et al.*, "High power DC/DC converter using extreme close-coupled inductors aimed for electric vehicles," in *The 2010 International Power Electronics Conference - ECCE ASIA -*, 21-24 June 2010 2010, pp. 2941-2948.

[62] K. J. Hartnett, J. G. Hayes, M. G. Egan, and M. S. Rylko, "CCTT-Core Split-Winding Integrated Magnetic for High-Power DC–DC Converters," *IEEE Transactions on Power Electronics,* vol. 28, no. 11, pp. 4970-4984, 2013.

[63] M. Hirakawa, M. Nagano, Y. Watanabe, K. Andoh, S. Nakatomi, and S. Hashino, "High power density DC/DC converter using the close-coupled inductors," in *2009 IEEE Energy Conversion Congress and Exposition*, 20-24 Sept. 2009 2009, pp. 1760-1767.

[64] K. J. Hartnett, J. G. Hayes, M. G. Egan, and M. S. Rylko, "Comparison of CCTT split-winding and EE integrated magnetics for high-power dc-dc converters," in *2011 IEEE Vehicle Power and Propulsion Conference*, 6-9 Sept. 2011 2011, pp. 1-6.

[65] K. J. Hartnett, J. G. Hayes, M. S. Rylko, B. J. Barry, and J. W. Masłoń, "Comparison of 8-kW CCTT IM and Discrete Inductor Interleaved Boost Converter for Renewable Energy Applications," *IEEE Transactions on Industry Applications,* vol. 51, no. 3, pp. 2455-2469, 2015.

[66] H. Chen, K. Sabi, H. Kim, T. Harada, R. Erickson, and D. Maksimovic, "A 98.7% Efficient Composite Converter Architecture With Application-Tailored Efficiency Characteristic," *IEEE Transactions on Power Electronics,* vol. 31, no. 1, pp. 101-110, 2016.

[67] H. Kim *et al.*, "SiC-MOSFET composite boost converter with 22 kW/L power density for electric vehicle application," in *2017 IEEE Applied Power Electronics Conference and Exposition (APEC)*, 26-30 March 2017 2017, pp. 134-141.

[68] "Onboard Charger." https://www.tesla.com/support/home-charging-installation/onboard-charger.

[69] M. C. Kisacikoglu, B. Ozpineci, and L. M. Tolbert, "Effects of V2G reactive power compensation on the component selection in an EV or PHEV bidirectional charger," in *2010 IEEE Energy Conversion Congress and Exposition*, 12-16 Sept. 2010 2010, pp. 870-876.

[70] A. N. Brooks, "Vehicle-to-Grid Demonstration Project:Grid Regulation Ancillary Servicewith a Battery Electric Vehicle," 2002. [Online]. Available: http://www1.udel.edu/V2G/docs/V2G-Demo-Brooks-02-R5.pdf

[71] Y. Kim and J. Lee, "Full-Bridge+SRT Hybrid DC/DC Converter for a 6.6-kW EV On-Board Charger," *IEEE Transactions on Vehicular Technology,* vol. 65, no. 6, pp. 4419-4428, 2016.

[72] B. Lee, J. Kim, S. Kim, and J. Lee, "A PWM SRT DC/DC Converter for 6.6-kW EV Onboard Charger," *IEEE Transactions on Industrial Electronics,* vol. 63, no. 2, pp. 894-902, 2016.

[73] D. Gautam, F. Musavi, M. Edington, W. Eberle, and W. G. Dunford, "An automotive on-board 3.3 kW battery charger for PHEV application," in *2011 IEEE Vehicle Power and Propulsion Conference*, 6-9 Sept. 2011 2011, pp. 1-6.

[74] B. Gu, J. Lai, N. Kees, and C. Zheng, "Hybrid-Switching Full-Bridge DC–DC Converter With Minimal Voltage Stress of Bridge Rectifier, Reduced Circulating Losses, and Filter Requirement for Electric Vehicle Battery Chargers," *IEEE Transactions on Power Electronics,* vol. 28, no. 3, pp. 1132-1144, 2013.

[75] R. W. A. A. D. Doncker, D. M. Divan, and M. H. Kheraluwala, "A three-phase soft-switched high-power-density DC/DC converter for high-power applications," *IEEE Transactions on Industry Applications,* vol. 27, no. 1, pp. 63-73, 1991.

[76] M. Mingkai, X. Lingxiao, D. Boroyevich, B. Hughes, and P. Mattavelli, "Design of integrated transformer and inductor for high frequency dual active bridge GaN Charger for PHEV," in *IEEE Applied Power Electronics Conference and Exposition*, 15-19 March 2015 2015, pp. 579-585.

[77] X. Lingxiao, M. Mingkai, D. Boroyevich, and P. Mattavelli, "The optimal design of GaN-based Dual Active Bridge for bi-directional Plug-IN Hybrid Electric Vehicle (PHEV) charger," in *IEEE Applied Power Electronics Conference and Exposition*, 15-19 March 2015 2015, pp. 602-608.

[78] M. N. Kheraluwala, R. W. Gascoigne, D. M. Divan, and E. D. Baumann, "Performance characterization of a high-power dual active bridge DC-to-DC converter," *IEEE Transactions on Industry Applications,* vol. 28, no. 6, pp. 1294-1301, 1992.

[79] G. Guidi, M. Pavlovsky, A. Kawamura, T. Imakubo, and Y. Sasaki, "Improvement of light load efficiency of Dual Active Bridge DC-DC converter by using dual leakage transformer and variable frequency," in *2010 IEEE Energy Conversion Congress and Exposition*, 12-16 Sept. 2010 2010, pp. 830-837.

[80] B. Li, F. C. Lee, Q. Li, and Z. Liu, "Bi-directional on-board charger architecture and control for achieving ultra-high efficiency with wide battery voltage range," in *2017 IEEE Applied Power Electronics Conference and Exposition (APEC)*, 26-30 March 2017 2017, pp. 3688-3694.

[81] P. He and A. Khaligh, "Comprehensive Analyses and Comparison of 1 kW Isolated DC–DC Converters for Bidirectional EV Charging Systems," *IEEE Transactions on Transportation Electrification,* vol. 3, no. 1, pp. 147-156, 2017.

[82] H. Wang, S. Dusmez, and A. Khaligh, "Maximum Efficiency Point Tracking Technique for LLC-Based PEV Chargers Through Variable DC Link Control," *IEEE Transactions on Industrial Electronics,* vol. 61, no. 11, pp. 6041-6049, 2014.

[83] H. Li, Z. Zhang, S. Wang, J. Tang, X. Ren, and Q. Chen, "A 300-kHz 6.6-kW SiC Bidirectional LLC Onboard Charger," *IEEE Transactions on Industrial Electronics,* vol. 67, no. 2, pp. 1435-1445, 2020.

[84] W. Yu, J. Lai, W. Lai, and H. Wan, "Hybrid Resonant and PWM Converter With High Efficiency and Full Soft-Switching Range," *IEEE Transactions on Power Electronics,* vol. 27, no. 12, pp. 4925-4933, 2012.

[85] J. Lee and H. Chae, "6.6-kW Onboard Charger Design Using DCM PFC Converter With Harmonic Modulation Technique and Two-Stage DC/DC Converter," *IEEE Transactions on Industrial Electronics,* vol. 61, no. 3, pp. 1243-1252, 2014.

[86] T. Lixin and S. Gui-Jia, "A low-cost, digitally-controlled charger for plug-in hybrid electric vehicles," in *IEEE Energy Conversion Congress and Exposition*, 20-24 Sept. 2009 2009, pp. 3923-3929.

[87] L. Jianing, X. Guoqing, W. Bangming, B. Junfang, and W. Huijun, "A novel integrated switched reluctance motor drive with bi-directional inverter," in *IEEE International Conference on Industrial Technology*, Feb. 26 2014-March 1 2014 2014, pp. 885-889.

[88] L. Tian-Hua, Y. Pei-Heng, and C. Jui-Ling, "Implementation of an integrated battery-charger for an electric-propulsion system," in *IEEE Industrial Electronics Society*, Oct. 29 2014-Nov. 1 2014 2014, pp. 1526-1531.

[89] L. Young-Joo, A. Khaligh, and A. Emadi, "Advanced Integrated Bidirectional AC/DC and DC/DC Converter for Plug-In Hybrid Electric Vehicles," *Vehicular Technology, IEEE Transactions on,* vol. 58, no. 8, pp. 3970-3980, 2009.

[90] S. Ishigaki and A. Khaligh, "A Compact and Integrated Multifunctional Power Electronic Interface for Plug-in Electric Vehicles," *Power Electronics, IEEE Transactions on,* vol. 28, no. 12, pp. 5690-5701, 2013.

[91] M. Chinthavali, O. C. Onar, S. L. Campbell, and L. M. Tolbert, "All-SiC inductively coupled charger with integrated plug-in and boost functionalities for PEV applications," in *2016 IEEE Applied Power Electronics Conference and Exposition (APEC)*, 20-24 March 2016 2016, pp. 1307-1314.

[92] K. Itoh, M. Ishigaki, N. Yanagizawa, S. Tomura, and T. Umeno, "Analysis and Design of a Multiport Converter Using a Magnetic Coupling Inductor Technique," *IEEE Transactions on Industry Applications,* vol. 51, no. 2, pp. 1713-1721, 2015.

[93] M. Ishigaki, K. Ito, S. Tomura, and T. Umeno, "A new isolated multi-port converter using interleaving and magnetic coupling inductor technologies," in *2013 Applied Power Electronics Conference and Exposition (APEC)*, 17-21 March 2013 2013, pp. 1068-1074.

[94] B. You, J. Kim, B. Lee, G. Choi, and D. Yoo, "Optimization of powder core inductors of buck-boost converters for Hybrid Electric Vehicles," in *2009 IEEE Vehicle Power and Propulsion Conference*, 7-10 Sept. 2009 2009, pp. 730-735.

[95] M. S. Rylko, J. G. Hayes, and M. G. Egan, "Experimental investigation of high-flux density magnetic materials for high-current inductors in hybrid-electric vehicle DC-DC converters," in *2010 IEEE Vehicle Power and Propulsion Conference*, 1-3 Sept. 2010 2010, pp. 1-7.

[96] M. S. Rylko, K. J. Hartnett, J. G. Hayes, and M. G. Egan, "Magnetic Material Selection for High Power High Frequency Inductors in DC-DC Converters," in *2009 Twenty-Fourth Annual IEEE Applied Power Electronics Conference and Exposition*, 15-19 Feb. 2009 2009, pp. 2043-2049.

[97] W. Zhang, S. Anwar, D. Costinett, and F. Wang, "Investigation of Cost-effective SiC Based Hybrid Switch and Improved Inductor Design Procedure for Boost Converter in Electrical Vehicles Application," in *SAE Technical Paper*, 2015.

[98] M. S. Rylko, B. J. Lyons, J. G. Hayes, and M. G. Egan, "Revised Magnetics Performance Factors and Experimental Comparison of High-Flux Materials for High-Current DC–DC Inductors," *IEEE Transactions on Power Electronics,* vol. 26, no. 8, pp. 2112-2126, 2011.

[99] Y. Wang, G. Calderon-Lopez, and A. J. Forsyth, "High-Frequency Gap Losses in Nanocrystalline Cores," *IEEE Transactions on Power Electronics,* vol. 32, no. 6, pp. 4683-4690, 2017.

[100] R. Lee, *Electronic Transformers & Circuits*, 2 ed. New York, NY, USA: Wiley, 1955.

[101] T. Tera, H. Taki, and T. Shimizu, "Loss Reduction of Laminated Core Inductor used in On-board Charger for EVs," in *2014 International Power Electronics Conference*, 2014, pp. 876-882.

[102] W. Shen, F. Wang, D. Boroyevich, and C. W. Tipton, "Loss Characterization and Calculation of Nanocrystalline Cores for High-Frequency Magnetics Applications," *IEEE Transactions on Power Electronics,* vol. 23, no. 1, pp. 475-484, 2008.

[103] B. Cougo and J. W. Kolar, "Integration of Leakage Inductance in Tape Wound Core Transformers for Dual Active Bridge Converters," in *2012 7th International Conference on Integrated Power Electronics Systems (CIPS)*, 6-8 March 2012 2012, pp. 1-6.

[104] K. Izui, T. Yamada, S. Nishiwaki, and K. Tanaka, "Multiobjective optimization using an aggregative gradient-based method," *Structural and Multidisciplinary Optimization,* vol. 51, no. 1, pp. 173-182, 2015.

[105] J. Behnamian, S. M. T. Fatemi Ghomi, and M. Zandieh, "A multi-phase covering Pareto-optimal front method to multi-objective scheduling in a realistic hybrid flowshop using a hybrid metaheuristic," *Expert Systems with Applications,* vol. 36, no. 8, pp. 11057-11069, 2009.

[106] T. Wu, B. Ozpineci, and C. Ayers, "Genetic algorithm design of a 3D printed heat sink," in *2016 IEEE Applied Power Electronics Conference and Exposition (APEC)*, 20-24 March 2016 2016, pp. 3529-3536.

[107] M. J. Mauger, P. Kandula, and D. Divan, "Optimal Design of the Resonant Tank of the Soft-Switching Solid-State Transformer," in *2019 IEEE Energy Conversion Congress and Exposition (ECCE)*, 29 Sept.-3 Oct. 2019 2019, pp. 6965-6972.

[108] M. Hirakawa *et al.*, "High power density interleaved DC/DC converter using a 3-phase integrated close-coupled inductor set aimed for electric vehicles," in *2010 IEEE Energy Conversion Congress and Exposition*, 12-16 Sept. 2010 2010, pp. 2451-2457.

[109] P. Deck and C. P. Dick, "High power density DC/DC-converter using coupled inductors," in *2017 19th European Conference on Power Electronics and Applications (EPE'17 ECCE Europe)*, 11-14 Sept. 2017 2017, pp. P.1-P.10.

[110] L. Chen, J. Wang, P. Lazari, and C. Xiao, "Optimizations of a permanent magnet machine targeting different driving cycles for electric vehicles," in *2013 International Electric Machines & Drives Conference*, 12-15 May 2013 2013, pp. 855-862.

[111] T. Schoenen, M. S. Kunter, M. D. Hennen, and R. W. De Doncker, "Advantages of a variable DC-link voltage by using a DC-DC converter in hybrid-electric vehicles," in *IEEE Vehicle Power and Propulsion Conference (VPPC)* 1-3 Sept. 2010 2010, pp. 1-5.

[112] R. Karimi, T. Koeneke, D. Kaczorowski, T. Werner, and A. Mertens, "Low voltage and high power DC-AC inverter topologies for electric vehicles," in *Energy Conversion Congress and Exposition (ECCE), 2013 IEEE*, 15-19 Sept. 2013 2013, pp. 2805-2812.

[113] S. Tenner, S. Gunther, and W. Hofmann, "Loss minimization of electric drive systems using a DC/DC converter and an optimized battery voltage in automotive applications," in *Vehicle Power and Propulsion Conference (VPPC), 2011 IEEE*, 6-9 Sept. 2011 2011, pp. 1-7.

[114] J. Lu, Q. Tian, K. Bai, A. Brown, and M. McAmmond, "An indirect matrix converter based 97%-efficiency on-board level 2 battery charger using E-mode GaN HEMTs," in *2015 IEEE 3rd Workshop on Wide Bandgap Power Devices and Applications (WiPDA)*, 2-4 Nov. 2015 2015, pp. 351-358.

[115] C. W. T. McLyman, *Transformer and inductor design handbook*, 4th Edition ed. 2011.

[116] K. Venkatachalam, C. R. Sullivan, T. Abdallah, and H. Tacca, "Accurate prediction of ferrite core loss with nonsinusoidal waveforms using only Steinmetz parameters," in *2002 IEEE Workshop on Computers in Power Electronics, 2002. Proceedings.*, 3-4 June 2002 2002, pp. 36-41.

[117] R. P. Wojda and M. K. Kazimierczuk, "Winding resistance of litz-wire and multi-strand inductors," *IET Power Electronics*, vol. 5, no. 2, pp. 257-268.

[118] R. P. Wojda and M. K. Kazimierczuk, "Analytical optimization of litz-wire windings independent of porosity factor," *COMPEL - The international journal for computation and mathematics in electrical and electronic engineering,* vol. 34, no. 3, pp. 920-940, 2015.

[119] P. A. M. Bezerra, F. Krismer, R. M. Burkart, and J. W. Kolar, "Bidirectional isolated non-resonant DAB DC-DC converter for ultra-wide input voltage range applications," in *2014 International Power Electronics and Application Conference and Exposition*, 5-8 Nov. 2014 2014, pp. 1038-1044.

[120] G. G. Oggier and M. Ordonez, "High-Efficiency DAB Converter Using Switching Sequences and Burst Mode," *IEEE Transactions on Power Electronics,* vol. 31, no. 3, pp. 2069-2082, 2016.

[121] D. Costinett, H. Nguyen, R. Zane, and D. Maksimovic, "GaN-FET based dual active bridge DC-DC converter," in *2011 Twenty-Sixth Annual IEEE Applied Power Electronics Conference and Exposition (APEC)*, 6-11 March 2011 2011, pp. 1425-1432.

[122] "TE CONNECTIVITY EV200AAANA RELAY." http://www.te.com/usa-en/product-1618002-7.html.

[123] G. J. Su and L. X. Tang, "A Segmented Traction Drive System with a Small dc Bus Capacitor," *2012 Ieee Energy Conversion Congress and Exposition (Ecce),* pp. 2873-2879, 2012.

[124] J. W. Kolar and S. D. Round, "Analytical calculation of the RMS current stress on the DC-link capacitor of voltage-PWM converter systems," *Iee Proceedings-Electric Power Applications,* vol. 153, no. 4, pp. 535-543, 2006.

[125] X. D. Li and Y. F. Li, "An Optimized Phase-Shift Modulation For Fast Transient Response in a Dual-Active-Bridge Converter," *Ieee Transactions on Power Electronics,* vol. 29, no. 6, pp. 2661-2665, 2014.

[126] H. H. Zhou and A. M. Khambadkone, "Hybrid Modulation for Dual-Active-Bridge Bidirectional Converter With Extended Power Range for Ultracapacitor Application," *Ieee Transactions on Industry Applications,* vol. 45, no. 4, pp. 1434-1442, 2009.

[127] F. Krismer, S. Round, and J. W. Kolar, "Performance optimization of a high current dual active bridge with a wide operating voltage range," *2006 Ieee Power Electronics Specialists Conference, Vols 1-7,* pp. 935-941, 2006.

[128] O. Kumar, P. S. Shenoy, P. T. Krein, and S. Kapat, "Augmented boost converter for near null-load transient response," in *2011 IEEE Power and Energy Conference at Illinois*, 25-26 Feb. 2011 2011, pp. 1-6.

[129] T. Geyer, G. Papafotiou, R. Frasca, and M. Morari, "Constrained Optimal Control of the Step-Down DC–DC Converter," *IEEE Transactions on Power Electronics,* vol. 23, no. 5, pp. 2454-2464, 2008.

[130] "Dynamometer Drive Schedules " https://www.epa.gov/vehicle-and-fuel-emissions-testing/dynamometer-drive-schedules.

[131] K. Uddin, A. D. Moore, A. Barai, and J. Marco, "The effects of high frequency current ripple on electric vehicle battery performance," *Applied Energy,* vol. 178, pp. 142-154, 2016.

[132] P. Ngatchou, A. Zarei, and A. El-Sharkawi, "Pareto Multi Objective Optimization," in *Proceedings of the 13th International Conference on, Intelligent Systems Application to Power Systems*, 6-10 Nov. 2005 2005, pp. 84-91.

[133] Z. Wang, F. Yang, S. L. Campbell, and M. Chinthavali, "Characterization of SiC Trench MOSFETs in a Low-Inductance Power Module Package," *IEEE Transactions on Industry Applications,* vol. 55, no. 4, pp. 4157-4166, 2019.

[134] Z. J. Wang, F. Yang, S. Campbell, and M. Chinthavali, "Development of a low-inductance SiC trench MOSFET power module for high-frequency application," in *2018 IEEE Applied Power Electronics Conference and Exposition (APEC)*, 4-8 March 2018 2018, pp. 2834-2841.

[135] S. Chattopadhyay and S. Das, "A Digital Current-Mode Control Technique for DC–DC Converters," *IEEE Transactions on Power Electronics,* vol. 21, no. 6, pp. 1718-1726, 2006.

[136] C. Jingquan, A. Prodic, R. W. Erickson, and D. Maksimovic, "Predictive digital current programmed control," *IEEE Transactions on Power Electronics,* vol. 18, no. 1, pp. 411-419, 2003.

Vita

Saeed Anwar received his BS in Electrical and Electronic Engineering from Bangladesh University of Engineering and Technology at Dhaka, Bangladesh in 2011. He received his MS in Electrical Engineering from the University of Akron at Ohio, USA in 2014. He started his Ph.D. in 2014 at the Center for Ultra-wide-area Resilient Electric Energy Transmission Networks (CURENT) at the University of Tennessee, Knoxville. As a graduate research assistant at CURENT, his research focus was integrated power converter development for EVs, magnetics design, optimization, and control. He worked as Innovation Team Lead in the EcoCAR 3 competition from 2015 to 2018. He has received the NSF innovation award for his contribution to the EcoCAR 3 competition. He also worked at Power Electronics and Electronic Machinery (PEEM) Group at Oak Ridge National Laboratory (ORNL) from 2016 to 2020 as student intern. At ORNL, he supported the high-power high-frequency inverter development and testing for wireless power transfer (WPT) projects for EVs. His research work is highlighted at ORNL for a 120 kW WPT system demonstration to the US Department of Energy (DOE). He will join General Electric (GE) Aviation as the Power Electronic Lead Engineer after graduation.